University of Innsbruck
Faculty of Mathematics, Computer Science and
Physics

Institute for Experimental Physics

MASTER THESIS

Thesis submitted in fulfilment of the requirements for the degree of

Master of Science in Physics

Characterisation of an Erbium Atomic Beam for Rydberg Experiments with Optical Tweezers

Amal El Arrach, BSc

supervised by:
Dr. Manfred Mark
Prof. Dr. Francesca Ferlaino

Für meine Familie und meinen Freund.

Abstract

This master's thesis describes my work on the characterisation and optimisation of the experimentally required tools of a new experiment, the so-called TREQS experiment. The primary objective of the TREQS experiment is to simulate quantum systems by utilising neutral erbium atoms confined within reconfigurable optical tweezer arrays and excited to Rydberg states.

To comprehend the prerequisites for successfully generating and trapping erbium atoms, the first part of the thesis offers a comprehensive overview of the pertinent properties of erbium atoms, including their electron configuration, magnetic properties and transitions within the atomic energy spectrum relevant to this research project. Furthermore, the velocity distribution of a thermal gas of erbium atoms with extension to an atomic beam is presented. The second part gives an introduction to light-matter interaction focussing on laser cooling and deceleration of erbium atoms, which is fundamental for the understanding of this thesis. Building upon this foundation, the third part delves into the experimental setup of the TREQS experiment, detailing the apparatus and techniques employed. In particular, it covers the configuration and operation of the atomic cooling and deceleration sections, which play a crucial role in achieving the desired conditions for trapping single erbium atoms. The main body of this thesis (chapters 5-7) encompasses a meticulous characterisation of the laser cooling and slowing of the erbium atomic beam. I present a detailed analysis and optimisation of the transverse cooling setup, aiming to achieve an efficient collimation of the atomic beam in transversal direction. Furthermore, I measure and characterise the deceleration of the atomic beam in dependence of the magnetic fields and the light used in the Zeeman slower, the essential component for reducing the longitudinal velocity of the atomic beam. Finally, I give a theoretical introduction to Rydberg atoms in chapter eight, elucidating their unique characteristics and interactions. This chapter provides also a summary of the first research paper published within the timeframe of this thesis, where we used electromagnetically-induced transparency to perform a first spectroscopy of Rydberg states in erbium atoms on an atomic beam. In the last part of this thesis, I draw a conclusion and outlook on the next steps planned for this experimental setup. The systematic exploration, optimisation procedures, and characterisation of the key components of the experimental setup presented in this thesis contributes to advancing the understanding and the practical implementation of the TREQS experiment, opening new avenues for exploring quantum simulation with erbium atoms.

Zusammenfassung

Diese Masterarbeit beschreibt meine Arbeit zur Charakterisierung und Optimierung der experimentell erforderlichen Werkzeuge eines neuen Experiments, des sogenannten TREQS-Experiments. Das Hauptziel des TREQS-Experiments besteht darin, Quantensysteme zu simulieren, indem neutrale Erbiumatome verwendet werden, die in rekonfigurierbaren optischen Pinzettenarrays eingeschlossen und in Rydberg-Zustände angeregt werden.

Um die Voraussetzungen für eine erfolgreiche Erzeugung und Einfangung von Erbiumatomen zu verstehen, bietet der erste Teil der Arbeit einen umfassenden Überblick über die relevanten Eigenschaften von Erbiumatomen, einschließlich ihrer Elektronenkonfiguration, magnetischen Eigenschaften und Übergänge innerhalb des für dieses Forschungsprojekt relevanten Atomenergiespektrums. Zusätzlich wird die Geschwindigkeitsverteilung eines thermischen Gases aus Erbiumatomen mit Erweiterung auf einen Atomstrahl eingeführt. Der zweite Teil gibt eine Einführung in die Licht-Materie-Wechselwirkung mit Schwerpunkt in Laserkühlung und Abbremsung von Erbiumatomen, die für das Verständnis dieser Arbeit von grundlegender Bedeutung sind. Aufbauend auf dieser Grundlage befasst sich der dritte Teil mit dem Versuchsaufbau des TREQS-Experiments und beschreibt detailliert die verwendeten Geräte und Techniken. Es behandelt insbesondere die Konfiguration und den Betrieb der atomaren Kühl- und Abbremsabschnitte, die eine entscheidende Rolle beim Erreichen der gewünschten Bedingungen zum Einfangen einzelner Erbiumatome spielen. Der Hauptteil dieser Arbeit (Kapitel 5-7) umfasst eine sorgfältige Charakterisierung der Laserkühlung und Verlangsamung des Erbium-Atomstrahls. Ich präsentiere eine detaillierte Analyse und Optimierung des transversalen Kühlaufbaus mit dem Ziel, eine effiziente Kollimation des Atomstrahls in transversaler Richtung zu erreichen. Darüber hinaus messe und charakterisiere ich die Abbremsung des Atomstrahls in Abhängigkeit der Magnetfelder und des Lichts des Zeeman Slowers, der wesentlichen Komponente zur Reduzierung der Längsgeschwindigkeit des Atomstrahls. Abschließend gebe ich im achten Kapitel eine theoretische Einführung in Rydberg-Atome und erläutere ihre einzigartigen Eigenschaften und Wechselwirkungen. Dieses Kapitel bietet auch eine Zusammenfassung der ersten Forschungsarbeit, die im Zeitraum dieser Arbeit veröffentlicht wurde und in der wir elektromagnetisch induzierte Transparenz nutzten, um eine erste Spektroskopie von Rydberg-Zuständen in Erbiumatomen an einem Atomstrahl durchzuführen. Im letzten Teil dieser Arbeit ziehe ich ein Fazit und gebe einen Ausblick auf die nächsten geplanten Schritte für diesen Versuchsaufbau. Die in

dieser Arbeit vorgestellte systematische Erforschung, sowie die präsentierten Optimierungsverfahren und die Charakterisierung der Schlüsselkomponenten des Versuchsaufbaus trägt dazu bei, das Verständnis und die praktische Umsetzung des TREQS-Experiments voranzutreiben und neue Wege für die Erforschung der Quantensimulation mit Erbiumatomen zu eröffnen.

Acknowledgements

Contents

Contents

Eidesstattliche Erklärung

Ich erkläre hiermit an Eides statt durch meine eigenhändige Unterschrift, dass ich die vorliegende Arbeit selbständig verfasst und keine anderen als die angegebenen Quellen und Hilfsmittel verwendet habe. Alle Stellen, die wörtlich oder inhaltlich den angegebenen Quellen entnommen wurden, sind als solche kenntlich gemacht.

Die vorliegende Arbeit wurde bisher in gleicher oder ähnlicher Form noch nicht als Magister-/Master-/Diplomarbeit/Dissertation eingereicht.

Innsbruck, am 30.02.2024　　　　　　　　　　　　　　　Amal El Arrach, BSc

1. Introduction

The idea of building programmable quantum systems in the lab was first suggested by Richard Feynman [1]. According to him, synthetically built quantum systems that evolve under the desired Hamiltonian with tunable parameters would allow for estimating the many-body dynamics of systems, surpassing the simulation capacity of classical computers and even supercomputers within a reasonable timeframe. This challenge is rooted in the limitation of deriving macroscopic behavior from microscopic properties, particularly the interactions between particles, due to the exponential scaling of the Hilbert space size with the number of particles [2]. This approach, known as 'analog quantum simulation', has catalysed a rapidly growing research field over the past twenty years. However, the major hurdle has been the experimental realisation of well-controllable quantum many-body systems, equipped with tunable interactions and arbitrary state initialisation.

The TREQS experiment aims to simulate quantum systems by utilising neutral erbium atoms trapped in reconfigurable optical tweezer arrays. These atoms interact with each other by being excited into Rydberg states, characterised by special features such as extremely large electric dipole moments, resulting in strong interactions with external fields and electromagnetic fields from surrounding atoms. This interaction is notably long-range, surpassing typical interactions between atoms in lower energy states and extending to atoms separated by even micrometers [3]. Furthermore, this interaction is switchable, allowing atoms to be excited to Rydberg states in a time-controlled manner using laser pulses. Consequently, Rydberg atoms emerge as promising candidates for implementing highly controllable quantum many-body simulators [4].

The optical tweezers provide the ability to capture and hold the individual atoms and position them in arbitrary configurations, enabling controlled engineering of scalable many-body systems for quantum information processing, quantum simulations, and precision measurements [5]. These optical tweezers are tightly focussed laser beams exhibiting an optical force onto the atoms, providing a trap for sufficiently cold atoms at the waist of the laser beam. As demonstrated in [5] for ^{87}Rb atoms, it is possible to produce defect-free one-dimensional cold atom arrays as well as two-dimensional atomic arrays of the same atom species as shown in [6].

This thesis discusses the experimental realisation of a beam of cold erbium atoms that can be later trapped in a magneto-optical trap (MOT) and subsequently loaded

14

into optical tweezers and excited to Rydberg states. To gain a comprehensive understanding of the requirements for effectively generating and trapping the erbium atoms, Chapter 2 presents a thorough overview of the essential properties of erbium atoms. This part includes their electron configuration, magnetic properties, and transitions within the atomic energy spectrum that are relevant to this thesis. Furthermore, I discuss the theory behind the velocity distribution of a thermal gas of erbium atoms following the so-called Maxwell-Boltzmann statistics.

In contrast, Chapter 3 focusses on the fundamental concept of light-matter interaction, specifically emphasising laser cooling and laser deceleration of erbium atoms, which do both play a crucial role in the comprehension of this thesis. Here, I give a general introduction to the radiation pressure which is fundamental for laser cooling and the deceleration of atoms. In addition, I introduce the theory behind the optical molasses which provides collimation of the atomic beam, but is also one of the key elements of the magneto-optical trapping (MOT) mechanism needed for the experiment. Furthermore, in this part of the thesis I delve into one of the most popular techniques used for the deceleration of atoms in longitudinal direction, employing both, optical and magnetic fields, the so-called Zeeman slower (ZS). This system allows the deceleration of atoms over velocity ranges of several hundreds of m/s.

In Chapter 4 of this thesis I delve into the experimental setup of the TREQS experiment and provide detailed informations on the apparatus and techniques employed. In Chapter 5 I give an overview on the measurement procedures used for the experimental part of this thesis, including both, differential absorption spectroscopy, as well as fluorescence imaging. Furthermore, I give an introduction to expected lineshapes and broadening mechanisms.

In Chapter 6 I encompass a meticulous characterisation and optimisation of the transversal cooling setup, aiming to achieve efficient collimation of the erbium atomic beam in transversal direction. The first set of measurements taken after the transversal cooling section, utilising a technique called differential absorption spectroscopy, allows to estimate the action of the optical molasses onto the atomic beam and to determine the frequency leading to an efficient cooling and collimation performance. The same measurements have been taken at the MOT position utilising fluorescence imaging to further optimise the transversal cooling (TC) laser beams in frequency, as well as in alignment and polarisation. For completeness, also the power characteristics of the TC laser beams have been recorded.

Next, in Chapter 7 I delve into the optimisation of the light of the Zeeman slower in frequency, as well as polarisation and the power characteristics via fluorescence imaging. In addition, the impact of the settings of the magnetic field of the ZS are elaborated.

In the subsequent Chapter 8, I discuss the theoretical aspects of Rydberg atoms, focussing on their distinct characteristics and interactions. This part of the thesis also contains a summary of the first research paper published during the course of this thesis, highlighting the findings of the first spectroscopy on Rydberg states in erbium using electromagnetically-induced transparency of an atomic beam. Finally, in the last Chapter 9 of this thesis I present the conclusions and an outlook for future work on this topic.

2. Ultracold erbium atoms

The subsequent sections provide a comprehensive overview of the pertinent properties of erbium important for ultracold quantum gas experiments. Following a general introduction to erbium, this includes a detailed examination of its electron configuration, magnetic properties, and the specific transitions within its atomic energy spectrum that hold relevance for this thesis. Furthermore, the velocity distribution of a thermal gas of erbium atoms produced in a high temperature oven will be discussed.

2.1. History and basic properties of erbium

In 1842, the mineral godolinite was separated by Carl Gustaf Mosander into three distinct fractions, called yttria, erbia, and terbia [7]. Then, starting from 1860 the term "erbia" was reassigned to refer specifically to terbia and after 1877, the substance previously known as erbia was officially recognized as terbia. However, in this period erbia named a mixture consisting of five oxides, nowadays named erbium, scandium, holmium, thulium and ytterbium [8]. The successful production of pure erbium was achieved for the first time by Klemm and Bommer in 1943 by heating purified erbium chloride with potassium [8]. The first erbium Bose-Einstein condensate (BEC) has been realised 2012 in Innsbruck [9].

Erbium belongs to the lanthanide series of elements in the periodic table and is classified as a rare-earth element. Moreover, it is characterised by a proton number of $Z = 68$ and a mass of $m_{\mathrm{Er}} = 167.259(3)\,\mathrm{u}$, where $1\,\mathrm{u}$ is equivalent to $1.660\,540\,2 \times 10^{-27}\,\mathrm{kg}$ [10]. As other lanthanides, erbium has a high melting point of $1529\,°\mathrm{C}$ and a boiling point of $2900\,°\mathrm{C}$ [8]. It is a soft and malleable metal with a bright, silvery, metallic shine. At room temperature and under standard conditions of pressure erbium exists in the solid phase. Furthermore, erbium has a density of $\rho_{\mathrm{Er}} = 9.07\,\mathrm{gcm}^{-3}$ at a temperature of $25\,°\mathrm{C}$ [8]. The vapor pressure of erbium as a function of temperature T can according to [8] be described by

$$p_{\mathrm{vap}} = 10^{5.006+9.916-16642/T-1.2154\log_{10}T} \tag{2.1}$$

and is illustrated in Figure 2.1.
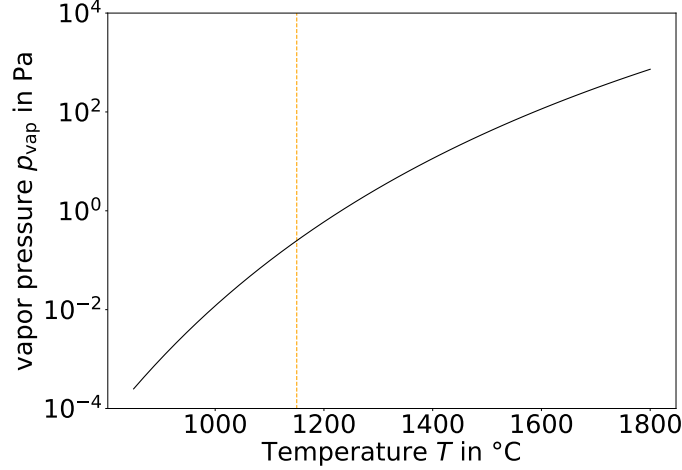
Figure 2.1.: The black solid line shows the vapour pressure curve of erbium p_{vap} as function of temperature T. The dashed orange line marks the temperature at which the erbium atomic oven of the TREQS experiment is operated.

Occurring naturally, erbium is a mixture of six stable isotopes where ^{162}Er, ^{164}Er, ^{166}Er, ^{168}Er, ^{170}Er are bosonic isotopes and ^{167}Er is a fermionic isotope. The bosonic isotopes have a nuclear spin I equal zero, the fermionic isotope has a nuclear spin of $I = 7/2$. For the fermionic isotope this results in a manifold of eight hyperfine levels in the electronic ground state [11]. The isotopes with the corresponding abundances are listed in Table 2.1. In this thesis we will focus on the most abundant isotope ^{166}Er.

Table 2.1.: Isotopes of erbium with corresponding abundance and type of quantum mechanical statistics. The values for the abundance are taken from [8].

Isotope	abundance in %	statistics
^{162}Er	0.139(5)	bosonic
^{164}Er	1.601(3)	bosonic
^{166}Er	33.503(36)	bosonic
^{167}Er	22.869(6)	fermionic
^{168}Er	26.978(18)	bosonic
^{170}Er	14.910(36)	bosonic

2.2. Electron configuration

The electron configuration of the ground state of erbium can according to the standard notation be written as

$$[\text{Xe}]4f^{12}6s^2.$$

Here [Xe] corresponds to the electron configuration of xenon. With the orbital momentum quantum number $L = 5$ and the spin quantum number $S = 1$ the angular momentum quantum number $J = L + S$ (in the standard LS coupling scheme) of the ground state results in $J = 6$. According to the notation $^{2S+1}L_J$ the ground state of erbium can then be written as $^3\text{H}_6$.

Neutral erbium has 68 electrons in total that fill the electronic orbitals according to the Madelung rule establishing the order in which the electrons fill the energy levels of an atom. The occupation of the electrons lead to a so-called submerged-shell structure, as the outer $6s$ orbital is filled before the inner $4f$ orbitals are [12]. There are seven available $4f$ orbitals that can take up to 14 electrons in total. The absence of the two electrons out of 14 possible ones, having an angular momentum projection number on the chosen quantisation axis of $m_l = +2$ and $m_l = +3$, in the $4f$ shells leads to a large orbital momentum. The spin projection quantum number of both electrons is $m_s = -1/2$. The $4f$ orbitals are highly anisotropic due to their large angular momentum quantum number of $l = 3$ leading to a strongly anisotropic van der Waals interaction potential. In contrast, the $6s$ orbital with angular momentum quantum number $l = 0$ is spherically symmetric [11]. The angular dependence of the $4f$ wavefunctions for different values of the magnetic quantum number m_l are shown in Figure 2.2.
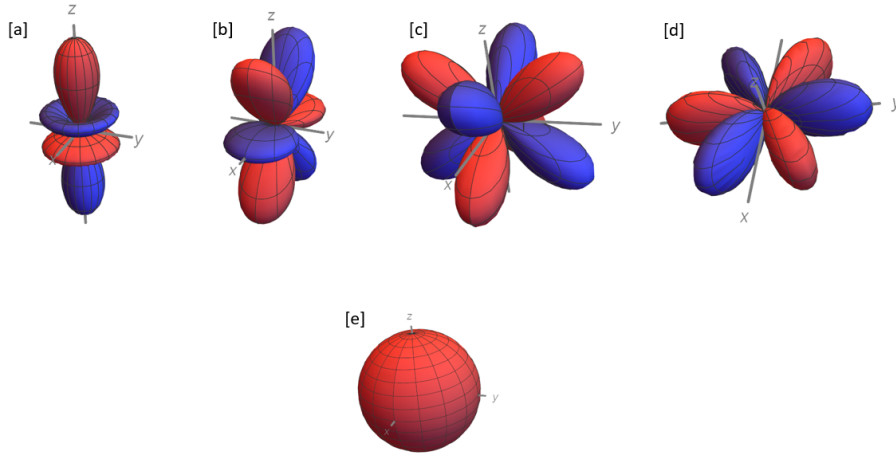
Figure 2.2.: Angular dependence of the $4f$ wavefunctions for different values of the magnetic quantum number m_l. For subfigure [a] $m_l = 0$, for [b] $|m_l| = 1$, for [c] $|m_l| = 2$ and for [d] $|m_l| = 3$. Subfigure [e] shows the symmetric $6s$ state. This graphic has been created using the code from [13].

Regarding the coupling of electrons in heavy elements as e.g. erbium, the spin-orbit coupling scheme of the electrons is replaced by the jj-coupling for excited

states. For most lanthanide elements, the special case of $J_1 J_2$ coupling becomes relevant, where the inner electrons of the [Xe] configuration couple independently as well as the electrons from the outer $6s$ shell. The relevant quantum numbers are the angular momentum quantum numbers of the two independent systems of coupled electrons with assigned angular momentum quantum numbers J_1 and J_2. The sum of this two independent quantum numbers $J_1 + J_2 = J$ gives the overall total angular momentum. Here the notation $(J_1, J_2)_J$ is introduced [12].

2.3. Atomic energy spectrum and the relevant laser cooling transitions

The rich electronic structure of erbium is caused by the submerged-shell structure already mentioned in the previous section. In a first view, this complexity seems to be disadvantageous for laser cooling and trapping because of unwanted decay channels and spurious excitation possibilities.

However, it has been shown that successful laser cooling of erbium atoms is possible, as there are suitable electric-dipole allowed transitions for this purpose, see [14]. In case of the TREQS experiment the erbium atoms are decelerated by using a so-called Zeeman slower, which will be introduced in Section 3.5. To operate the Zeeman slower efficiently, a transition with a broad linewidth is preferential to ensure many scattering events leading to a strong deceleration force. To be more precise, in the TREQS experiment, the strongest transition of erbium near 401 nm is used for the transversal cooling, as well as for the Zeeman slowing process. For this transition one of the $6s$ electrons gets excited into a $6p$ orbital and couples with the remaining $6s$ electron to a ${}^1\mathrm{P}_1$ singlet state. The remaining inner electrons couple via the well-known LS-coupling scheme to a ${}^3\mathrm{H}_6$ state. These two independently coupled systems $J_1 J_2$ couple to a $(J_1, J_2)_J$ state with electron configuration $[\mathrm{Xe}]4f^{12}({}^3\mathrm{H}_6)6s6p({}^1\mathrm{P}_1)(6,1)_7$.

In contrast, a narrow-line transition (near to 583 nm) is used for the magneto-optical trap as the small natural linewidth leads to a lower Doppler temperature and thus to better starting conditions for loading the tweezer traps in later steps of the experiment. For this transition, the excited $6p$ electron couples with the $6s$ electron to a ${}^3\mathrm{P}_1$ triplet state. This is a so-called recombination line as this electric dipole transition violates the spin-conserving selection rule. Analogously to the previously introduced notation, the electron configuration of the resulting state reads $[\mathrm{Xe}]4f^{12}({}^3\mathrm{H}_6)6s6p({}^3\mathrm{P}_1)(6,1)_7$ [12]. The relevant laser cooling parameters that characterise the used transitions can be found in Table 2.2. The atomic energy spectrum of erbium for energy values up to 25 000/cm is shown in Figure 2.3.
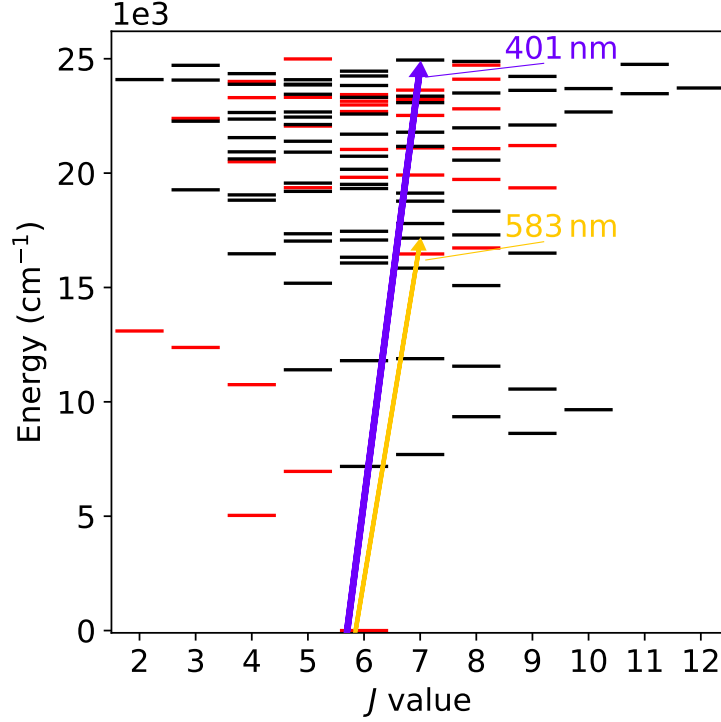
Figure 2.3.: Atomic level spectrum of erbium for energy values up to $25\,000/\text{cm}$ for different values of the total angular momentum quantum number J. Odd parity states are indicated as black lines, even parity states are indicated as red lines. The laser cooling transition for the Zeeman slower ($401\,\text{nm}$) is indicated as blue arrow, the laser cooling transition for the magneto-optical trap ($583\,\text{nm}$) is indicated as yellow arrow.

Table 2.2.: Values of the laser cooling parameters for the relevant electric dipole transitions used for the Zeeman slower ($401\,\text{nm}$) and for the magneto-optical tap ($583\,\text{nm}$). Data taken from [15].

laser cooling parameter	401 nm transition	583 nm transition
natural transition rate γ	$1.87 \times 10^8/\text{s}$	$1.17 \times 10^6/\text{s}$
lifetime τ	$5.35\,\text{ns}$	$875\,\text{ns}$
natural linewidth $\Delta\nu_{\text{nat}}$	$29.7\,\text{MHz}$	$0.19\,\text{MHz}$
saturation intensity I_{S}	$60.3\,\text{mW/cm}^2$	$0.13\,\text{mW/cm}^2$
Doppler temperature T_{D}	$714\,\mu\text{K}$	$4.6\,\mu\text{K}$
Doppler velocity v_{D}	$267\,\text{mm/s}$	$21\,\text{mm/s}$
recoil temperature T_{r}	$717\,\text{nK}$	$339\,\text{nK}$
recoil velocity v_{r}	$6\,\text{mm/s}$	$4.1\,\text{mm/s}$
precise wavelength λ	$400.796\,\text{nm}$	$582.681\,\text{nm}$

2.4. Magnetic properties of bosonic erbium

According to definition, the magnetic quantum numbers m_J are given by the projection of the total angular momentum quantum number J onto the chosen quantisation axis that is defined in relation to an external magnetic field. The quantised values of m_J range from $-J$ to J according to space quantisation demonstrated by Otto Stern and Walther Gerlach [16]. The magnetic moment of an atom is given by

$$\mu = m_J g_J \mu_{\mathrm{B}}. \tag{2.2}$$

Here μ_{B} denotes the Bohr magneton and g_J the Landé g-factor. Usually, under the assumption of pure spin-orbit coupling the Landé g-factor can be calculated as

$$g_J = 1 + (g_s - 1)\frac{J(J+1) - L(L+1) + S(S+1)}{2J(J+1)}, \tag{2.3}$$

with $g_s \approx 2.00232$ [11]. In the case of lanthanide erbium, several corrections need to be considered that lead to a reduction of the value. As explained in [17], one part of the correction accounts for the deviations from the spin-orbit coupling scheme. Furthermore, relativistic corrections as well as diamagnetic corrections need to be considered. Thus a experimentally determined value of $g_J = 1.163801(1)$ is used in the following calculations [18]. Atomic erbium exhibits an exceptional characteristic with its remarkably high magnetic moment. For the ground state ${}^3\mathrm{H}_6$ of bosonic erbium the magnetic moment μ corresponding to the energetically highest state with a magnetic quantum number $m_J = 6$ can be calculated with Equation (2.2) to $\mu = 6.982806(6)\mu_{\mathrm{B}}$. This places erbium among the elements possessing the largest magnetic moments in the periodic table. This remarkable characteristic gives rise to captivating dipolar effects that become observable in the ultracold regime. In contrast, alkali metals only possess a magnetic moment of $1\mu_{\mathrm{B}}$. Other elements such as terbium and dysprosium have even larger magnetic moments with $\mu = 9.94\mu_{\mathrm{B}}$ and $\mu = 9.93\mu_{\mathrm{B}}$, respectively [19].

For the excited states, under the assumption of jj-coupling, the gyromagnetic ratio g_J for a total electronic angular momentum quantum number J_1 and J_2 of the two coupled parts can be calculated as

$$\begin{aligned} g_J = g_{J_1} &\frac{J(J+1) + J_1(J_1+1) - J_2(J_2+1)}{2J(J+1)} \\ +g_{J_2} &\frac{J(J+1) + J_2(J_2+1) - J_1(J_1+1)}{2J(J+1)}. \end{aligned} \tag{2.4}$$

Here g_{J_1} and g_{J_2} denote the Landé g-factors of the two coupled parts that can be calculated according to Equation (2.3). Including the already mentioned correc-

tions for the Landé g-factors, the gyromagnetic ratios for the excited states of the two relevant transitions, the 401 nm transition and the 583 nm transition, can be calculated with Equation (2.4) to $g_J = 1.160$ and $g_J = 1.195$, respectively [11].

2.5. Velocity distribution of an erbium atomic beam

The atomic gas of erbium atoms needed for the experiment is produced in a high-temperature oven. Within this oven, the thermal cloud that is characterised by the temperature T is assumed to have a motional spread that can be well described by the Maxwell-Boltzmann velocity distribution. This velocity distribution can be defined individually for all axes representing the positional space. For a chosen axis, let us say along the $z-$axis, the Maxwell-Boltzmann velocity probability density of the one-component velocity can be written as

$$P_T(v_z)\mathrm{d}v_z = \sqrt{\frac{m}{2\pi k_\mathrm{B}T}} \exp\left(-\frac{mv_z^2}{2k_\mathrm{B}T}\right)\mathrm{d}v_z. \tag{2.5}$$

This function describes the probability to find an atom with mass m having a velocity v_z within the infinitesimal point unit $\mathrm{d}v_z$.

However, to define the probability of finding an atom with velocity $v = |\vec{v}|$ in the three dimensional velocity-space set by (v_x, v_y, v_z), it is common to write down the product of the one-dimensional velocity probability densities as

$$P_T(v_x)P_T(v_y)P_T(v_z)\mathrm{d}v_x\mathrm{d}v_y\mathrm{d}v_z = \left(\frac{m}{2\pi k_\mathrm{B}T}\right)^{\frac{3}{2}} \exp\left(-\frac{m(v_x^2 + v_y^2 + v_z^2)}{2k_\mathrm{B}T}\right)\mathrm{d}v_x\mathrm{d}v_y\mathrm{d}v_z.$$

This is valid under the assumption that all three probabilities are independent and characterised by the same temperature T. As a next step, transforming the infinitesimal cartesian volume unit $\mathrm{d}v_x\mathrm{d}v_y\mathrm{d}v_z$ to spherical polar coordinates as $\mathrm{d}v_x\mathrm{d}v_y\mathrm{d}v_z = \mathrm{d}v(v\mathrm{d}\theta)(v\sin\phi\mathrm{d}\phi)$, after integration over Θ and ϕ giving an additional factor of 4π, the normalised probability density can be written as

$$P_T(v)\mathrm{d}v = 4\pi \left(\frac{m}{2\pi k_\mathrm{B}T}\right)^{3/2} v^2 \exp\left(-\frac{mv^2}{2k_\mathrm{B}T}\right)\mathrm{d}v. \tag{2.6}$$

This velocity distribution is assumed to well describe the motional spread of the thermal atomic sample within the oven of the TREQS experiment and is shown as a function of velocity v for a sample of erbium atoms in Figure 2.4 for different temperatures. The most probable velocity within this distribution is given by $v_\mathrm{mp} = \sqrt{2k_\mathrm{B}T/m}$ and corresponds to the maximum position of the distribution.
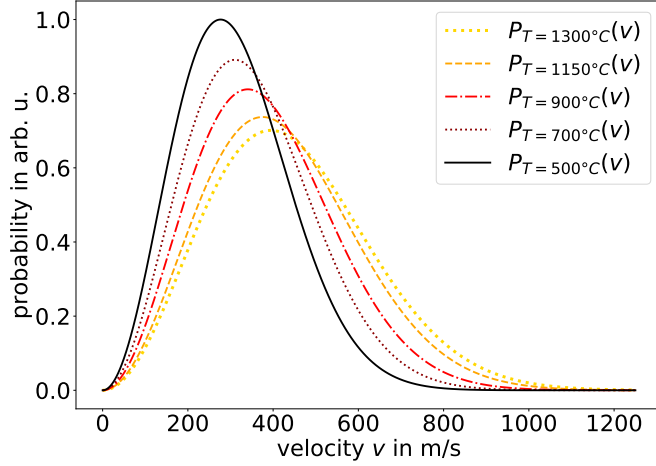
Figure 2.4.: Velocity distribution of a thermal gas of erbium atoms described by Equation (2.6). The velocity distribution $P_T(v)$ is shown for temperatures chosen as $T = 500\,°\mathrm{C}$ (black solid line), $T = 700\,°\mathrm{C}$ (dark red dotted line), $T = 900\,°\mathrm{C}$ (red dash-dotted line), $T = 1150\,°\mathrm{C}$ (orange dashed line) and $T = 1300\,°\mathrm{C}$ (yellow fat-dotted line). The velocity distribution $P_T(v)$ with $T = 1150\,°\mathrm{C}$ corresponds to the velocity distribution obtained in the TREQS experiment.

However, the motional spread of the atoms emerging from the oven through an aperture can no longer be described by Equation (2.6). As explained in [20], in the molecular effusion regime the number of particles $\mathrm{d}Q$ emerging per second from the aperture in solid angle $\mathrm{d}\omega$ at an angle Θ relative to the normal to the plane containing the aperture can be written as

$$\mathrm{d}Q = \frac{\mathrm{d}\omega}{4\pi} n\bar{v}\cos(\Theta)A, \tag{2.7}$$

where n is the number of particles per unit volume, $\bar{v}$ is the mean atom velocity and A is the aperture area, as indicated in Figure 2.5. Integrating $\mathrm{d}\omega$ as $2\pi\sin(\Theta)\mathrm{d}\Theta$ with Θ going from 0 to $\pi/2$ leads to

$$Q = \frac{1}{4}n\bar{v}A \propto \bar{v}. \tag{2.8}$$

This means the probability to emerge through the aperture is proportional to the atom velocity leading to a new velocity distribution given by

$$P_T'(v) = \left(\frac{m}{k_\mathrm{B}T}\right)^2 v^3 \exp\left(-\frac{mv^2}{2k_\mathrm{B}T}\right). \tag{2.9}$$

This function is assumed to well describe the motional spread of the atomic beam

emerging from the oven aperture with most probable velocity $v'_{\mathrm{mp}} = \sqrt{3k_{\mathrm{B}}T/m}$.

In general, the velocity distribution can be separated into a longitudinal and a transversal distribution, whereas the longitudinal distribution is mostly characterised by the source temperature and the transversal distribution by the geometry of the collimating apertures. The narrowed transversal velocity distribution can still be described by a symmetric Gaussian, but the width of the distribution is characterised by some reduced temperature T_{coll}. This temperature is determined by a strict limit on the sideways movement of atoms, ensuring they remain sufficiently low to pass through the aperture without straying too far from the center.
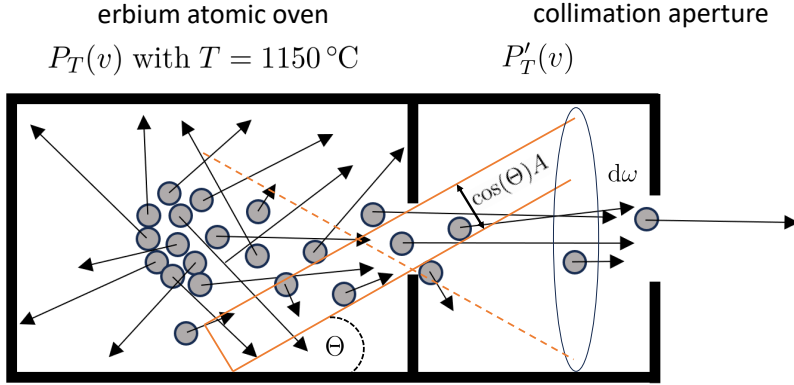
Figure 2.5.: Thermal gas with motional spread characterised by the oven temperature T leaving the oven though an aperture with area A under an angle Θ into a solid angle $\mathrm{d}\omega$. The atomic beam velocity distribution with additional v proportionality of the probability is further deformed by passing other collimating apertures. Figure inspired by [21].

A theoretical quantitative estimation of the velocity distribution of the atomic beam along the different sections of the vacuum apparatus used in the TREQS experiment is almost impossible, as there are many processes and parameters influencing the atomic motion and deforming the velocity distribution. As explained in [22], the velocity distribution of a collimated atomic beam is strongly depending on the geometry of the collimating aperture and the calculation of the collimated velocity distribution is only possible under certain assumptions of the geometry of the collimator. Furthermore, as explained in [20] and also further elaborated experimentally in [23], the dynamics of the atoms are also strongly dependent on the flow regime, that can be either of molecular or hydrodynamic nature. These regimes lead to different gas kinetics in dependence of the atomic density and the characteristics of the atom species. This means, the regime is not equal over the entire experiment as the atomic density is reduced continuously after passing each section of the experiment. Additionally, as explained in [23] and [21], the scattering behaviour of

the atoms with the surrounding walls is also influencing the atomic motion. Here it needs to be considered that the surface of the walls is rough on an atomic scale, but also, that the scattering process is depending on the temperature of the wall and of the collimating apertures (bright or dark wall). Because of this high complexity of the processes and the large number of parameters the deformation of the motional spread depends on, it is common to characterise the velocity distribution of the atomic beam experimentally. The experimental approach for the characterisation and the manipulation of the atomic motion of the TREQS experiment is discussed in the experimental part of this thesis.

3. Laser Cooling and Deceleration of Erbium Atoms

Already in 1917, in his paper on blackbody radiation [24], Einstein discussed the thermodynamics of absorption an re-emission cycles of radiation taking note of the momentum transfer in spontaneous emission. This is followed by studies of Frisch, observing the deflection of a sodium atomic beam by resonant light in 1933 [25]. However, at this time the mechanical effect of the light pressure acting on the atomic beam was considered insignificant, due to the low brightness of the available light sources. The invention of narrow linewidth tunable lasers in the 1970s led to a large progress in the field of laser cooling and trapping and has been substantial to initialise a long list of experiments developing the laser cooling and trapping techniques used nowadays in the laboratories [26]. In the field of quantum physics, the ability to cool and trap atoms by using laser light led to a platform for experiments on quantum technologies as for example quantum simulators and quantum information processing [27], quantum computing [28] or atomic clocks [29].

This chapter focusses on the radiation pressure which corresponds to the phase-shifted response of the atom's electric field dipole to the oscillating electric field, resulting in a dissipative force that can be used for laser cooling. In addition, an atom cooling technique based on radiation pressure, the so-called optical molasses, will be introduced. Furthermore, one of the most popular techniques used to decelerate atoms, the so-called Zeeman slower, will be explained, focussing on a Zeeman slower for bosonic erbium.

3.1. Radiative optical force

The general idea behind using an optical force to slow down moving atoms is the conservation of energy and momentum during absorption an re-emission cycles of radiation. The momentum transferred to the atom during the absorption of a photon coming from a laser beam is given by $\hbar\vec{k}$, with $\vec{k}$ denoting the wave vector of the incoming photon. A photon from a laser operating at a frequency ω_l is absorbed by the atom in case the laser is resonant to an atomic transition from the ground state to some excited state with energy difference $\Delta E = \hbar\omega_a$ that is characterised by the atomic resonance frequency ω_a leading to the condition $\omega_a - \omega_l = 0$. In case the atom is moving, the energy difference between the ground and the excited state

seems to be changed as the atom sees a shifted frequency of the laser. Thus the frequency of the laser needs to be changed by the so-called Doppler shift which is defined as $\omega_{\mathrm{D}} = -\vec{k}\vec{v}$ transforming the resonance condition to

$$\omega_{\mathrm{a}} - \omega_{\mathrm{l}} + \vec{k}\vec{v} = 0. \tag{3.1}$$

Now, in case this condition is fulfilled, the absorption is again enabled and the moving atom makes a transition to the excited state, followed by a subsequent return to the ground state emitting a photon after some time τ given by the radiative lifetime of the excited state. If the atom, after the excitation, decays via spontaneous emission, the re-emission of the photon can be in any direction. However, due to parity conservation of the electromagnetic interaction, the spontaneous emission pattern will be spherical over many realisations [30], as shown in Figure 3.1.
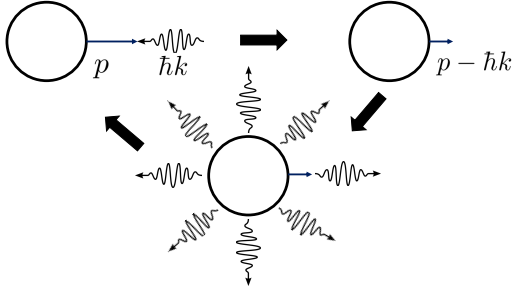

Figure 3.1.: Schematic of the laser cooling process showing an atom of mass m with momentum $p = mv$ moving in opposite direction to the incoming photon with momentum $\hbar k$. The momentum of the photon is transferred to the atom changing the momentum of the atom to $p - \hbar k$. The excited atom decays via spontaneous emission back to the ground state emitting a photon in a random direction.

For each emission of a photon, the atom experiences a recoil. This recoil, as explained in [30] for an atom with mass m is characterised in terms of the so-called recoil velocity v_{rec} and the recoil energy E_{rec} as

$$\vec{v}_{\mathrm{rec}} = \frac{\hbar\vec{k}}{m} \tag{3.2}$$

and

$$E_{\mathrm{rec}} = \frac{\hbar^2 |\vec{k}|^2}{2m}. \tag{3.3}$$

This means due to the symmetry of the re-emission, the recoil momentum experienced by the atom would theoretically average to zero over an infinite number of absorption and re-emission cycles, leading to an overall momentum transfer to the atom into the direction $\vec{k}$ of the incoming photons [30]. In case the laser is propagating in opposite direction as the atoms direction of motion, the photons need to be red-detuned from resonance (frequency below resonance frequency) to fulfil the resonance condition and the interaction leads to a reduction of velocity of the atom. In case the laser is propagating into the same direction as the atoms direction of motion, the photons need to be blue-detuned from resonance (frequency above resonance frequency) and the interaction leads to an enhancement of velocity of the atom. According to [31] the resulting overall net force, known as radiation

pressure, acting on the atom can be described by

$$\vec{F}_{\text{press}} = \hbar \vec{k} \gamma_{\text{ex}}. \tag{3.4}$$

Here γ_{ex} denotes the excitation rate of the atoms which is defined as

$$\gamma_{\text{ex}} = \frac{S_0 \gamma / 2}{1 + S_0 + [2(\delta + \omega_{\text{D}})/\gamma]^2}. \tag{3.5}$$

Here δ denotes the detuning of the laser from resonance and γ denotes the natural transition rate. The parameter $S_0 = I/I_{\text{S}}$ is the ratio of the light intensity I to the saturation intensity I_{S}, also known as on-resonance saturation parameter. The saturation intensity is defined as

$$I_{\text{S}} = \frac{\pi h c \gamma}{3 \lambda^3}, \tag{3.6}$$

where an intensity of I_{S} corresponds to the energy of one photon $\hbar \omega_{\text{l}}$ every two lifetimes $(2/\gamma)$ over the area of the radiative cross section of the two-level transition $(3\lambda^2/2\pi)$ [32]. However, the exact form of this force derives from a phenomenological description of the effect of spontaneous emission on the time evolution of the density operator needed to describe statistically the incoherent or dissipative processes of systems with several atoms. From the steady state solution of the optical Bloch equations, the excited state population corresponding to the excitation rate γ_{ex} at which the momentum transfer of $\hbar k$ occurs can be derived as elaborated in detail in [33] and [34].

The radiation pressure depends on the Doppler shift ω_{D} and is thus velocity depending, which plays a crucial role in the frame of laser cooling. For a better explanation on this velocity dependence, the force F_{press} as a function of the velocity for different saturation parameters is plotted in Figure 3.2 a). As shown, the force does not only act onto atoms moving at v_0 the laser is resonant to, but the strength of the interaction of the laser with an atom moving at v is decaying symmetrically around the velocity v_0. To give a precise definition on where the force is considered to be interacting significantly with the atoms, it is common to use the full width at half maximum (FWHM) of the Lorentzian shaped radiation pressure and to assume that the significant interaction range is limited to atoms that move at a velocity inducing a Doppler shift within the FWHM of the Lorentzian. In the low intensity limit where $I \ll I_{\text{S}}$, the natural decay rate of the excited state is considered to be proportional to the saturation parameter leading to a FWHM of the Lorentzian shaped γ_{ex} of γ. This leads to the condition

$$|\delta + \omega_{\text{D}}| \leq \frac{\gamma}{2}. \tag{3.7}$$

3. Laser Cooling and Deceleration of Erbium Atoms

This broadening of the interaction region is known as natural broadening which is a direct consequence of the finite life time of the excited state. According to the Heisenberg uncertainty principle, spontaneous emission implies a frequency spread $\Delta E \Delta t \sim \hbar$ with $\Delta E = \hbar \omega_a$ [35]. In the velocity frame, this leads to an upper and lower velocity bound for the significant interaction range that is given by

$$\pm v_{B,nat} = v_0 \pm \frac{\gamma}{2k}. \tag{3.8}$$

For intensities in the order of magnitude of the saturation intensity, power broadening needs to be considered and the FWHM changes to $\gamma\sqrt{1 + S_0}$. This leads to the condition

$$|\delta + \omega_D| \leq \frac{\gamma}{2}\sqrt{1 + S_0}. \tag{3.9}$$

In the velocity frame, the velocity bounds of the saturation broadened interaction region can be calculated with

$$\pm v_{B,sat} = v_0 \pm \frac{\gamma\sqrt{1 + S_0}}{2k}. \tag{3.10}$$

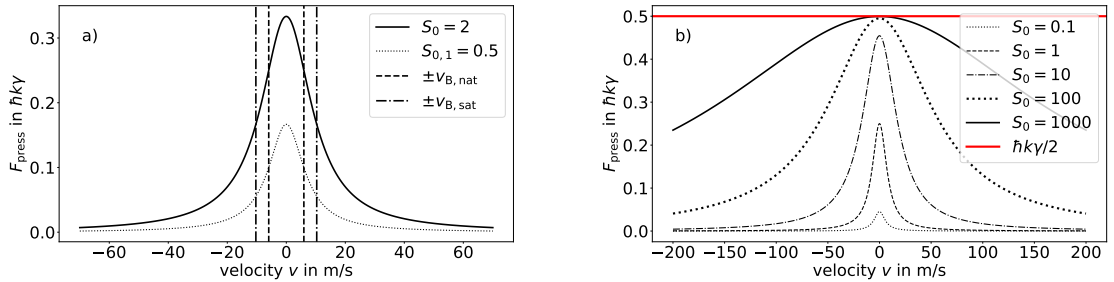**Figure 3.2.:** Velocity dependence of the radiation pressure F_{press} and saturation. The presented radiation pressure F_{press} corresponds to a detuning of $\delta = 0$ from resonance with $\gamma = 2\pi \times 29.7\,\text{MHz}$. In a) the radiation pressure is shown for two different saturation parameters chosen as $S_0 = 2$ (solid line) and $S_{0,1} = 0.5$ (dotted line). The significant interaction bounds $\pm v_{B,nat}$ in the low intensity case and power broadened interaction bounds $\pm v_{B,sat}$ in the high intensity case are indicated as dashed and as dash-dotted line, respectively. In b) the radiation pressure is shown for different saturation parameters chosen as $S_0 = 0.1$ (dotted line), $S_0 = 1$ (dashed line), $S_0 = 10$ (dash-dotted line), $S_0 = 100$ (fat-dotted line) and $S_0 = 1000$ (black solid line). The saturation limit $\hbar k \gamma / 2$ is indicated as red fat solid line.

According to [30], the power broadening results from the absorption-stimulated emission cycles that do not contribute to the force. At really high intensities the light can produce faster absorption, but also causes fast stimulated emission and as the process of absorption and stimulated emission is reversible leading to a conser-

vative force, it cannot be used for laser cooling [31]. This means, the strength of the total radiation pressure is rising until saturation can be observed. The theoretical high intensity limit of the force can be found for $S_0 \to \infty$ as $\hbar k\gamma/2$. This high intensity limit is also known as saturation limit of the force and is fully characterised by the parameters of the chosen transition. The radiation pressure as a function of velocity v is shown in Figure 3.2 b) for different saturation parameters. For rising intensities, the interaction region of the force in velocity-space is broadened and the strength of the force is rising until saturation can be observed.

Now, to understand how laser cooling of atoms is implemented, let us consider a real case scenario. For this example the laser will manipulate the longitudinal motional spread (along the positive $z-$axis) of a thermal atomic beam of erbium atoms $P'_{T_0}(v_z)$ with realistic temperature chosen as $T_0 = 1150\,°C$. This velocity distribution is presented in Figure 3.3.
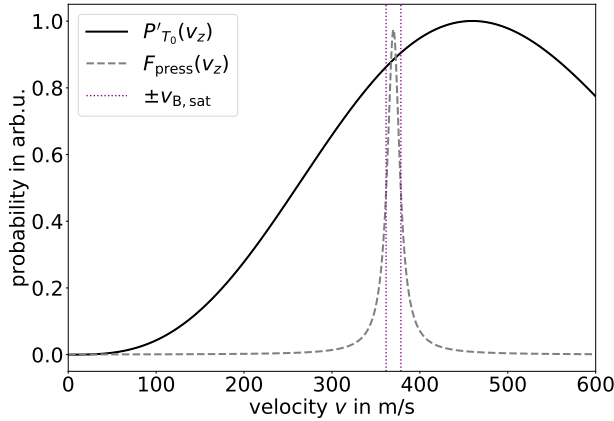

Figure 3.3.: Velocity distribution with indication of the radiation pressure-atom interaction region. The black solid line is the assumed velocity distribution $P'_{T_0}(v_z)$, the grey dashed line shows the velocity dependence of the radiation pressure. The bounds of the significant interaction region given by $\pm v_{B,sat}$ are indicated as vertical dotted purple lines. The relative strength of the interaction probability and the velocity distribution has been chosen arbitrarily in this figure. For a quantitative picture it would be necessary to assign a certain number of atoms distributed among the relevant velocity classes and to assume a time frame in which the laser is acting on the atoms. This picture is only thought to give an intuitive picture regarding the velocity spread within the interaction region.

Furthermore, let us assume the laser propagates along the negative $z-$axis and has a detuning δ from the atomic transition frequency ω_a that compensates the Doppler shift of an atom moving at a velocity $v_0 = 370\,\text{m/s}$. In addition, let us assume the laser drives the 401 nm transition and has an intensity $I = I_S$ leading to a saturation parameter of $S_0 = 1$. The velocity dependence of the force F_{press}

for the given parameters is shown in Figure 3.3. The Lorentzian shaped excitation rate, which can be understood as interaction probability density in velocity space, characterises the strength of the interaction for each velocity. For the given parameters, the laser would interact significantly with atoms from the distribution having a velocity within the saturation broadened velocity bounds $v_{\mathrm{B,sat}} \approx 370\,\mathrm{m/s}\pm 8.42\,\mathrm{m/s}$, as indicated in Figure 3.3. The interaction with the laser would lead to a deceleration of the atoms below the lower velocity bound after a certain number of absorption and spontaneous re-emission cycles.

3.2. Optical Molasses using the 401 nm Transition in Erbium

The first optical molasses has been observed by a group at Bell Laboratories in 1985 [36]. In principle, the optical molasses is based on the concept of diffusive atomic motion that occurs under the influence of a laser cooling process producing a significant damping force.

For the following explanations, let us assume a two level atom interacting with a pair of counter propagating laser beams and let us recall the previously introduced definitions. The energy difference between the ground state and the excited state in units of frequency is given by ω_{a}. The population of the excited state decays radiatively at a rate γ.. The laser beams have an angular frequency of ω_{l} leading to a detuning of the laser beams from the atomic transition $\delta = \omega_{\mathrm{l}} - \omega_{\mathrm{a}}$. The coupling between the ground state and the excited state induced by the laser beam of intensity I is characterised in terms of the saturation intensity I_{S} of the atomic transition. The atom moving at a certain velocity v sees a Doppler shifted frequency of the laser light leading to a velocity dependent force known as radiation pressure. Let us extend the form of this force to the relative motion of the atom into the direction of the velocity vector $\vec{v}$ with respect to the direction of the wave vector $\vec{k}$. In case of two counter-propagating plane waves, the average force induced by a plane wave propagating in positive direction (leading to F_+) or in negative direction (leading to F_-) is given by

$$F_{\pm} = \pm \hbar k \frac{\gamma}{2} \frac{I/I_{\mathrm{S}}}{1 + I/I_{\mathrm{S}} + [2(\delta \mp kv)/\gamma]^2}. \tag{3.11}$$

Both forces, F_+ and F_-, acting on atoms moving at a velocity v in direction $\vec{v}$ with respect to a laser propagating along $\vec{k}$ with $\vec{k}\vec{v} = -kv$ are shown in Figure 3.4.
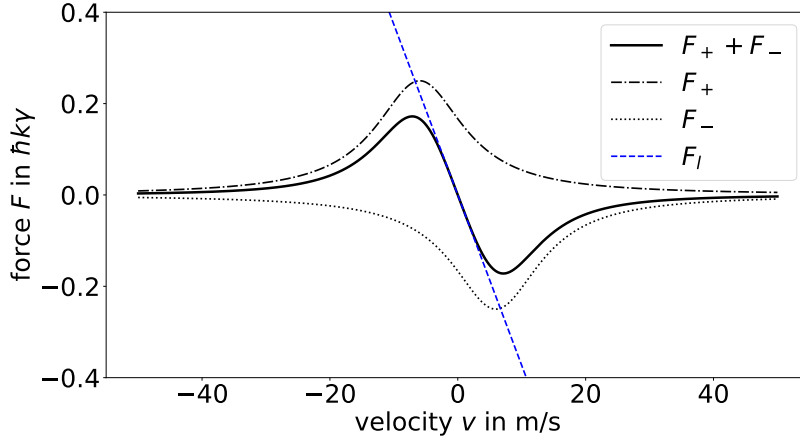
Figure 3.4.: Radiation pressure acting as optical molasses. The forces shown in this figure induced by two counter-propagating plane waves, F_+ (black dash-dotted line) and F_- (black dotted line) have parameters corresponding to the 401 nm transition and a saturation parameter $S_0 = 1$. The detuning is $\delta = -\gamma/2$. The overall acting force $F = F_+ + F_-$ is indicated as black solid line. The approximation of the average force $F_l = -\alpha v$ with damping coefficient α is indicated as blue dashed line.

Under the assumption that the two light waves act independently, the overall acting net force can be written as $F = F_+ + F_-$. In the low intensity limit $I/I_S << 1$, the average force $F = F_+ + F_-$ can be approximated as

$$F = \frac{\hbar k \gamma}{2} \frac{I}{I_S} \frac{kv}{\gamma} \frac{16\delta/\gamma}{1 + \frac{8}{\gamma^2}(\delta^2 + k^2 v^2) + \frac{16}{\gamma^4}(\delta^2 - k^2 v^2)}. \tag{3.12}$$

For $|kv| << \gamma$ and $|kv| << |\delta|$ Equation (3.12) simplifies to

$$F_l = 4\hbar k \frac{I}{I_S} \frac{kv(2\delta/\gamma)}{[1 + (2\delta/\gamma)^2]^2}. \tag{3.13}$$

This force, which corresponds to a linear approximation valid for small velocities, is damping for all velocities if $\delta < 0$, and writing the damping force in the common form $F_l = -\alpha v$ leads to the so-called damping coefficient

$$\alpha = -4\hbar k^2 \frac{I}{I_S} \frac{2\delta/\gamma}{[1 + (2\delta/\gamma)^2]^2}, \tag{3.14}$$

as explained in [37].

The effect of changing the detuning δ on the damping force given by $F = F_+ + F_-$ is shown in Figure 3.5 a). The central region between the two extrema of the force (maximum to minimum) can be understood as the velocity capture region where

the optical molasses is acting as a damping force on the atoms. For a small detuning, the resulting force has a steep gradient in the central region leading to a large damping coefficient α, but to a small velocity capture region. For a large detuning, the gradient is less steep, but the velocity capture region is larger.

Furthermore, the effect of changing the saturation parameter S_0 on the damping force is shown in Figure 3.5 b). For small values of the saturation parameter the resulting force is small, but also the velocity range within the velocity distribution the atoms are part of is narrow, leading to a small fraction of atoms that can be damped. For too large values of the saturation parameter a large fraction of atoms can be cooled, but the strength of the force is small as the spectral line is significantly broadened.
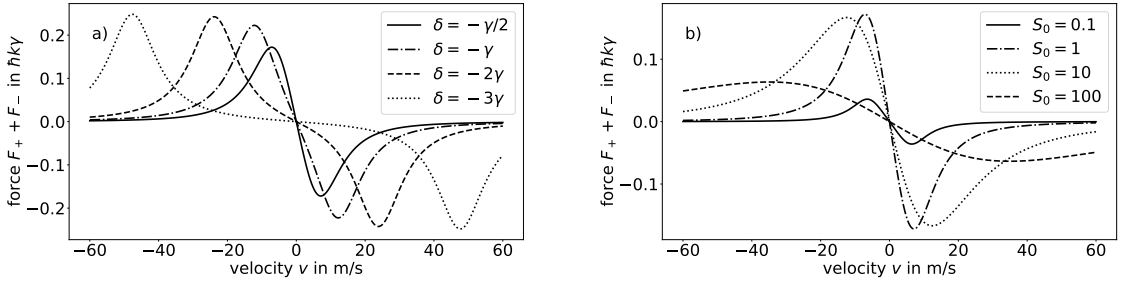

Figure 3.5.: Damping force $F = F_+ + F_-$ for different values of the detuning and for different values of the saturation parameter for the parameters corresponding to the 401 nm transition. In a), the effect of changing the detuning δ on the damping force for a chosen saturation parameter of $S_0 = 1$ is shown. The dotted line corresponds to a detuning of $\delta = -\gamma/2$, the dashed line to $\delta = -\gamma$, the dash-dotted line to $\delta = -2\gamma$ and the solid line to $\delta = -3\gamma$ In b) the effect of changing the saturation parameter S_0 on the damping force for a chosen detuning for $\delta = -\gamma/2$ is depicted. The solid line corresponds to $S_0 = 0.1$, the dash-dotted line to $S_0 = 1$, the dotted line to $S_0 = 10$ and the dashed line to $S_0 = 100$.

Additionally, the dependence of the damping coefficient α on the saturation parameter S_0 is shown in Figure 3.6 for different values of the detuning. Looking again at Equations (3.13) and (3.14) reveals that the acting damping force is maximal in case the damping coefficient is minimal. For each detuning δ, the damping coefficient is minimal at a certain value of S_0. From an experimental point of view it is common to optimise the detuning of the laser for the given intensity of the light. In case of an intensity of the laser of $I = 2I_S$, the optimal detuning of the laser in order to maximise the damping force would be expected to be found between $-1/3\gamma$ and $-1/2\gamma$.
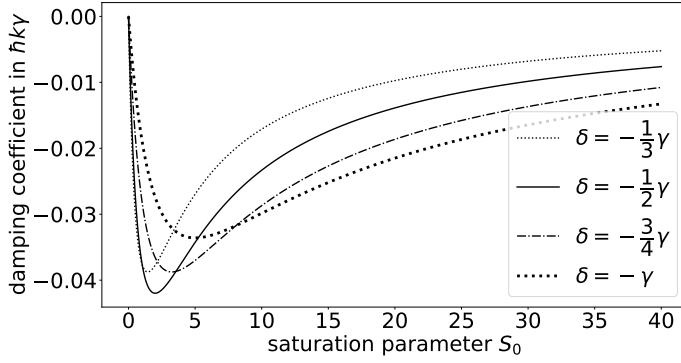
Figure 3.6.: Dependence of the damping coefficient α on the saturation parameter S_0 for four different values of the detuning chosen as $\delta = -1/3\gamma$ (black dotted line), $\delta = -1/2\gamma$ (black solid line), $\delta = -3/4\gamma$ (black dash-dotted line) and $\delta = -\gamma$ (black fat dotted line).

As explained in [38], the narrowed velocity distribution resulting from the action of the laser onto the thermal velocity distribution can be found as a stationary solution of the Fokker-Planck equation including the damping force as well as momentum diffusion leading to

$$P''_{T_{\text{eff}}}(v) = \frac{1}{\sqrt{\pi}u} \exp\left(-\frac{v^2}{u^2}\right). \tag{3.15}$$

Here u denotes the half-width of the steady state velocity which is defined as

$$u = \frac{2k_{\text{B}}T_{\text{eff}}}{m}. \tag{3.16}$$

The half-width of the steady state velocity is characterised by the effective temperature, that can be approximated as

$$T_{\text{eff}} = \frac{\hbar\gamma}{2k_{\text{B}}} \left(\frac{|\delta|}{\gamma} + \frac{\gamma}{|\delta|}\right). \tag{3.17}$$

This means the force acting on the atoms can reduce their kinetic energy. However, the random walk in momentum space with step size $\hbar k$ that occurs at a scattering rate $\gamma_{\text{ex}} = S_0\gamma/2$ in case of $\delta = 0$ and $S_0 << 1$ induces heating. Thus, the cooling performance is limited. As explained in [38], the minimum effective temperature T_{eff} is reached for a detuning $\delta = -\gamma$ leading to a minimum temperature, known as Doppler temperature, of

$$T_{\text{Doppler}} = \frac{\hbar\gamma}{2k_{\text{B}}}.$$

This means, the minimal temperature surprisingly only depends on the linewidth

of the chosen transition. The Doppler temperatures of the transitions that hold relevance to this research project are listed in Table 2.2.

3.3. Transversal Cooling: An Application of the Optical Molasses

As shown, the optical molasses can be used to deform the motional spread of a sample of atoms along the direction of propagation of the light. In case the interaction of the laser with the atoms would lead to a compression of the velocity distribution, the deceleration towards smaller velocities is also known as laser cooling, as the thermodynamic temperature of an ensemble of atoms is proportional to the variance of the atom velocities. In case the action of the light leads to an acceleration to higher atom velocities, the velocity distribution is decompressed by the laser light which is called laser heating.

An intuitive picture of the narrowing of the motional spread of an atomic beam represented by the Maxwell-Boltzmann velocity distribution $P'_T(v_x)$ is given in Figure 3.7 a). For the given detuning δ and the given natural decay rate γ, the light decelerates the atoms within the interaction region below the lower interaction bound. Choosing a larger detuning means choosing a fraction of atoms with larger velocity that are decelerated by the optical molasses, but also cooling to a larger effective temperature. However, in case of a blue-detuned laser beam acting on the atoms inducing transversal heating, the given velocity distribution will be deformed similarly as shown in Figure 3.7 b) leading to an enhancement of atoms being part of the velocity distribution at larger velocities.

For the transversal cooling mechanism used experimentally, this concept of the one-dimensional optical molasses is extended to two dimensions. There the transversal motional spread of an atomic beam is manipulated utilising two pairs of red-detuned counter propagating laser beams leading to narrowing of the velocity distribution.
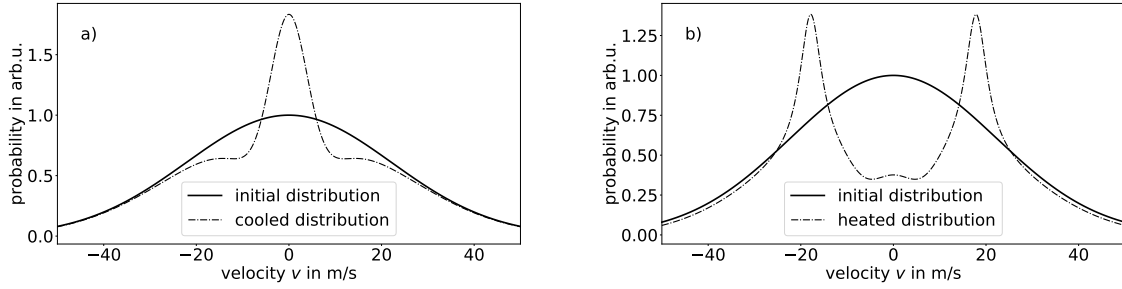
Figure 3.7.: Intuitive picture of the deformation of velocity distribution of an atomic beam $P'_T(v_x)$ with reduced temperature $T = 10\,\mathrm{K}$ by a laser with a chosen detuning of $\delta = \pm\gamma/2$, a saturation parameter chosen as $S_0 = 1$ and parameters of the 401 nm transition. In a) (b)) for the given detuning $\delta < 0$ ($\delta > 0$) the light decelerates (accelerates) the atoms within the interaction region beyond the inner (outer) interaction bounds. Thus the fraction of atoms subtracted from the distribution in the interaction regions is re-added in the center (beyond the outer interaction bounds) of the distribution.

3.4. Magneto-Optical Trapping

In case of an extension to three dimensions involving three pairs of counter propagating laser beams, the lasers act as a viscous confinement, where the atoms can dissipate their energy. Such a three dimensional molasses is cooling as it is leading to a reduction of the mean velocity, however it is not trapping as the molasses is not implementing a restoring force in position space. This means, the atoms can spatially diffuse out of the molasses [36]. Therefore, it is common to add a trapping mechanism. For atoms with some net magnetic dipole moment the trapping mechanism can be implemented introducing a magnetic field with a local minimum, as e.g. a quadrupole field, an Ioffe-Pritchard field, or other configurations [38]. One prominent trapping technique is the so-called magneto-optical trap (MOT) firstly realised in 1987 [39]. It consists of an optical molasses in three dimensions which is implemented by three intersected orthogonal pairs of red detuned counter-propagating laser beams with opposite circular polarisation in combination with a quadrupole field being zero at the center and increasing in magnitude in all directions. Such a magnetic field can simply be produced by constructing two coils in an anti-Helmholtz like configuration (the distance between the two coils does not have to be equal to the radius of the coils, but the current is running in opposite direction through the coils). A precise explanation on this trapping scheme including also explanations on the polarisation needed to drive the right transition can be found in [40].

As already explained, the optical molasses can effectively cool atoms to very low temperatures, also known as the Doppler temperature, which is $T_\mathrm{D} = 4.6\,\mathrm{\mu K}$ in

case of the TREQS experiment utilising the narrow-line transition near 583 nm. The narrow linewidth in combination with the large mass of erbium leads to an asymmetric MOT density distribution, where atoms accumulate at the bottom of the trap due to gravity. As explained in [11], [41] and demonstrated in [42], the laser beam propagating into the direction of the gravitational force can be removed without disturbing the proper functionality of the magneto-optical trapping mechanism.

However, the magnetic field design of the MOT defines a certain capture velocity which can be understood as maximum velocity of the atoms that can be reduced to stop within the profile of the MOT beams. As explained in [43], under the assumption that the atoms scatter photons at a maximum rate of $\gamma/2$ across the entire MOT beam diameter D, the capture velocity can be estimated as

$$v_{\mathrm{c}}^{\mathrm{MOT}} = \sqrt{2\frac{\hbar k \gamma}{2m}D}.$$

In case of the TREQS experiment it is given by $v_{\mathrm{c}}^{\mathrm{MOT}} = 5.6\,\mathrm{m/s}$.

3.5. Zeeman slower for bosonic Erbium

Since its first realisation in 1982 [44], the Zeeman slower represents one of the most popular technologies used for slowing thermal beams consisting of neutral atoms along their direction of propagation, down to velocities where they can be trapped.

Working principle

The general idea of this technology is to exert a strong light force in opposite direction of the atom's direction of propagation by shining a counter-propagating laser beam onto the atomic beam. The deceleration of the atoms, implemented by the radiation pressure, leads to a changing Doppler shift. If this change in Doppler shift is larger than the natural decay rate of the excited state γ of the atomic transition chosen for the cooling process, the resonance condition cannot be maintained. Thus the laser is considered to be off-resonance and does not significantly interact with the atoms anymore. To keep the radiation pressure acting on the atoms without changing the frequency of the laser, one possibility is to change the difference between the energy levels that is characterised by the transition frequency ω_{a}. This can be implemented by making use of the so-called Zeeman effect.

According to [11], every energy level of an atom represented by the total angular momentum quantum number J is split into $2J+1$ Zeeman sub states in case of an applied external magnetic field of strength B. The degeneracy of the Zeeman levels in a bosonic isotope represented by the magnetic quantum numbers m_J ranging

from $-J$ to J is lifted according to

$$\Delta E_B = m_J g_J \mu_{\mathrm{B}} B \tag{3.18}$$

with $m_J g_J \mu_{\mathrm{B}} = \mu$ being the magnetic moment. To explain how this shift of the energy levels can be used to compensate the changing Doppler shift, let us consider the simplest theoretical case of a two-level atom and let us introduce the notation $|J, m_J\rangle$. The ground state (g) of the chosen atom has a total angular momentum $J_{\mathrm{g}} = 0$ and the excite state (e) has a total angular momentum of $J_{\mathrm{e}} = 1$. As explained, in presence of a magnetic field the energy levels are split into Zeeman sub states. For the ground state $\Delta E_B = 0$ and the only state in presence of the magnetic field is $|0, 0\rangle$. For the excited state with $J = 1$ the degeneracy is lifted into three Zeeman sub states $|1, -1\rangle$, $|1, 0\rangle$ and $|1, 1\rangle$. To drive a transition to the excited state the condition $\Delta m_J = 0, \pm 1$ needs to be fulfilled. This means a transition from the ground state is allowed to all three excited Zeeman states. A transition from $|0, 0\rangle$ to $|1, +1\rangle$ is a so-called σ^+ transition, a transition from $|0, 0\rangle$ to $|1, -1\rangle$ is known as σ^- transition. It needs to be mentioned that the convention of σ^+ and σ^- transition depends strongly on the chosen quantisation axis with respect to the direction of the magnetic field, as the magnetic quantum number m_J corresponds to the projection of J onto the quantisation axis. In the following, the quantisation axis is chosen along the magnetic field vector of the applied magnetic field.

There are different types of Zeeman slowers depending on the different magnetic fields that define which transition is being driven. One type is the so-called decreasing field slower that works in case σ^+ transition are driven, as it has been realised eg. in [44] decelerating Na atoms in an atomic beam. The second type is the increasing field slower that works in case of σ^- transitions as implemented in [45] for Rb atoms. In case of the TREQS experiment a Zeeman slower in the so-called spin-flip configuration is used, providing a decreasing field in the first part of the slower where σ^+ transition are driven and an increasing field in the second part of the slower where σ^- transition are driven. Furthermore, also Zeeman slowers with transverse magnetic field provided by permanent magnets have been realised, as e.g. studied in [46] with a Zeeman slower for sodium atoms in a Halbach configuration or in [47] showing successful Zeeman slowing of a group-III atom.

Before explaining the working principle of the Zeeman slower more precisely, it needs to be introduced how such transitions (σ^- and σ^+ transitions) are defined and how they can be driven. Let us consider a laser propagating along $\vec{k}$. The polarisation of the laser is defined by the orientation of the electric field vectors with respect to the $\vec{k}$-vector. In the context of σ^- and σ^+ transitions, circular polarisation is needed to drive the transition. As indicated in Figure 3.8, in case of circular polarisation, the electric field vectors $\vec{E}$ of the light rotate constantly and clockwise (left-handed polarisation) or counter-clockwise (right-handed polari-

sation) in a plane perpendicular to the $\vec{k}$-vector of the light. Now, let us introduce a homogeneous magnetic field with orientation given by the $\vec{B}$-vector and let us choose the quantisation axis into the direction of the magnetic field. As shown in Figure 3.8, a σ^+ transition is driven in case the $\vec{k}-$vector of the light and the $\vec{B}-$vector point into the same direction and the light has right-handed polarisation. For a σ^- transition the light needs to have left-handed polarisation.
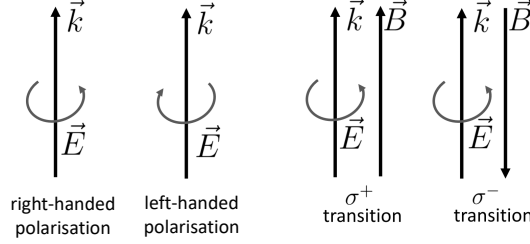

Figure 3.8.: Definition of circular left-handed and right-handed polarisation indicating the direction of rotation of the electric field vectors $\vec{E}$ with respect to the direction of propagation of the laser $\vec{k}$ and introduction of σ^- and σ^+ transitions in dependence of the chosen quantisation axis.

Now, to understand the working principle of the Zeeman slower, let us assume the laser with frequency ω_l is detuned by δ from the atomic transition frequency of the simple two-level atom ω_a in order to interact with atoms moving at a velocity v_1 inducing some Doppler shift $\hbar\omega_{\mathrm{D}_1}$. If the atoms are decelerated to a velocity v_2 inducing a Doppler shift $\hbar\omega_{\mathrm{D}_2}$ that is larger than the natural decay rate of the excited state γ, the laser does not significantly interact with the atoms anymore. Now, let us introduce a static and spatially varying magnetic field which is assumed to decrease linear along the $x-$axis chosen into the same direction as the atoms direction of motion. For the following explanations the magnetic field is of the form $B(x) = B_0(1 - x/x_0)$ with $B_0 > 0$ and x_0 is the length of the slower. The resonance condition now reads

$$\omega_\mathrm{a} - kv(x) + \frac{\mu' B(x)}{\hbar} = \omega_\mathrm{l}. \tag{3.19}$$

Here $\mu' = g_\mathrm{e}m_\mathrm{e} - g_\mathrm{g}m_\mathrm{g}$ denotes the difference of the magnetic moments between the ground state (g) and the excited state (e) with g_e and g_g being the Landé g-factors and m_e and m_g the magnetic quantum numbers of the excited state and the ground state, respectively. For the assumed linearly decreasing magnetic field, the polarisation needs to be chosen in order to drive σ^+ transitions. The resulting splitting of the $|1, 1\rangle$ state with respect to the $|0, 0\rangle$ ground state along x for the chosen magnetic field will be of the form as shown in Figure 3.9 in case of an arbitrarily chosen Landé g-factor of the excited state $g_\mathrm{e} > 0$. According to Equation (3.19), the detuning δ of the laser needs to be chosen such that the laser compensates the energy difference of the ground state $|0, 0\rangle$ and the excited state $|1, 1\rangle$ for the

maximum Doppler shift (velocity) the slower is designed to decelerate. This energy difference is Zeeman shifted in presence of the magnetic field of strength B_0 at the start position of the slower. The maximum velocity the Zeeman slower is designed to decelerate is the so-called capture velocity of the Zeeman slower $v_{\text{capt,ZS}}$. This capture velocity can be understood as the upper bound of the atoms being part of the thermal velocity distribution that are slowed efficiently inside the Zeeman slower.

As the magnetic field in this example is decreasing, at each position along the x-axis a different resonance condition needs to be fulfilled. Thus, for atoms with dropping velocity and dropping Doppler shift along x there will be a position where the resonance condition is fulfilled. This is the case if $\Delta E_B(x)_{\text{max}} - \Delta E_B(x)_{\text{min}}$ is equal to the desired velocity range in energy space $\hbar\omega_{\text{D,v}_{\text{max}}} - \hbar\omega_{\text{D,v}_{\text{min}}}$.
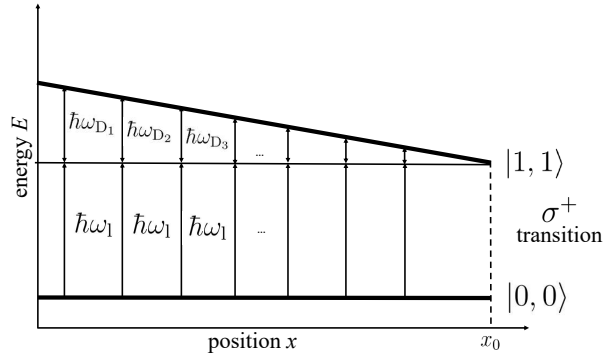

Figure 3.9.: Zeeman splitting of the $|1,1\rangle$ for a magnetic field decreasing linearly along the $x-$axis with constant laser energy $\hbar\omega_{\text{l}}$ for the compensation of a changing Doppler shift.

The deceleration $a(x)$ of an atom of mass m after the introduction of the magnetic field $B(x)$ can be calculated from $F_{\text{press}}(x) = ma(x)$ analogous to Equation (3.5) by adding the magnetic shift as

$$a(x) = \frac{\hbar k\gamma}{2m} \frac{S_0}{1 + S_0 + 4[\delta + \omega_{\text{D}} + \mu'B(x)/\hbar]^2/\gamma^2}. \tag{3.20}$$

The maximum deceleration is achieved when the atoms are on resonance and the sum of the induced Doppler shift, the laser frequency ω_{l} and the Zeeman shift $\mu'B(x)/\hbar$ corresponds to the transition frequency $\omega_{\text{a}} = \omega_{\text{l}} - \omega_{\text{D}} - \mu'B(x)/\hbar$. This results in

$$a_{\text{max,sat}} = \frac{\hbar k\gamma}{2m} \tag{3.21}$$

in the high intensity limit. To achieve a constant deceleration of the atoms, the velocity needs to follow a square-root dependence on the position x of the form

$$v(x) = v_{\text{capt,ZS}}\sqrt{1 - \frac{x}{x_0}}. \qquad (3.22)$$

Here, x_0 corresponds to the length of the Zeeman slower, which cannot be chosen arbitrarily, as explained in [48]. Looking at Equation (3.21) and under consideration of Newton's law of motion, the minimal distance needed to decelerate an atom from a velocity v_{max} to a velocity v_{min} for scattering events at a rate γ with momentum transfer $\hbar k$ is given by

$$x_0 = m\frac{v_{\text{max}}^2 - v_{\text{min}}^2}{\hbar k \gamma}. \qquad (3.23)$$

To fulfil the resonance condition given in Equation (3.19) and knowing that the Doppler shift follows a square-root dependence on the position, also the Zeeman shift needs to follow the same square-root dependence. This leads to an ideal form of the magnetic field which is

$$B(x) = B_{\text{B}} + B_0\sqrt{1 - \frac{x}{x_0}}, \qquad (3.24)$$

with overall height of the profile B_0 and bias field B_{B}. The choice of the bias field depends on the Zeeman slower type: For the increasing field slower $B_{\text{B}} = -B_0$, for the decreasing field slower $B_{\text{B}} = 0$ and for the Zeeman slower in spin-flip configuration $0 < |B_{\text{B}}| < |B_0|$. In an experimental setup those ideal conditions are never reached exactly. Thus it is common to introduce a so-called security parameter η accounting for deviations from the ideal shape of the magnetic field in the design of the Zeeman slower. This security parameter is defined as

$$\eta = \frac{a(x)}{a_{\text{max,sat}}}. \qquad (3.25)$$

This parameter accounts for the fact that the deceleration of the atoms depends on the number of scattering events in each section of the Zeeman slower, that is limited by the finite intensity of the light. Furthermore, this parameter accounts for deviations of the real magnetic field from the ideal magnetic field. According to [48], the security parameter is related to the finite intensity as

$$\frac{I}{I_{\text{S}}} = \frac{\eta}{1 - \eta},$$

whereas

$$\eta = \frac{2M\mu'}{\hbar^2 k \gamma}\frac{\text{d}B}{\text{d}x}\left(\frac{\mu'B}{\hbar} - \delta\right)$$

relates the security parameter to the slope of the magnetic field. Theoretically, the Zeeman slower is only working properly if the slope of the magnetic field $\text{d}B/\text{d}x$

does not exceed the slope of the ideal magnetic field as stated in Equation (3.24). Therefore, in practice the Zeeman slower is usually significantly longer than the theoretical minimum length to ensure that the slope of the magnetic field at each point is always smaller than the theoretical ideal value.

TREQS Zeeman slower

The Zeeman slower used in the TREQS experiment is in a so-called spin-flip configuration with a decreasing field in the first part and an increasing field in the second part. The advantage of this configuration is that the total magnetic field strength B has lower values, as only the relative splitting of the states is of importance for the compensation of the Doppler shift. The relative splitting is characterised by the peak-to-peak magnetic field strength B_{pp} and thus also lower currents running through the coils are needed. This reduces the heating of the coils. Furthermore, the comparatively small magnetic field of the Zeeman slower is less disturbing to the proper functionality of other sections of the experiment. The calculated magnetic field of the Zeeman slower is shown in Figure 3.10.
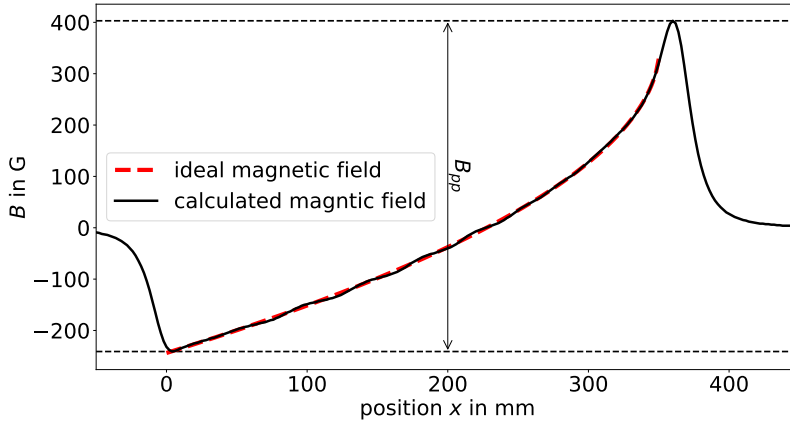

Figure 3.10.: Magnetic field of the Zeeman slower used in the TREQS experiment. The black solid line indicates the magnetic field obtained theoretically for the Zeeman slower calculated from the coil design and for the designed currents given in [49]. The negative sign of the magnetic field strength indicates opposite orientation of the quantisation axis (magnetic field vector) with respect to the direction of propagation of the laser beam. The red dashed line corresponds to the ideal magnetic field following the square-root dependence on the position (Equation (3.24)) with parameters $B_{\mathrm{B}} = 354\,\mathrm{G}$, $B_0 = -598\,\mathrm{G}$ and $x_0 = 350\,\mathrm{mm}$. The black arrow indicates the peak-to-peak magnetic field strength B_{pp}.

The TREQS Zeeman slower uses the transition near $401\,\mathrm{nm}$ in erbium with a maximum deceleration of $a_{\mathrm{max,sat}} = 6.6 \times 10^5\,\mathrm{m/s^2}$ and a minimal length of approx-

imately $x_0 = 12.4$ cm. Comparing the real case scenario of the TREQS experiment to the theoretical introduction on the working principle of the Zeeman slower in the first part of this section, it is not only the shape of the magnetic field that is not simply linear, but also the simple understanding of a two-level atom breaks down in the real case of an ensemble of erbium atoms undergoing this deceleration process. As already mentioned in Section 2.3, the transition from the ground state $[4f^{12}(^3\mathrm{H}_6)6s^2(^1\mathrm{S}_0)]_6$ to the excited state $[4f^{12}(^3\mathrm{H}_6)6s6p(^1\mathrm{P}_1)]_7$ is used for the cooling process. The ground state of erbium has a total angular momentum quantum number of $J = 6$, the chosen excited state $J = 7$. In presence of the magnetic field these states are split into 13 Zeeman substates for the ground state and 15 Zeeman substates for the excited state. The calculated Zeeman splitting is shown in Figure 3.11 as a function of the magnetic field strength B.
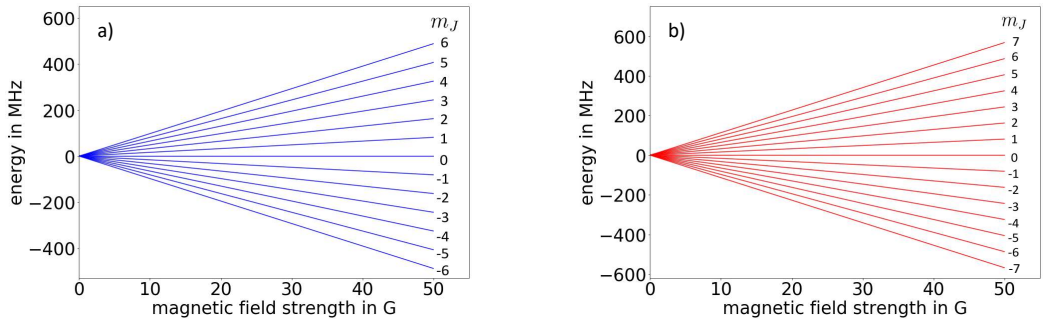

Figure 3.11.: Zeeman splitting of the states of the cooling transition used for the Zeeman slower calculated with Equation (3.18) with Landé g-factors given in Section 2.4. In a) Zeeman splitting of the ground state of erbium $[4f^{12}(^3\mathrm{H}_6)6s^2(^1\mathrm{S}_0)]_6$ with total angular momentum quantum number $J = 6$ and in b) Zeeman splitting of the excited state of erbium $[4f^{12}(^3\mathrm{H}_6)6s6p(^1\mathrm{P}_1)]_7$ with total angular momentum quantum number $J = 7$.

However, as shown, there is a large number of transitions that can be driven (all transitions with $\Delta m_J = +1$ in the decreasing field section and $\Delta m_J = -1$ in the increasing field section) as the atoms entering the Zeeman slower do usually occupy all Zeeman states. In case σ^+ transitions are driven with $\Delta m_J = +1$ the magnetic quantum number is always enhanced by one in each excitation, but does not necessarily decrease by one in each decay as the dipole selection rules for the decay state $\Delta m_J = 0, \pm 1$. This means the atoms are optically pumped into the stretched states and after a few absorption and spontaneous re-emission cycles mostly the transition $|6, +6\rangle \rightarrow |7, +7\rangle$ will be driven ($|6, -6\rangle \rightarrow |7, -7\rangle$ in the increasing field section).

As already explained, the change in Doppler shift in a range $\hbar\omega_{\mathrm{D,v_{max}}} - \hbar\omega_{\mathrm{D,v_{min}}}$ needs to be compensated by the change in Zeeman shift given by the relative change in splitting between the ground state and the excited state. The Zeeman shift obtained for the calculated magnetic field of the TREQS experiment along the position x for the transition $|6, +6\rangle \rightarrow |7, +7\rangle$ if $B < 0$ and $|6, -6\rangle \rightarrow |7, -7\rangle$ if

$B > 0$ is shown in Figure 3.12. In the upper plot, the energy difference ΔE_B between the Zeeman split state and the non-split state (degenerate state in absence of the magnetic field) is shown for the ground state and the excited state. Furthermore, the relative change between the two split states $\Delta E_{B_e} - \Delta E_{B_g}$ is shown. The lower plot contains only the relative Zeeman shift on the MHz scale, which should be equal for all allowed σ^+ (σ^-) transitions in the decreasing field section (increasing field section). To decelerate atoms moving at a velocity $v_{\text{capt,ZS}} = 370\,\text{m/s}$, a Doppler shift of $\omega_D = 2\pi\nu_D$ with $\nu_D = 923\,\text{MHz}$ needs to be compensated. This means, the laser needs to be detuned by $-\nu_D + \nu_B = -539\,\text{MHz}$ from the transition frequency $\nu_a = \omega_a/2\pi$.
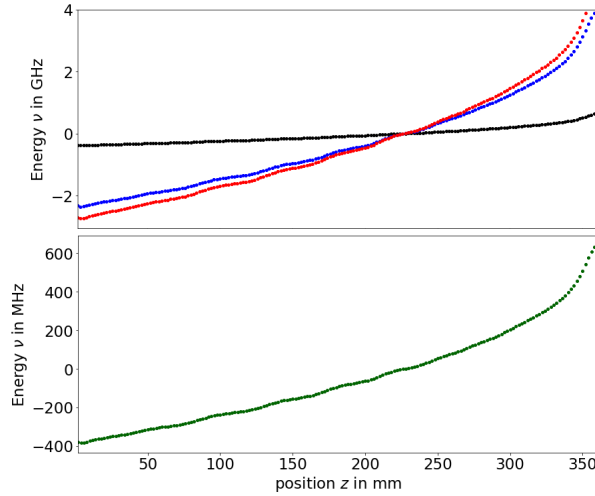

Figure 3.12.: In the upper plot, energy difference $\Delta E_B = h\nu_B = \hbar\omega_B$ between the Zeeman split state and the non-split state for the ground state (blue) and the excited state (red) and relative change between the two split states $\Delta E_{B_{ex}} - \Delta E_{B_{gs}}$(black). The minimum of the relative Zeeman shift is given by $-384\,\text{MHz}$ and the maximum is given by $641\,\text{MHz}$. To compensate the Doppler shift for atoms moving at a velocity of $370\,\text{m/s}$ to a velocity of $5\,\text{m/s} < v_c^{\text{MOT}}$ (designed target velocity), the relative Zeeman shift needs to change by $910\,\text{MHz}$. The lower plot contains only the relative Zeeman shift on the MHz scale.

Given our knowledge of the radiation pressure and the working principle of a Zeeman slower, we can estimate the what the velocity distribution resulting at the end of the slowing process should look like. An intuitive picture on the deformation of the thermal longitudinal velocity distribution characterising the motional spread $P_{T_0}(v_x)$ of an erbium atomic beam (along the positive $x-$axis) with realistic temperature chosen as $T_0 = 1150\,°\text{C}$, achieved with the Zeeman slower (with light propagating along the negative $x-$axis), is shown in Figure 3.13. Atoms being part of the thermal velocity distribution with velocity smaller than the capture velocity of the Zeeman slower, would be decelerated until the laser is off-resonant. The part

of atoms of the distribution within the interaction range of the laser would then reappear being part of the distribution below the lower interaction bound.
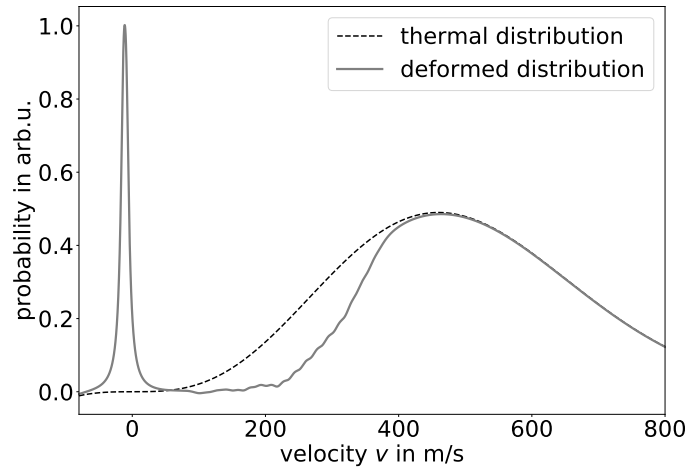

Figure 3.13.: Intuitive picture on the deformation of the longitudinal motional thermal spread of an erbium atomic beam achieved with the Zeeman slower. The initial thermal longitudinal velocity distribution is indicated as black dashed line, a sketch of the deformed distribution resulting from the effect of the Zeeman slower onto the thermal distribution is indicated as grey solid line.

4. Setup of the TREQS experiment

In this chapter the experimental setup of the TREQS is presented. The first section focusses on the laser setup of the 401 nm laser used for the differential spectroscopic measurement performed for the experimental part of this thesis, providing the lasers needed for the individual laser cooling mechanisms. Furthermore, the laser setup of the 583 nm laser used for the fluorescence imaging measurement in the experimental part is discussed. The second section presents the entire setup of the experiment, delving into the technical details of the individual vacuum parts, as well as into the required special features of the experiment to achieve a tweezer-trappable ensemble of erbium atoms.

4.1. Laser system

This section describes the laser setups providing light to perform laser cooling on the two relevant atomic transitions presented in Section 2.3. Both setups have been used for the measurements. Thus, a brief overview of the laser systems is given in order to get a better understanding of the characterisation and optimisation measurements that will be presented in Chapter 5.

401 nm setup

The optical setup of the 401 nm laser system was constructed based on the previously used laser system presented in [50] and is shown in Figure 4.1. The SHG frequency-doubled tapered-amplified (TA) diode laser TA-SHG pro operates at 802 nm. This system provides the laser light used for the Zeeman slower (ZS), the transversal cooling (TC), the spectroscopy (SPEC) measurement in the beam shutter section and the imaging (IMG). The frequency of the laser system is stabilised by locking the laser to a dispersive signal of a hollow-cathode lamb generated performing modulation transfer spectroscopy at the reference cell, as explained in [49]. The frequency of the laser is scanned by passing double-pass acousto-optic modulator (AOM) systems in the individual laser paths. The laser lights of the individual paths are transported to the intended positions of the ultra-high vacuum apparatus by coupling them into polarisation-maintaining single mode fibers. The frequency of the light is measured with a fiber-coupled wavemeter.
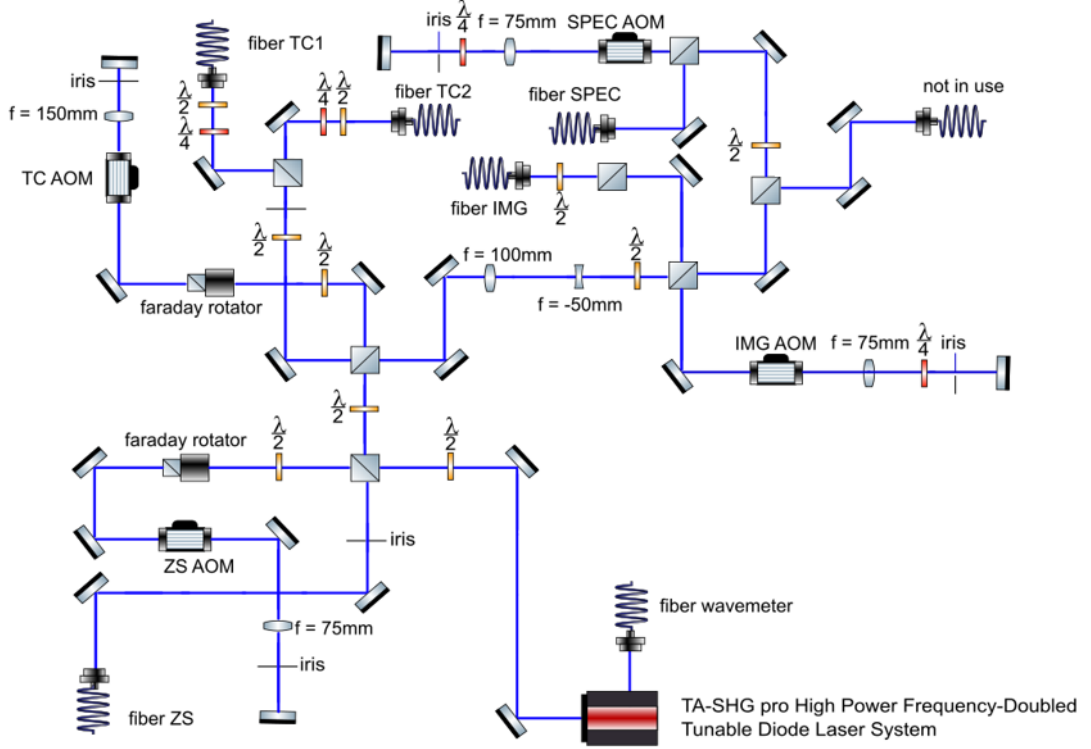
Figure 4.1.: Optical setup of the 401 nm laser. The frequency-doubled tapered-amplified diode laser TA-SHG pro operates at 802 nm. This laser provides the laser light for the Zeeman slower (ZS), the transversal cooling (TC), the spectroscopy (SPEC) and the imaging (IMG). Each laser path includes a double-pass acousto-optic modulator (AOM) for individual frequency scans. The laser is locked using modulation transfer spectroscopy at the reference cell. The focal lengths of the lenses f are written above the symbol in the figure.

583 nm setup for the spectroscopy

The 583 nm laser system used for the spectroscopy measurements in the main chamber was constructed based on the previously setups presented in [50] and is shown in Figure 4.2. The light is generated by the Toptica DL pro laser operating at 1166 nm which seeds a Raman fiber amplifier which amplifies this light and doubles the frequency on its output with a single pass crystal to 583 nm with up to 1.5 W. The laser is stabilised to a high finesse ultrastable cavity for long-term stability and independent control over frequency. For this, the Pound-Drever-Hall (PDH) technique is used by employing a fiber-based EOM for the generation of the necessary sidebands. A detailed explanation of the PDH technique can be found in [51]. The fiber-coupled EOM has a large bandwidth which allows for the tunable sidebands over a wide frequency range, leading to a dynamically modifiable laser frequency for the spectroscopy measurements. This replaces other frequency shifting elements

such as double-pass AOM systems. The double-pass AOM used in this setup allows to switch the laser on and off during the experimental sequence.
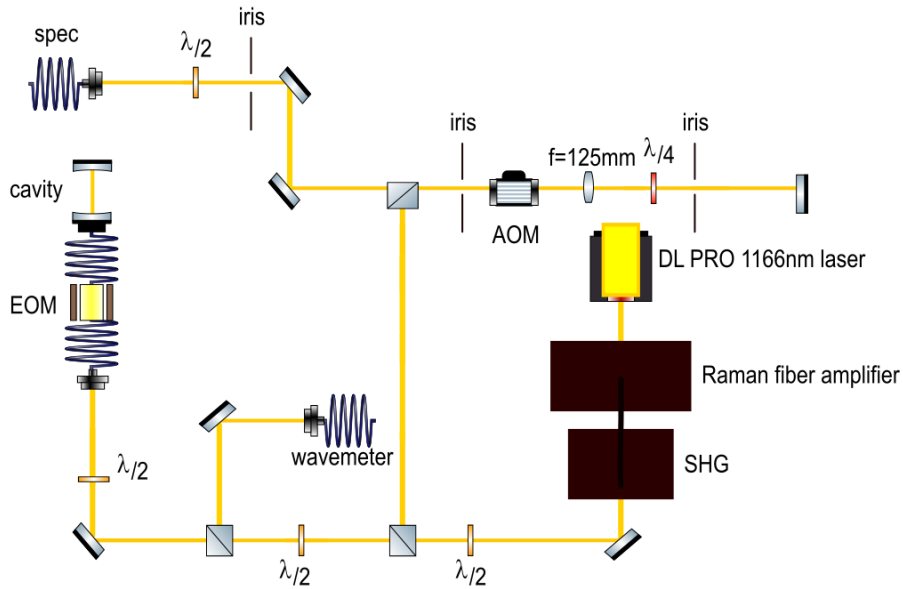

Figure 4.2.: Optical setup of the 583 nm laser used for the measurements in the main chamber. The light is generated by the Toptica DL pro laser operating at 1166 nm with an integrated Raman fiber amplifier and a fiber-coupled SHG unit. The laser is stabilised in frequency via the Pound-Drever-Hall technique and locked to a stable cavity with an EOM coupled fiber. The laser light being coupled into the spectroscopy fiber (spec) is switched on and off using the spectroscopy AOM in double-pass configuration. The focal length of the lens f is written above the symbol in the figure.

4.2. The Vacuum Apparatus

This section provides an overview of the individual units of the TREQS experiment, delving into the technical details of the crucial steps in the generation of an ultracold quantum gas.
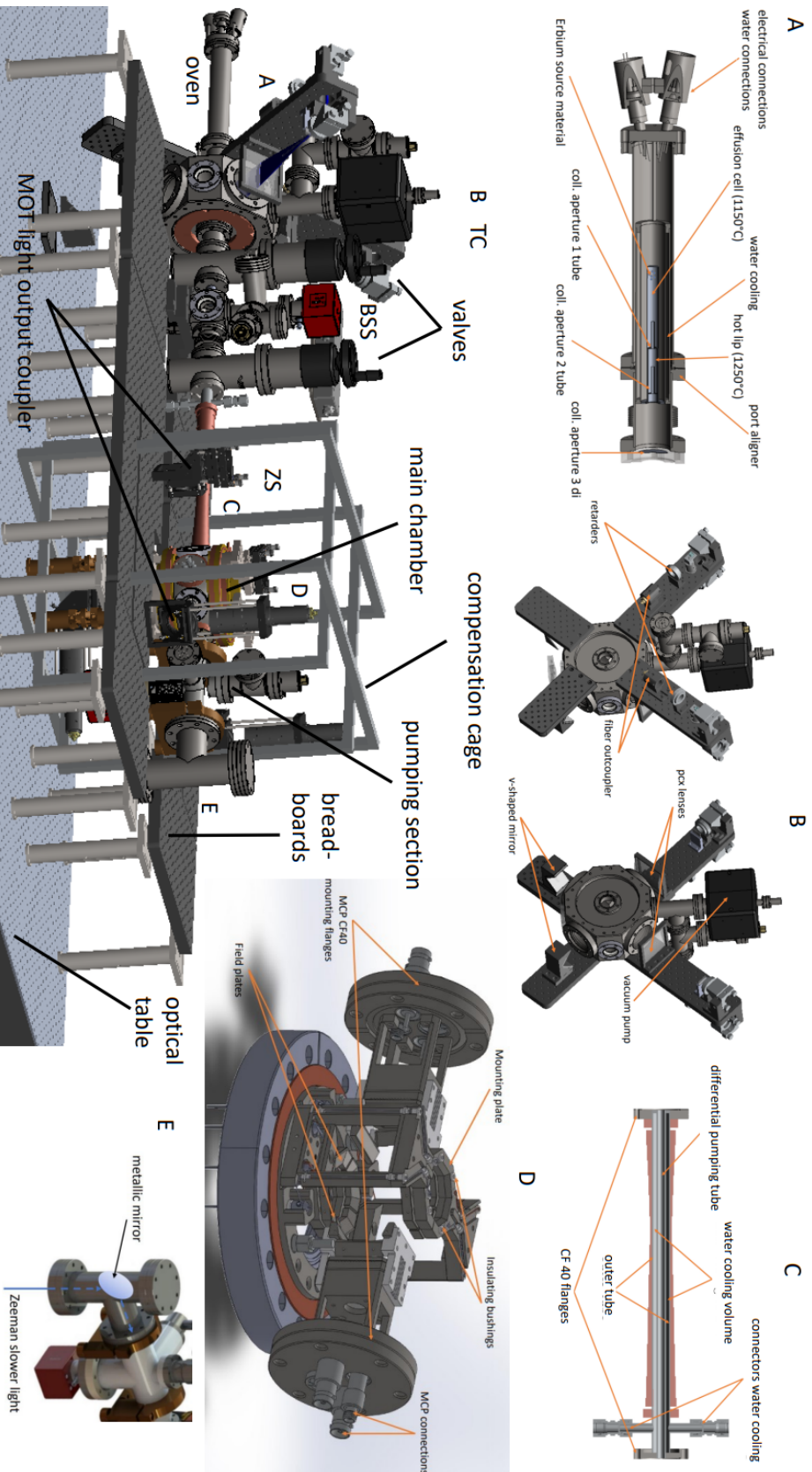
Figure 4.3.: Technical drawing of the entire setup of the TREQS experiment with focus on the most important sections of the experiment: the high temperature oven A, the transversal cooling section B, the Zeeman slower C with light being coupled into the setup in E and the main chamber D. This figure has been created using the technical drawing that has been mostly drawn by Phillip Ilzhöfer and Arno Trautmann.

High Temperature Erbium atomic oven

The thermal atomic gas of erbium atoms is produced by heating the erbium source material with a high temperature oven. The setup of the oven is shown in Figure 4.3 A. The effusion cell made of tantalum contains the erbium source material and is heated up to a temperature of 1150 °C by heating filaments sitting outside the cell. The material tantalum is used because of its high temperature resistivity, its inertness to chemical reactions and its suppression of forming low-melting alloys with erbium [50]. The gaseous erbium atoms leave the effusive cell through the first collimating aperture and reaches the second section, the so-called hot lip. The hot lip has its own heating filaments that heats this section up to a temperature of 1250 °C. At the outside of the heating filaments the water cooling section is placed. After leaving the hot lip and after passing the collimation aperture disc, the erbium leaves the oven. The collimation apertures modify the transversal velocity distribution, as already explained in Section 2.5. In [21], a detailed analysis of the effect of the collimation apertures on the transversal velocity distribution can be found.

Atomic Beam Collimation

After leaving the oven, the transversal velocity distribution of the erbium atomic beam is manipulated in the so-called transversal cooling chamber by implementing laser cooling via an optical molasses extended to two dimensions. This chamber consists of an octagonal shaped vacuum chamber with optical access for two counter propagating laser beams operating at 401 nm passing the chamber through CF63 viewports and four additional CF40 viewports that provide additional optical access. Figure 4.3 B shows the setup of the transversal cooling section. The light for the transversal cooling lasers can be adjusted in polarisation by retarder plates located after the fibers. Before the lasers are directed into the chamber through the viewports, a telescope with cylindrical lenses elongates the laser beam to an aspect ration of about 5:1 to maximise photon scattering by simultaneously having high intensity, as well as a long interaction time with the atomic beam [11]. The laser beam directed into the chamber passes the opposite CF63 viewport and is reflected back by a v-shaped mirror to form the optical molasses. The top flange of the chamber is connected to a 20 L/s ion pump for individual pressure control and an all-metal angled valve allowing to connect external pumping stations. In this section the pump allows to maintain a vacuum pressure of around 10×10^{-10} mbar [50]. The two-dimensional optical molasses is anticipated to provide collimation of the atomic beam by reducing the transversal motional spread, as detailed in Section 3.2. This collimation is expected to result in a greater number of atoms exiting the TC chamber through a narrow aperture, as well as leaving the beam shutter section, as illustrated in Figure 4.3. Both apertures impose a geometric confinement that exhibits velocity selectivity, as atoms with a higher transverse velocity component

move further away from the geometric center.

Beam Shutter Section

The transversal cooling chamber is directly connected by a tube of 50 mm length and inner diameter of 8 mm acting as an aperture to the beam shutter section (BSS) as shown in Figure 4.3. This section of the experiment contains a servo motor-controlled shutter that is used to block the erbium atomic beam after the MOT loading sequence. Furthermore, at the top port of this section a non-evaporative getter and an ion pump provide differential pumping in order to achieve a vacuum pressure of around 10×10^{-11} mbar. On the opposite site the inner tube of the Zeeman slower acts also as an aperture [50]. This pumping section contains an ionisation gauge, as well as an additional all-metal angled valve to connect external pumping stations. In front and after the BSS two gate valves allow to separate the individual sections of the vacuum apparatus.

Zeeman Slower

The Zeeman slower in the TREQS experiment used to decelerate the erbium atomic beam in longitudinal direction has been calculated and theoretically optimised by Benedict Hochreiter in the frame of his master thesis. The setup of the Zeeman slower is shown in Figure 4.3 C. The technical details are taken from [49] if not stated otherwise .

The Zeeman slower has been designed for a capture velocity of 370 m/s and to decelerate the atoms to a final velocity of 5 m/s, which corresponds to a value slightly smaller than the capture velocity of the MOT of 5.6 m/s. The light for the Zeeman slower is provided by the diode laser system presented in Section 4.1. The laser beam is directed into the Zeeman slower vacuum tube through the bottom viewport of the vacuum tube located after the pumping section of the experiment as shown in Figure 4.3 E. This tubes contain an in-vacuum aluminium mirror that is tilted in order to reflect the light into the Zeeman slower.

The magnetic field of the Zeeman slower is divided into 12 magnetic field segments being produced by nine coils. The designed currents of the nine coils of the Zeeman slower producing the individual magnetic fields shown in Figure 4.4 are given in Table 4.1.

Table 4.1.: Designed currents for the magnetic field coils of the Zeeman slower

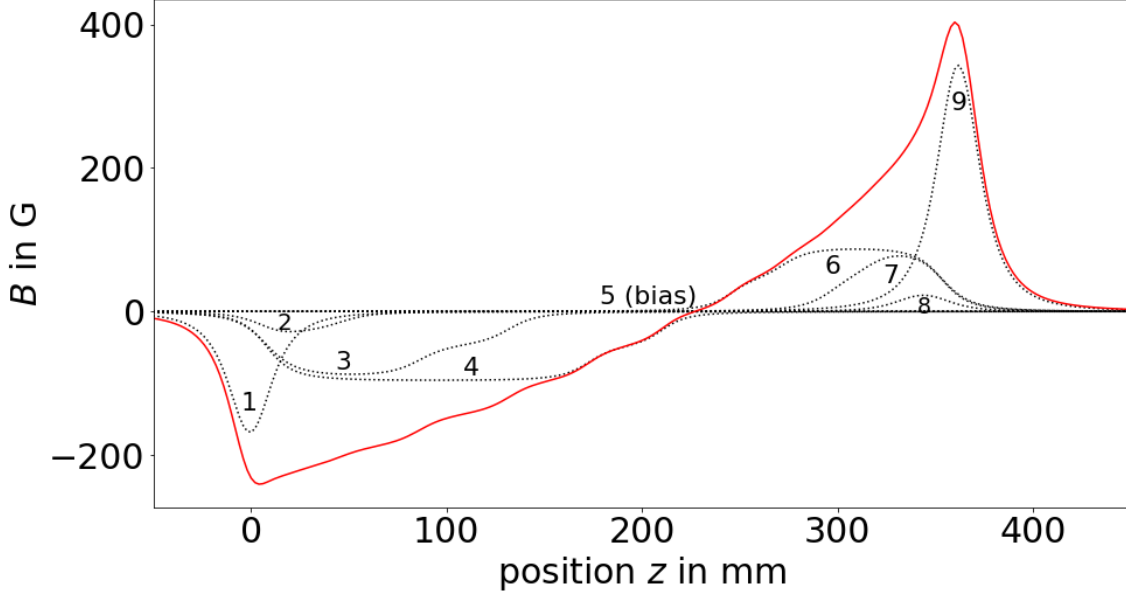| number	coil 1	coil 2	coil 3	coil 4	coil 5	coil 6	coil 7	coil 8	coil 9
current	10.5 A	6.5 A	10 A	10.4 A	0 A	9.8 A	10.4 A	10.4 A	23 A

Figure 4.4.: Magnetic fields of the individual coils (black dotted line) obtained theoretically for the Zeeman slower used in the TREQS experiment, calculated from the coil design and for the designed currents given in [49] and total magnetic field (red solid line). The corresponding coil numbers are written next to the corresponding magnetic field. The magnetic field of coil number 5 is zero over the entire length of the Zeeman slower.

An explanation of the current control for the coils can be found in the Appendix A.1. The wire used for the coils has a rectangular shape with dimensions $1\,\text{mm} \times 2.6\,\text{mm}$ and has been fixed in place with a special glue "Duralco® NM25 Adhesive epoxy" due to its amagnetic nature, its thermal conductivity of $1.87\,\text{W/mK}$ and electrical resistivity of $10 \times 10^{15}\,\Omega\,\text{cm}$. Furthermore, this glue is able to resist temperatures up to $260\,°\text{C}$, which is necessary to withstand the baking process of the experiment. In addition to the nine Zeeman slower coils there are two compensation coils being wound separately in order to prevent the magnetic field of the Zeeman slower to disturb the sections of the experiment being located before and after the Zeeman slower. The coil assembly has a total length of $373\,\text{mm}$.

The entire outer vacuum tube has a length of $435\,\text{mm}$, an outer diameter of $23\,\text{mm}$ and is made of stainless steel type 1.4404. Inside this tube the differential pumping

tube is located that the atoms need to pass, consisting of the same type of steel as the outer tube. The inner tube has an outer diameter of 12 mm and an inner diameter of 8 mm. The volume between the inner and the outer tube is used for the water cooling in order to dissipate the heat produced by the coils. The connectors of the water cooling are also made from the same type of steel. At both ends of the Zeeman slower there is a CF40 flange with an aperture for the optical access of the Zeeman slower light. The distance between the center of the MOT and the last coil of the Zeeman slower is 101 mm.

After this laser cooling stage, the atoms reach the main chamber that constitutes the core element of the experimental setup.

Main Chamber

The main chamber is formed as an octagon, having eight CF40 flanges, one at each side and two CF100 flanges, one at the top and one at the bottom of the chamber providing the optical access for the three-dimensional optical molasses. Inside this chamber, the MOT, roughly introduced in Section 3.2, is implemented. The coils providing the magnetic field for the MOT are mounted on the top and the bottom of the chamber. Inside this octagonal vacuum chamber, an electric field control system is mounted. Figure 4.3 D shows the electric field control system used to compensate disturbing external electric stray fields, to apply precisely controlled electric fields during the experiment and for the field ionisation of the excited Rydberg atoms. The electric field is provided by eight cloverleaf-octupole field plates mounted on the shown mounting plates. Furthermore, the control system possesses two microchannel plate detectors (MCP) units used for the detection of ions or electrons [50].

At the other side of the main chamber, another pumping system similar to the one above the BSS is located. The main chamber is surrounded by rectangular magnetic field coils used to compensate external magnetic fields such as the earth geomagnetic field that would disturb the measurements. This compensation cage has been built within the frame of this thesis. The entire experiment is mounted on an optical table that is air-floated in order to protect the experiment from environmental vibrations.

5. Experimental Measurement Techniques

This chapter provides a comprehensive explanation of the theoretical foundation underlying the spectroscopic measurements conducted to characterise the cooling and deceleration techniques employed in the TREQS experiment. It delves into the expected lineshapes and the broadening mechanisms they originate from. Additionally, the chapter introduces measurement techniques, namely, differential spectroscopy and fluorescence imaging, along with the corresponding setups that have been utilised.

5.1. Lineshape and Broadening Mechanisms

From the discussion in the previous chapter, we know already that light only interacts with atoms within a certain velocity class (see Equation (3.7)) and that the spectral width of the interaction depends on the intensity of the probing light with respect to the saturation intensity (see Equation (3.9)). From a theoretical perspective, the photons of a spectroscopy laser are absorbed in case the laser is on resonance with the atoms. For a moving atom, the resonance condition contains the so-called Doppler shift. If this condition is fulfilled the atom makes a transition to the excited state and can decay via spontaneous emission to the ground state, re-emitting a photon in a random direction.

Now, let us assume the laser interacts with an ensemble of atoms that doesn't have any motional spread and let us assume the photons coming from the laser are continuously measured. In case of a frequency scan of the spectroscopy laser around resonance ν_0 interacting with atoms, the spectroscopy signal would reproduce the Lorentzian shaped interaction probability, characterised by the excitation rate γ_{ex} from Equation (3.5). For the spectroscopic signal that is not containing the spontaneously re-emitted photons, the transmitted intensity I_{nat} as a function of frequency ν around resonance ν_0 is well-described by

$$I_{\mathrm{nat}}(\nu) = I_0 \frac{(\gamma/4\pi)^2}{(\nu - \nu_0)^2 + (\gamma/4\pi)^2}. \tag{5.1}$$

Here I_0 denotes the peak intensity. In case of high intensities of the spectroscopy beam the spectrum is expected to be broadened up due to an effect known as

saturation broadening leading to a new FWHM of $\Delta\nu_{\mathrm{S}}^{\mathrm{FWHM}} = \Delta\nu_{\mathrm{nat}}^{\mathrm{FWHM}}\sqrt{1 + S_0}$. Here S_0 denotes the saturation parameter. However, as the erbium atomic beam which is subject of the spectroscopic measurements has a motional spread, changing the detuning of the spectroscopy beam $\delta_{\mathrm{spec}} = \nu - \nu_0$ can resolve the velocity distribution of the atomic beam along the $\vec{k}$-vector of the spectroscopy laser beam. For each detuning δ_{spec}, the resonance condition is fulfilled for a different Doppler shift and thus for a different velocity class. In case of the spectroscopy beam being aligned perpendicularly to the erbium atomic beam, the transmitted intensity $I_{\mathrm{D}}(\nu)$ resolves the measured transversal motional spread described by the one-dimensional Maxwell-Boltzmann distribution from Equation (2.5) and can be written as

$$I_{\mathrm{D}}(\nu) = I_0 \exp\left(-\frac{c^2 m(\nu - \nu_0)^2}{2k_{\mathrm{B}}T\nu_0^2}\right). \tag{5.2}$$

Here c denotes the speed of light. The FWHM of the Doppler broadened spectrum is given by $\Delta\nu_{\mathrm{D}}^{\mathrm{FWHM}} = 2\sqrt{2\ln 2}\sqrt{k_{\mathrm{B}}T\nu_0^2/(mc^2)}$. The form of Equation (5.2) can easily be derived from Equation (2.5) by substituting the velocity v with $v = c(\nu/\nu_0 - 1)$, as explained in [21].

However, in practice, the measured line will be a convolution of both shapes: Due to the natural broadening, the spectroscopy signal can show Lorentzian character in case the natural linewidth is on the order of magnitude of the motional spread in frequency space.

To get an idea which broadening mechanism actually determines the spectral shape, it is common to compare it to a Gaussian function, as described by Equation (5.2), a Lorentzian as described by Equation (5.1), as well as to a so-called Voigt profile which is according to [21] defined as convolution of the individual shapes of the form

$$I(\nu, \Delta\nu_{\mathrm{G}}, \Delta\nu_{\mathrm{L}}) = \int_{-\infty}^{+\infty} \mathrm{G}(\nu', \Delta\nu_{\mathrm{G}})\mathrm{L}(\nu - \nu', \Delta\nu_{\mathrm{L}})\mathrm{d}\nu'. \tag{5.3}$$

Here $\mathrm{G}(\nu', \Delta\nu_{\mathrm{G}})$ denotes the Gaussian contribution with $\Delta\nu_{\mathrm{G}} = \Delta\nu_{\mathrm{D}}^{\mathrm{FWHM}}$, whereas $\mathrm{L}(\nu - \nu', \Delta\nu_{\mathrm{L}})$ denotes the Lorentzian contribution with $\Delta\nu_{\mathrm{L}} = \Delta\nu_{\mathrm{S}}^{\mathrm{FWHM}}$ in case of saturation broadening and $\Delta\nu_{\mathrm{L}} = \Delta\nu_{\mathrm{nat}}^{\mathrm{FWHM}}$ in the low intensity limit. The resulting total linewidth of the Voigt profile $\Delta\nu_{\mathrm{V}}^{\mathrm{FWHM}}$ can according to [52] be approximated as

$$\Delta\nu_{\mathrm{V}}^{\mathrm{FWHM}} \approx 0.5346\Delta\nu_{\mathrm{L}} + \sqrt{0.2166\Delta\nu_{\mathrm{L}}^2 + \Delta\nu_{\mathrm{G}}^2}. \tag{5.4}$$

There are also other broadening mechanisms such as collisional broadening influencing the shape of the spectrum, but as explained in [21], this effect can be neglected in the effusive regime.

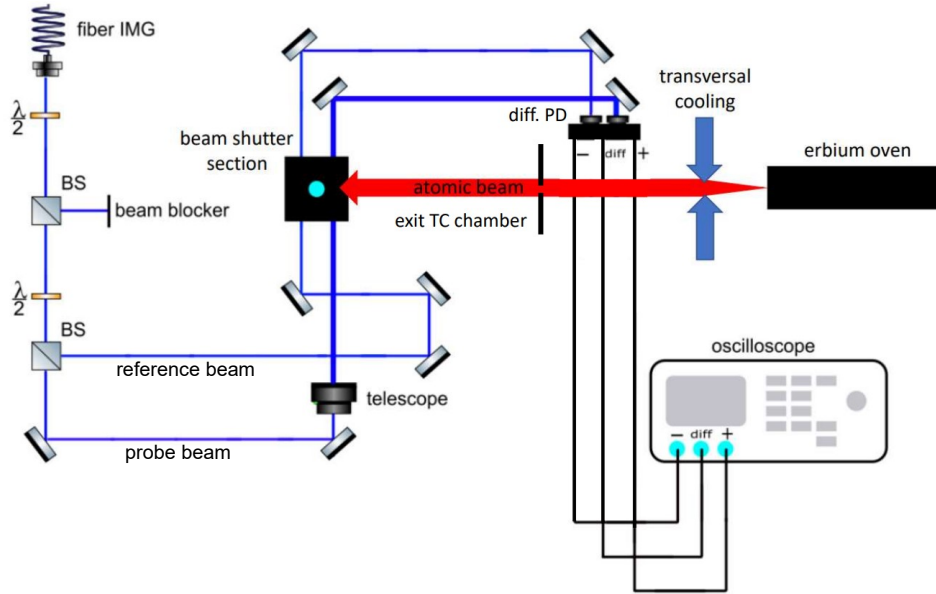# 5.2. Differential Absorption Spectroscopy: Measurement Procedure

Figure 5.1.: Setup for the differential absorption spectroscopic measurement taken in the beam shutter section. The laser beam is split into two paths, the reference beam and the probe beam. Only the probe beam can interact with the atoms. Both beams are directed into a differential photo diode which subtracts the reference beam from the probe beam. All three signals (reference, probe and differential) are imaged on the oscilloscope. The first $\lambda/2$ retarder plate in combination with the first polarisation beam splitter (BS) is used to clean the polarisation. An additional telescope is used to enlarge the reference beam passing the atoms.

For the characterisation of the transversal cooling mechanism, we use differential absorption spectroscopy. These measurements have been performed in the beam shutter section providing optical access via two viewports for the 401 nm laser using the setup shown in Figure 5.1. The spectroscopy laser (probe beam) is intersected perpendicularly with the atomic beam. To measure the absorption spectra, the laser is directed into a photodiode. As explained in the previous section, the absorption spectrum can be measured by scanning the laser in frequency, providing informations on the transversal motional spread. The randomly re-emitted photons resulting from the interaction are not coupled into the photodiode leading to a signal loss. Furthermore, the exit of the TC chamber acts as an aperture which is limiting the spatial divergence of the atomic beam. This allows to estimate the collimation performance of the TC.

In addition, a polarisation beam splitter in combination with a retarder plate

provides the reference beam which is needed to remove the background from the signal. The resulting differential signal is free from global intensity fluctuations of the laser, but is sensitive to changes of the intensity of the probe beam.

5.3. Fluorescence Imaging: Measurement Procedure

For further optimisations of the transversal cooling mechanism, but also to characterise the Zeeman slower, we directly measured the randomly re-emitted photons (fluorescence) with a CCD camera. These measurements have been taken in the main chamber using the 583 nm laser, because the narrow line transition at 583 nm provides a better velocity resolution of 0.1 m/s, as explained in [11]. The setup for the measurement is shown in Figure 5.2 a).
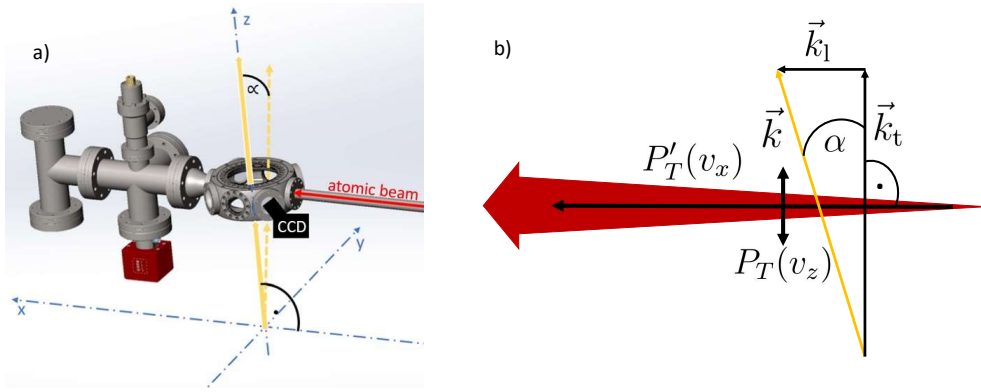

Figure 5.2.: Scheme of the measurement setup used in the main chamber. In a): The coordinate system we refer to is indicated as blue lines. The 583 nm spectroscopy laser that can be scanned in the $x-z-$plane of this coordinate system is indicated by an yellow arrow. The dashed yellow arrow shows the laser declined by an angle of α. The erbium atomic beam passing the center of the Zeeman slower vacuum tube is indicated by a red arrow. A CCD camera is imaging the fluorescence signal resulting from the interaction of the spectroscopy laser with the erbium atomic beam. In b): The transversal motional spread $P_T(v_z)$ and the longitudinal motional spread $P'_T(v_x)$ are indicated by black arrows. For the spectroscopy performed under an angle, the $\vec{k}-$vector can be decomposed into a component parallel to the direction of motion of the atomic beam $\vec{k}_l$, as well as a component transversal to the direction of motion $\vec{k}_t$.

The spectroscopy laser is directed into the main chamber through the bottom viewport. The fluorescence is imaged by a CCD camera through one of the side viewports. Analogous to the differential absorption spectroscopy, the imaged fluorescence signal for the perpendicular intersection allows to estimate the transversal motional spread. As an extension to the previous measurement performed in the BSS, the alignment of the spectroscopy beam under some angle allows to gain information on the longitudinal motional spread. The fluorescence resulting from the

interaction of the spectroscopy laser with the atoms allows to estimate the motional spread along its direction of propagation $\vec{k}$ due to the velocity dependence of the resonance condition. For the used narrow line spectroscopy laser, the measured spectrum $P_T(v_z)$ in case of fully transversal alignment to the atomic beam is expected to be almost of purely Gaussian nature. In case the laser would be aligned parallel to the atomic beam, the longitudinal motional spread $P_T'(v_x)$ can be resolved. However, as the longitudinal motional spread has a width of several hundred of m/s as estimated in Section 2.5, large-range tunable lasers would be required. To avoid such large scan ranges it is common to perform the spectroscopy under an angle to have a component of the $\vec{k}-$vector parallel to the direction of motion of the atomic beam $\vec{k}_\mathrm{l}$, as well as a component transversal to the direction of motion $\vec{k}_\mathrm{t}$. A schematic of the decomposition of the $\vec{k}-$vector is shown in Figure 5.2 b).

For the analysis of the images taken by the CCD camera, a region of interest (ROI) containing the fluorescence signal, as well as an offset region are introduced. An example on how these regions have been set in this experiment is shown in Figure 5.3. To derive the final signal we first subtract a global offset value from each pixel, determined by the mean pixel value of the offset region. Then we numerically integrate the fluorescence signal ROI pixel values to get a single value corresponding to the fluorescence strength.
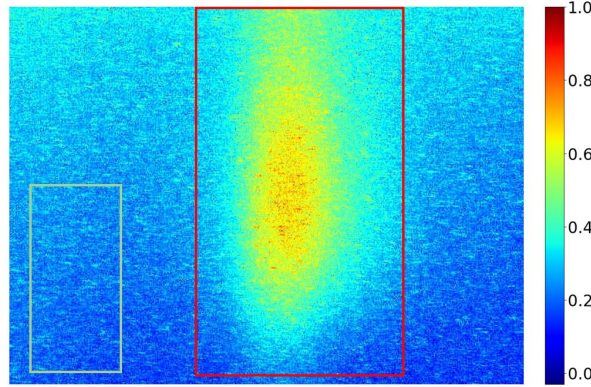

Figure 5.3.: Definition region of interest and offset region for the analysis of the fluorescence imaging. The red rectangle in this figure indicates the region of interest, encircling the fluorescence signal. The green rectangle in this figure indicates the offset region containing the background noise. The signal strength is indicated as a colour gradient in this figure. This image has been normalised for a better visualisation.

6. Transversal Cooling of an Erbium Atomic Beam

In this chapter, the results of the measurements regarding the optimisation and characterisation of the transversal cooling mechanism are presented, containing both, the results from the differential absorption spectroscopy, as well as the results from the fluorescence imaging.

6.1. Optimisation via Differential Absorption Spectroscopy at 401 nm

For the differential absorption spectroscopic measurements, the laser is scanned in frequency for different detunings of the transversal cooling laser beams. During each experimental run, the signal is recorded with the transversal cooling beams being on (TC on) and with the transversal cooling beams being off (TC off), respectively. A few examples of the differential signal measured in the BSS are shown in Figure 6.1.
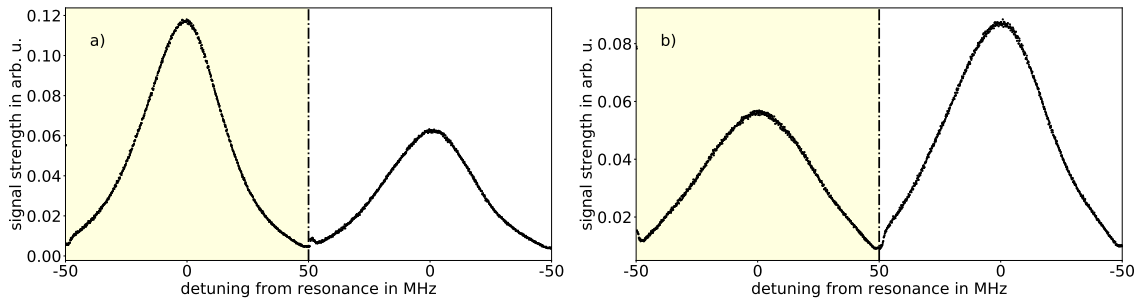

Figure 6.1.: Example of the recorded differential spectroscopy signal. The frequency of the spectroscopy light is scanned upwards around resonance in a range of 100 MHz with the transversal cooling light being on (yellow coloured background). Then the transversal cooling light is switched off and the spectroscopy laser is scanned downwards around resonance again (white background). In a) the detuning of the TC cooling light was set to $\delta = -20$ MHz, in b) it was set to $\delta = 20$ MHz.

As shown in Figure 6.1 a) for a detuning of the TC from resonance of -20 MHz, the transversal cooling effect clearly leads to an increase in signal strength and thus to a larger number of atoms that are collimated sufficiently in order to reach the

BSS. In Figure 6.1 b) the effect of transversal heating can be observed clearly. As explained, this effect broadens the transversal motional spread and therefore the signal is reduced as less atoms reach the BSS due to aperture before. Further, to understand which broadening mechanism dominates the recorded signal, the differential spectroscopy signals have been fitted with a Gaussian representing the Doppler broadening mechanism from Equation (5.2), with a Lorentzian accounting for natural as well as saturation broadening from Equation (5.1), as well as with the convolution from Equation (5.3) accounting for all contributions. An example of a fitted data set taken with TC on for a detuning of -20 MHz is shown in Figure 6.2.
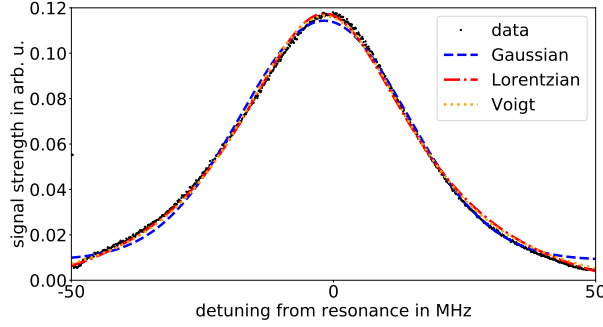

Figure 6.2.: Dominating broadening mechanism analysis for transversal motional spread measurement. The black data points correspond to the TC on case data for a detuning of the TC chosen as -20 MHz. The blue dashed line represents a Gaussian fit of the form (5.2), the red dash-dotted line represents a Lorentzian fit of the form (5.1) and the orange dotted line represents a fit of the form (5.3).

As shown, the Gaussian fit deviates significantly from the presented data set. From the fit parameters the FWHM can be calculated to $\Delta\nu_{\mathrm{G}}^{\mathrm{FWHM}} = 37.4(2)$ MHz being slightly larger than the natural linewidth of the transition $\Delta\nu_{\mathrm{nat}} = 29.7$ MHz. In comparison, the Lorentzian fit reproduces the given data set almost perfectly. The FWHM of the Lorentzian has been calculated to $\Delta\nu_{\mathrm{L}}^{\mathrm{FWHM}} = 42.7(3)$ MHz, which is larger than the FWHM resulting from the Gaussian fit and also significantly larger than the natural linewidth of the transition. As already discussed before, we expect a convolution of both profile types. Therefore, the measured spectrum is fitted with a Voigt profile. The FWHM of the Gaussian contribution to the Voigt profile can be calculated as $\Delta\nu_{\mathrm{G}} = 16(2)$ MHz and the FWHM of the Lorentzian contribution as $\Delta\nu_{\mathrm{L}}^{\mathrm{FWHM}} = 34(2)$ MHz. Using Equation (5.4), the total linewidth of the Voigt profile can be approximated as $\Delta\nu_{\mathrm{V}} = 41(2)$ MHz. The FWHM of the Lorentzian contribution to the Voigt profile $\Delta\nu_{\mathrm{L}}^{\mathrm{FWHM}}$ is comparable to the natural linewidth of the 401 nm transition of about 30 MHz, leading to the conclusion that almost the entire Lorentzian contribution is dominated by the natural broadening. The Doppler broadening can be extracted from the Gaussian contribution, leading to a temperature of $T = 0.08(2)$ K. Comparing this temper-

ature to the expected temperature of $T = 1.5\,\mathrm{mK}$ obtained in an optical molasses as explained in Section 3.2, shows that the motional spread is larger than expected from theory. One possible reason is that the interaction length of the atomic beam with the TC light is too short to reach the theoretical equilibrium result. In addition, it could be that the effective intensity of the TC light is lower than expected due to the interplay of polarisation and residual magnetic fields, making the TC cooling less efficient.

Now, we want to measure the performance of the TC as a function of the detuning from resonance. For this, we repeat the measurement for detunings in the range $[-80, +60]\,\mathrm{MHz}$ and take the amplitude of the signal from the Voigt fit as a measure. More precisely, we take the ratio of this maximum signal strength between the TC on and the TC off case $A_{\mathrm{TC,on}}/A_{\mathrm{TC,off}}$. Figure 6.3 shows the resulting dependence.
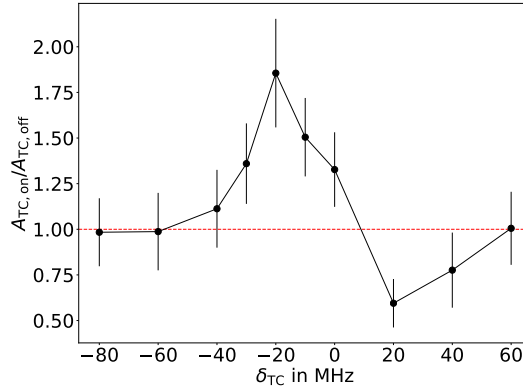

Figure 6.3.: Relative maximum signal strength $A_{\mathrm{TC,on}}/A_{\mathrm{TC,off}}$ as a function of the detuning of the transversal cooling lasers δ_{TC}. The red dashed line indicates a relative maximum signal strength of 1. In addition to the combined standard error given by the fits, we account for fluctuations/drifts during the whole measurement. Thus, the presented error bar includes the error given by the fluctuations of the TC off signal averaged over the entire detuning range of $\sigma_{\mathrm{err}} = 0.00771$.

For a too large detuning from resonance (further from resonance than $\pm 60\,\mathrm{MHz}$), the transversal cooling laser light is almost non-interacting with the erbium atoms leading to $A_{\mathrm{TC,on}}/A_{\mathrm{TC,off}} \approx 1$. This value of the detuning corresponds to approximately twice the natural linewidth of the transition. For a detuning of around $-40\,\mathrm{MHz}$, the effect of transversal cooling can already be observed, as there are more atoms reaching the beam shutter section leading, to an increase in amplitude of the differential spectroscopy signal. The highest amplitude ratio can be observed for a detuning of $-20\,\mathrm{MHz}$. This means for the given geometry, the collimation performance is maximal for a detuning of $-20\,\mathrm{MHz}$. This result can be compared to estimations from theory regarding the damping coefficient, stating an expected maximum efficiency for a detuning between $-1/3\Delta\nu_{\mathrm{nat}}$ ($-10\,\mathrm{MHz}$) and $-1/2\Delta\nu_{\mathrm{nat}}$

$(-15\,\mathrm{MHz})$ for values of $S_0 = 2$. The obtained result is slightly larger than the expected ideal value for efficient damping. Furthermore, crossing the resonance and going to positive detunings we observe transversal heating. As explained previously, the atoms instead of being collimated and cooled, are accelerated leading to a loss of atoms in the BSS.

Now, as already mentioned, it is possible to separate the Gaussian contribution from the Lorentzian contribution using a Voigt fit, which in principle can be used to estimate the narrowing (or broadening in case of transversal heating) of the motional spread resulting from the action of the TC laser beams on the atomic beam. Thus, we analyse the relative FWHM of the Gaussian contribution to the Voigt fit $\Delta\nu_{\mathrm{G,TCon}}^{\mathrm{FWHM}}/\Delta\nu_{\mathrm{G,TCoff}}^{\mathrm{FWHM}}$ for detunings in the range $[-80, +60]\,\mathrm{MHz}$. Figure 6.4 shows the resulting dependence.
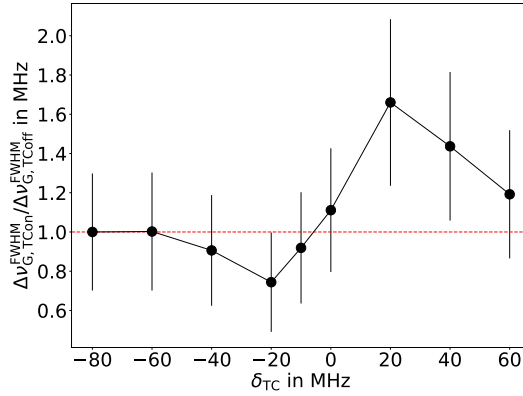

Figure 6.4.: Relative FWHM of the Gaussian contribution to the Voigt fit $\Delta\nu_{\mathrm{G,TCoff}}^{\mathrm{FWHM}}$ as a function of the detuning of the transversal cooling lasers δ_{TC}. The red dashed line indicates a relative FWHM of 1. In addition to the combined standard error given by the fits, we account for fluctuations/drifts during the whole measurement. Thus, the presented error bar includes the error given by the fluctuations of the TC off signal averaged over the entire detuning range of $\sigma_{\mathrm{err}} = 1.74\,\mathrm{MHz}$.

As shown, for a detuning from resonance further than $\pm 60\,\mathrm{MHz}$ we get $\Delta\nu_{\mathrm{G,TCon}}^{\mathrm{FWHM}}/\Delta\nu_{\mathrm{G,TCoff}}^{\mathrm{FWHM}} \approx 1$. This means that the TC shows no cooling/heating performance which is equal to the result obtained for the maximum strength analysis, see Figure 6.3. In addition, as expected from the results obtained in the previous analysis, the FWHM is minimal at a detuning of $-20\,\mathrm{MHz}$. Furthermore, in case of blue detuning, transversal heating can be observed in form of an increase in FWHM. Both results, the results from the maximum signal strength and the results from the FWHM of the Gaussian contribution to the Voigt fit, are consistent with each other. From this we can conclude that the best collimation performance is obtained at a detuning of $-20\,\mathrm{MHz}$ and that transversal heating can be observed at a detuning of $+20\,\mathrm{MHz}$ in this section of the experiment (BSS).

For the completeness of the analysis, also the Lorentzian contribution to the Voigt profile has been analysed, which is expected to be constant for all measurements (TC on and TC off) as it is characterised by the natural or saturation broadening. Both broadening mechanisms are quantified by the transition parameters and the laser intensity which were kept constant for all measurements. The obtained values did slightly fluctuate around a mean value of 32.5 MHz with a standard deviation of $\sigma_{err} = 1.6$ MHz, which is comparable to the natural linewidth of the transition.

Measurement Difficulties

During the measurements the differential signal recorded at the oscilloscope did strongly fluctuate under the influence of mechanical stress as well as under slight changes of the angle between probe beam and atomic beam. As a first guess, it was assumed that these fluctuations do arise due to cavity-like effects of the light passing the two viewports of the beam shutter section. However, to reduce this sensitivity, the polarisation of the light has been changed to circular which reduces the probability of creation of standing waves between the two viewports. Furthermore, the probe beam has been enlarged by using a telescope. Both, changing the polarisation and making the probe beam larger, did not help to reduce the sensitivity to environmental disturbances. The signal measured in case of TC off should remain equal for all measurements, as the atom flux is only determined by the velocity selective geometry of the experiment. However, as this has not been the case the TC off signal has been recorded for each experimental run.

6.2. Optimisation via Fluorescence Imaging at 583 nm

This section contains an explanation on the determination of the resonance frequency of the laser, as well as on the optimisation and characterisation of the transversal cooling mechanism.

Determination of the resonance frequency

As a first step, we need to find the center frequency of the optical transition to be able to calibrate the frequency of the EOM used for detuning the 583 nm laser source. To do so, the spectroscopy laser should be aligned as good as possible perpendicularly to the erbium atomic beam, as in this case the spectrum should be symmetric around the (unshifted) resonance position. In case the spectroscopy beam is not fully perpendicular to the atomic beam, the signal will show an asymmetric character from the longitudinal motional spread with a shifted maximum corresponding to the most probable velocity. The alignment is done by looking at

the back reflection of the laser being produced at the bottom CF100 viewport of the main chamber with the incoming laser beam. Figure 6.5 shows the resulting spectra for the perpendicular alignment, as well as for not-perpendicular alignments.
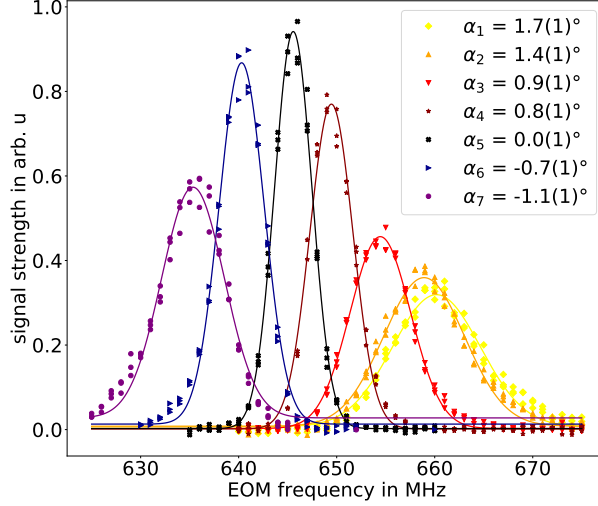

Figure 6.5.: Spectroscopy data taken under different angles. The total fluorescence signal strength is shown as a function of the spectroscopy laser EOM frequency. Each spectroscopy measurement has been repeated three times. Each data set is fitted with a Gaussian function.

The angle is calculated from the distance between the incoming laser beam and the back reflection being generated at the viewport. The range in which the angle can be tuned is limited by the geometry of the main chamber, as the inside of the main chamber contains a complex electric field control system. The spectroscopy laser has to pass through the center area of the electric field plates without hitting any parts of the control system to avoid reflections inside the main chamber that disturb the measurement, e.g. saturating the camera.

As shown in the plot, we indeed observe that for larger angles, the maximum is shifted away from the symmetric Gaussian shaped spectrum at 0°. Furthermore, the amplitude (width) gets smaller (larger) for larger angles as the number of atoms stays constant for different angles, but the atoms are spread over a larger velocity range. To determine the EOM frequency which corresponds to the unshifted resonance, we perform a Gaussian fit to each of the spectra and look at the maximum amplitude of the fit vs. the EOM frequency position of the peak, see Figure 6.6 a). Additionally we can look at the width as a function of the EOM frequency position of the peak, as shown in Figure 6.6 b).
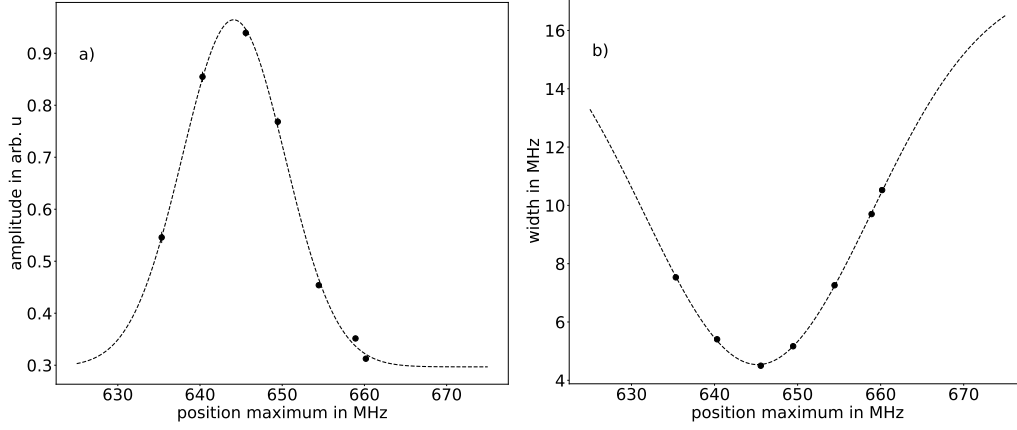
Figure 6.6.: In a) the black data points indicate the amplitude of the Gaussian fit as a function of the maximum position in frequency. In b) the black data points indicate the width of the fits as a function of the maximum position in frequency. The black dashed lines in a) and b) correspond to Gaussian fits.

In both cases, we clearly see a maximum or a minimum at a specific EOM frequency. We can fit now a Gaussian to both datasets and derive a center position of $\nu_{\mathrm{ampl}} = 644.1(1)\,\mathrm{MHz}$ looking at the amplitude data and a center position of $\nu_{\mathrm{width}} = 645.2(1)\,\mathrm{MHz}$ from the width data. Therefore, we take the mean value of both results $\nu_{\mathrm{res}} = 644.6(5)\,\mathrm{MHz}$ for the analysis of the rest of this thesis. The given error corresponds to the standard deviation.

Method for the Alignment of the Transversal Cooling Laser Beams

As explained in Section 3, to achieve cooling, two counter propagating laser beams with red detuning $\delta < 0$ need to interact with the atoms forming an optical molasses. For the alignment of the laser beams it turned out that using an iterative process also using transversal heating conditions is preferential, as the heating process also works in case of a single laser beam propagating in one direction. As elaborated in Section 6.1, efficient transversal heating is obtained in case of blue detuning of the transversal cooling laser beams around $+20\,\mathrm{MHz}$. This knowledge is used now to align the transversal cooling laser beams to the erbium atomic beam. A good alignment in this sense would mean that the action of the laser onto the atoms leads to a maximal reduction in signal strength.

In a first step, all TC laser beams except the one that should be aligned are blocked, and the TC frequency is set to a detuning of $+20\,\mathrm{MHz}$. Then, the signal strength of the fluorescence is recorded and minimised continuously while changing the alignment. In a second step, the back reflection of the aligned beam is added again, and the TC frequency is changed back to transversal cooling conditions.

Then, the back reflected beam is aligned while maximising the recorded signal continuously. This procedure is repeated for each beam until no further improvement can be observed. Figure 6.7 shows the improvement of the transversal cooling performance caused by this alignment procedure in comparison to the result obtained before this alignment: The strength of the 583 nm fluorescence signal is shown as a function of the detuning of the transversal cooling frequency.
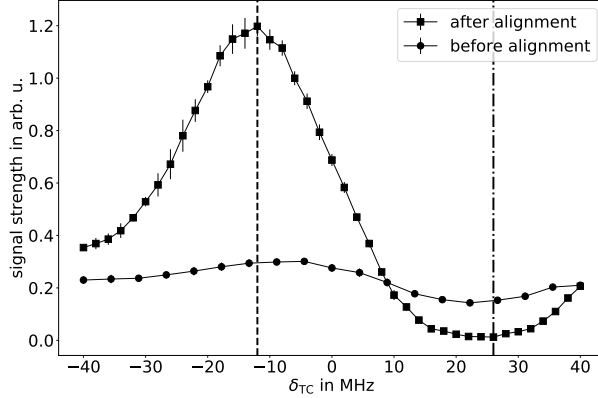

Figure 6.7.: Comparison of cooling performance, before and after the described alignment procedure. The black squares show the strength of the fluorescence signal as a function of the TC AOM frequency detuning after the alignment procedure, the black dots show the results of the same measurement before the alignment procedure. The maximum (minimum) of the curve at a detuning of -12 MHz (26 MHz) is indicated as black dashed (dash-dotted) line.

The fluorescence signal after the alignment is by about a factor of five higher than before. This means that there are a lot more atoms being collimated and that they are able to reach the main chamber. Furthermore, according to this measurement, the transversal cooling works most efficiently for a detuning of -12 MHz. The strongest reduction of the signal strength for the most efficient transversal heating effect is obtained for a detuning of 26 MHz. The reduction of the signal strength obtained by switching the frequency to 26 MHz is almost 100 %. This means, for subsequent measurements instead of blocking the atoms to not let them reach the main chamber with the beam shutter, the atoms can also be blocked using the transversal heating effect. In comparison to the measurement presented in Section 6.1, see Figure 6.3, the most efficient cooling and heating frequencies deviate from the results obtained in this measurement. This is due to different geometrical restrictions in the main chamber in comparison to the beam shutter section. The atoms from the atomic beam encounter more obstacles on the way to the main chamber, which might lead to slight corrections needed to be done on the collimation parameters.

To complete the settings of the transversal cooling, we also looked at the influ-

ence of the polarisation of the TC light, rotating the $\lambda/4$-plate in each of the TC paths, while recording the fluorescence signal for a constant TC detuning of about $-12\,\text{MHz}$. During this optimisation procedure, the strength of the fluorescence signal remained unchanged within the experimental fluctuations. This means that the impact of the polarisation of the light used for the transversal cooling on the cooling performance cannot be observed with this measurement procedure. As explained in [53], the polarisation of the TC light is not important from an atomic-energy perspective, as all energy levels are effectively degenerate at this point. However, as also stated in [53], it is common to use circularly polarised light for the transversal cooling lasers, as this avoids the creation of standing waves that lead to intensity minima of the laser beams within the TC chamber. Such intensity minima could lead to a loss in cooling effectiveness.

Power dependence of the transversal cooling

To conclude the characterisation of the transversal cooling performance, the fluorescence signal is recorded for different values of the TC power. To change the power in the TC beams, the RF power of the AOM of the TC laser system is changed. The result of this measurement is shown in Figure 6.8. At approximately $40\,\text{mW}$ of power per beam, the fluorescence signal intensity approaches the maximum on the curve and starts to exhibit saturation. Beyond this power level, no significant improvement in strength of the fluorescence signal can be observed. This means, the number of atoms being collimated in such a way that they reach the main chamber does not enhance for higher values of the power in the TC laser beams.
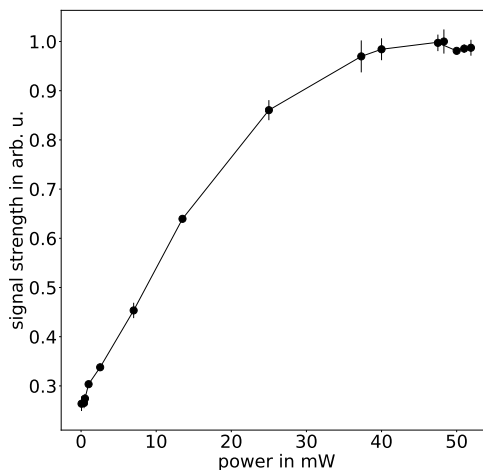

Figure 6.8.: The signal strength as a function of the power of the transversal cooling laser beams is indicated as black dots. The measurement has been repeated three times. The indicated data points correspond to the mean value of the signal strength and the error bars to the standard deviation. The black solid line connects the individual data points.

7. Zeeman slowing of an Erbium Atomic Beam

This chapter provides a comprehensive review of all the important measurements conducted for the characterisation of the Zeeman slower, needed to prepare a trappable ensemble of atoms. The first part of this chapter contains the characterisation of the magnetic field of the Zeeman slower, as well as a simulation of the deceleration performance. The second part of this chapter delves into the characterisation and optimisation of the light needed for the Zeeman slowing process. Finally, the last part of this chapter focusses on the dependence of the slowing performance on the magnetic field.

7.1. Characterisation of the Magnetic Field and Simulation of the Deceleration

For the characterisation of the Zeeman slower, initially the deviations of the experimentally obtained magnetic field from the theoretically designed magnetic field need to be quantified. To ensure that the shape of the magnetic field is sufficiently similar to the desired one calculated by theory, the magnetic field of each coil is measured while running a current of $1\,\mathrm{A}$ through them. Then the measured values are multiplied by the designed current in order to scale the magnetic field up. The measurement has not been done at high currents as the water cooling has not been connected at that time and running high currents would lead to over-heating of the coil assembly.

The theoretical overall shape of the magnetic field in comparison to the measured one is presented in Figure 7.1 a). As shown, the measured magnetic field deviates from the theoretical field in the first part of the Zeeman slower, and also in the last part. Comparing the theoretical field of each coil to the experimentally determined field led to the conclusion, that the magnetic field being produced by coil 1 and coil 9 are to small. To correct this, the current in coil 1 is enhanced from $10.5\,\mathrm{A}$ to $15\,\mathrm{A}$ and the current in coil 9 is enhanced from $23\,\mathrm{A}$ to $25\,\mathrm{A}$. This leads to a new up-scaled experimental overall shape of the magnetic field as shown in Figure 7.1 b), matching the ideal magnetic field better.
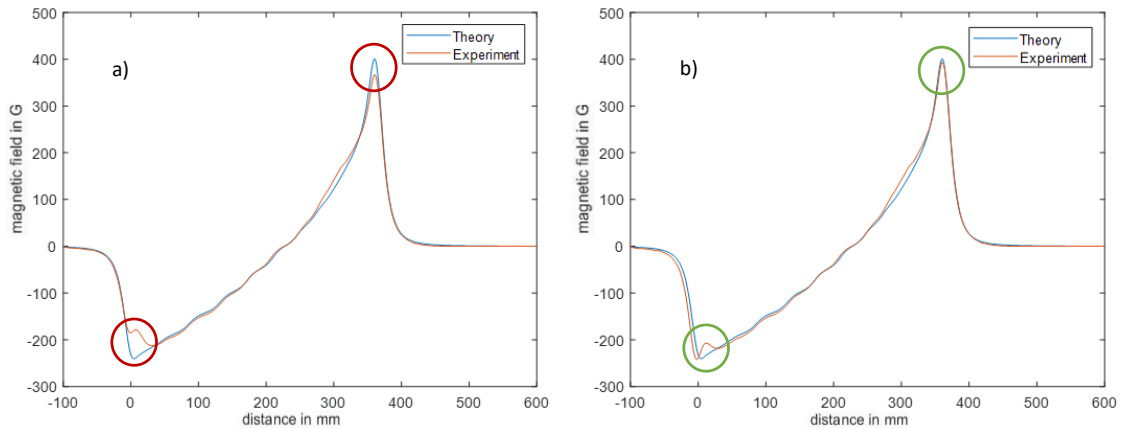
Figure 7.1.: Theoretical overall shape of the magnetic field in comparison to the measured one [54]. In a) the theoretical magnetic field, as well as the measured field is shown. The sections of significant deviations of the actually produced magnetic field from the designed magnetic field are circled in red. In b) the theoretical field in comparison to the corrected one is shown. Here the current in coil 1 is enhanced from 10.5 A to 15 A and the current in coil 9 is enhanced from 23 A to 25 A, leading to reduced deviations circled in green.
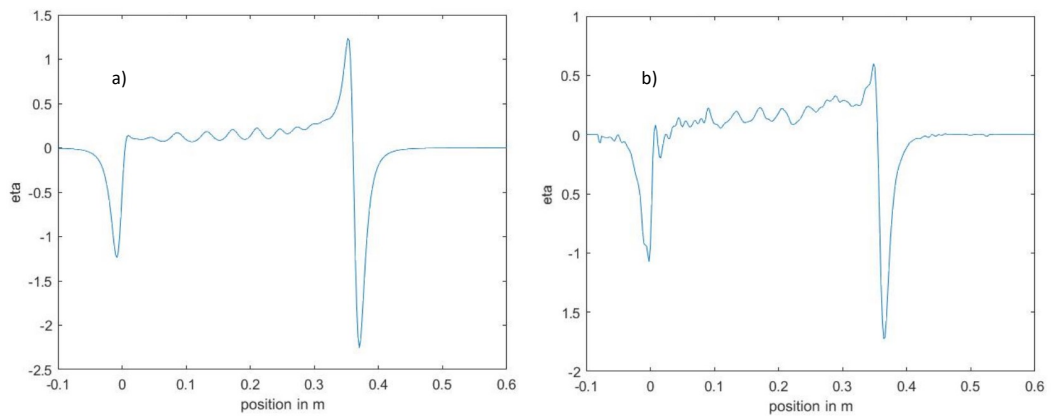
Figure 7.2.: Plot of the η-parameter for the theoretical magnetic field in a) and for the experimentally determined and up-scaled magnetic field with enhanced currents in coil 1 and coil 9 in b) [55]. For both plots, the relevant part is given by the ZS region which ranges from 0 m to 350 m. As shown in both plots, outside this region also negative values of the η-parameter can be obtained. This can be explained due to negative values of the gradient of the magnetic field in the corresponding part of the slower.

Furthermore, as explained in Section 3.5, the measure for how much the produced

magnetic field can deviate from the ideal magnetic field is given by the $\eta-$parameter which has been chosen as $\eta = 2/3$ for this experiment. As shown in Figure 7.2 a), the $\eta-$parameter for the theoretical magnetic field fluctuates between zero and 0.5 along the entire length of the Zeeman slower. For the corrected values of the magnetic fields with enhanced currents in coil 1 and coil 9, the $\eta-$parameter stays below the critical value of 2/3, as shown in Figure 7.2 b).

While the theory only accounts for the slowing of atoms at a length of the Zeeman slower, atoms will also interact in the regions before and after the Zeeman slower with the slowing light. To get a deeper insight on the effect of the unconsidered parts, we implement a classical simulation of the deceleration of the atoms over the whole length of interactions. This is done by numerically integrating the equation of motion taking Equation (3.20) as the position-dependent acceleration into account. This simulation calculates the deceleration of an atom along the Zeeman slower in dependence of the initial velocity and is shown in Figure 7.3 a). The range of the initial velocity is chosen according to the expected velocity distribution of an erbium atomic beam for realistic values of the temperature.
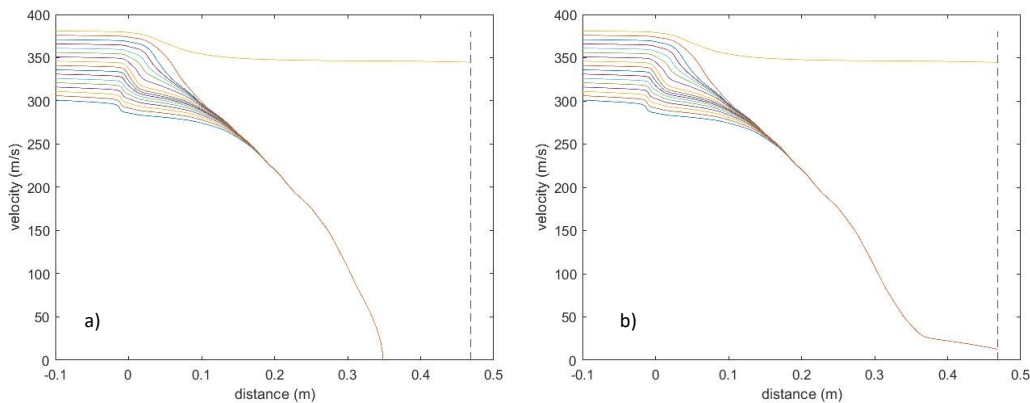

Figure 7.3.: Result of the simulation calculating the deceleration of an atom within the Zeeman slower considering a magnetic field corresponding to the designed currents in a) and for the designed currents for coils 1-8 and a reduced current of 10.73 A in coil 9 in b). The indicated curves correspond to different initial velocities in a range from 300 m/s to 380 m/s. The Zeeman slower coil assembly starts at a position of 0 m in this figure. The end-position is indicated as a purple dashed line [56].

As shown in Figure 7.3 a), for the magnetic field being produced by the designed currents running through the magnetic field coils, the atoms with an initial velocity higher or equal than 380 m/s are not decelerated by the Zeeman slower for the chosen design with a capture velocity of 370 m/s. Atoms with a velocity of 376 m/s are still slightly decelerated, but not to the point where they would stay resonant

with the slowing light, leaving them at high velocities. Atoms with an initial velocity smaller than $375\,\mathrm{m/s}$ are decelerated to zero-velocity, before reaching the desired end-position, indicated as purple dashed line. To correct on this, the current in coil 9 was reduced to $10.73\,\mathrm{A}$ leading to the result shown in Figure 7.3 b). As shown, for the magnetic fields corresponding to the designed currents for coils 1-8 and a reduced current of $10.73\,\mathrm{A}$ in coil 9, the atoms are decelerated to a finite velocity and reach the desired end-position.

7.2. Zeeman Slower Performance Optimisation: Light

This section focusses on the optimisation and characterisation of the light used for Zeeman slowing. The first part of this section presents the studies conducted for the optimisation of the light in frequency, alignment, focussing and polarisation. The second part contains the power characteristics of the Zeeman slower performance.

Zeeman slower light optimisation

In a first step, the light used for the Zeeman slower is optimised in frequency. For this measurement, the Zeeman slower light is overlapped with the erbium atomic beam according to the geometrical alignment that has been performed during the exchange of the oven in the built-up phase of the experiment. This has been done in such a way that the laser beam that is directed into the vacuum part at the end of the pumping section as shown in Figure 4.3 E is passing the center of the collimation aperture 3 disc of the atomic oven as shown in Figure 4.3 A.

Furthermore, for all measurements taken in order to optimise the light of the Zeeman slower, the currents running through the magnetic field coils of the Zeeman slower number 1-8 are set to their designated values from Table 4.1. The current running through coil number 9 is set to a reduced value of $10\,\mathrm{A}$ for this measurements to ensure a slow but finite velocity of the atomic beam as discussed in the previous chapter. To see the effect of the Zeeman slower in form of a reduction in velocity of a fraction of atoms, the spectroscopy beam is declined by an angle α to be sensitive to the longitudinal velocity component of the atomic beam. This means, on a frequency scale, scanning the spectroscopy beam over a Doppler shift range containing the entire velocity distribution, two peaks should appear: one peak corresponding to the thermal atoms that are not influenced by the slower and one peak corresponding to the Zeeman slowed atoms.

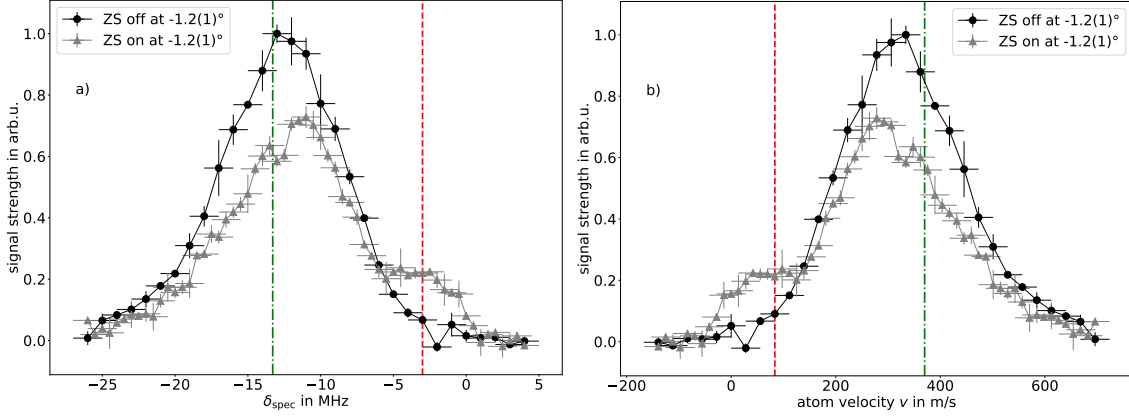The first result of such a scan is shown in Figure 7.4 a).

Figure 7.4.: First results of the spectroscopy measurement under an angle of $\alpha = -1.2(1)°$ for a ZS detuning of $-540\,\text{MHz}$. In this plot, the black dots (grey triangles) represent the total signal strength of the spectroscopy signal in case the ZS is switched off (on). In a) the signal is shown as a function of the detuning of the spectroscopy laser from resonance. The dashed red line marks a detuning of the spectroscopy beam corresponding to -3 MHz. The green dash-dotted line indicates the Doppler-shift $\nu_{\text{D,ZS}} = -13(1)\,\text{MHz}$ corresponding to the capture velocity of the ZS of $v_{\text{D,ZS}} = 370\,\text{m/s}$. . In b) the same dataset as shown in a) is presented in the velocity frame with the transformation from Equation (7.1).

The Doppler-shift corresponding to this velocity can be calculated according to $2\pi\nu_{\text{D}} = kv\sin(\alpha)$ leading to

$$\nu_{\text{D}} = \frac{v\sin(\alpha)}{\lambda}. \tag{7.1}$$

For the later ZS frequency optimisation a detuning of -3 MHz has been chosen for the probe beam, as it corresponds approximately to the center of the appearing peak representing the Zeeman slowed atoms. As shown in Figure 7.4 a), the strength of the fluorescence signal of the Zeeman slowed atomic beam shows a dip slightly below the theoretically designed capture velocity. This dip indicates the start of the Zeeman slower performance. This dip is slightly displaced towards resonance as the real magnetic field in the initial part of the slower is smaller than the theoretically designed magnetic field. Analogously, Equation (7.1) can also be used to calculate the longitudinal velocity component corresponding to the Doppler shifted frequency measured with the spectroscopy laser as $v = \nu_{\text{D}} \cdot \lambda / \sin(\alpha)$. Showing the measurements from Figure 7.4 in this velocity frame results in Figure 7.4 b).

As a next step, to find the optimal detuning of the ZS light, the maximal signal strength of the peak corresponding to the slowed atoms is determined for different ZS detunings δ_{ZS} ranging from $-500\,\text{MHz}$ to $-590\,\text{MHz}$ at a constant detuning of the spectroscopy frequency of -3 MHz. The result of this measurement is shown in Figure 7.5 a). For a ZS detuning of $-564\,\text{MHz}$, the signal strength of the appearing peak corresponding to the Zeeman slowed atoms is maximal. Reproducing

73

the spectroscopy measurement that is shown in Figure 7.4, but changing the ZS detuning to the optimised value of -564 MHz, leads to the result shown in 7.5 b).
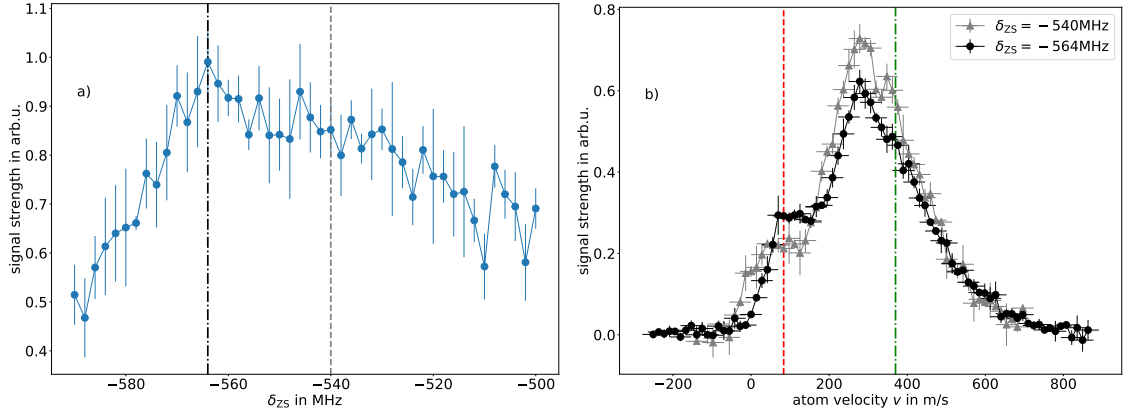

Figure 7.5.: In a) the scan of the detuning for the optimisation process is indicated as blue data points. The previously used detuning of -540 MHz, is indicated as grey dashed line, the ZS detuning leading to the strongest signal of -564 MHz, is indicated as black dash-dotted line. In b) the 583 nm laser spectroscopy signal is shown for a constant detuning of -540 MHz (grey triangles) and for a constant detuning of -564 MHz (black dots). The dashed red line marks a velocity corresponding to a detuning of the spectroscopy beam of -3 MHz, the green dash-dotted line indicates the capture velocity of the ZS.

As shown, the peak corresponding to the Zeeman slowed atoms increased by about factor 1.5 in signal strength for a ZS detuning of -564 MHz, compared to the signal strength for a detuning of -540 MHz. This means, this optimisation procedure in frequency of the Zeeman slower light led to a higher number of atoms that are slowed down. Furthermore, near the designed capture velocity of the Zeeman slower, the two spectroscopy signals start to deviate. The dip indicating the start of the Zeeman slower performance is shifted to higher velocities for a detuning of -564 MHz in comparison to a detuning chosen as -540 MHz.

As a next step, the Zeeman slower light is optimised in alignment, focussing and polarisation. To do so, again spectroscopy data is taken while changing the different parameters. All three optimisation procedures have been performed using a ZS detuning of -564 MHz, and a detuning of the spectroscopy beam of -3 MHz. Regarding the alignment optimisation, only slight improvements could be achieved. The ZS laser beam is strongly restricted in alignment due to the small tube the laser needs to pass. Furthermore, the ellipticity of the circular left-handed polarisation of the light has been changed while taking spectroscopy data. This optimisation procedure led to no significant improvements.

For completeness, the ZS light has also been focussed by adding a plano convex lens with a focal length of $f = 2$ m to the optical path of the ZS light right after the

output coupler of the ZS light. To align the lens to the laser beam, the beam with no lens in the optical path is reflected by a mirror onto a screen. The position of the beam hitting the screen is marked. Afterwards, the lens is added and aligned in such a way that the laser beam overlaps with the marked position on the screen. Furthermore, the beam shutter is closed to reflect the ZS laser beam outside the vacuum chamber to check the Gaussian shape of the laser beam. To control the spot size, a telescope is added to the optical path. Now, the signal strength is recorded while changing the spot size. For the setting of the focussing leading to the highest signal strength, a spectroscopic measurement has been taken. This is shown in comparison to the results obtained with the collimated ZS laser beam in Figure 7.6. In case of no focussing , the Zeeman slower is cooling the atoms more efficiently, leading to a higher signal strength of the peak corresponding to the Zeeman slowed atoms. The signals start to deviate for velocities below the capture velocity of the Zeeman slower.
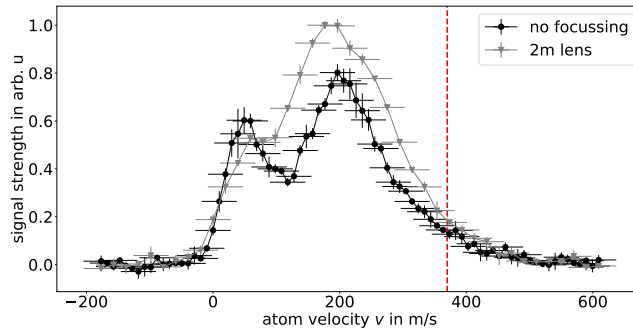

Figure 7.6.: Signal strength of the fluorescence as a function of δ_{spec} presented in the longitudinal velocity frame in case of focussing vs. no focussing. The black dots correspond to the spectroscopy data taken in case of no focussing, the grey triangles represent the data taken while focussing with a 2 m lens. The capture velocity of the Zeeman slower is indicated as red dashed line.

The same focussing procedure has been repeated using a different piano convex lens with a focal length of $f = 1\,\mathrm{m}$. With this lens no improvement of the Zeeman slower performance has been achieved.

Zeeman slower light power dependence

To complete the characterisation of the light of the Zeeman slower, we recorded the slowing efficiency as a function of the power. As a first step, to ensure that the peak of the slowed atoms appears at the same frequency, the spectroscopy signal is recorded for different values of the ZS power. This is shown in Figure 7.7 a).

Now the spectroscopy frequency of the 583 nm laser is set to a detuning of -3.5 MHz and the power of the light is scanned. The result of this measurement is shown in Figure 7.7 b). At approximately 40 mW of power, the fluorescence signal intensity approaches the maximum and starts to exhibit saturation. Beyond this power level, no significant improvement in strength of the fluorescence signal can be observed. This means, the number of atoms being effectively slowed by the Zeeman slower does not enhance for higher values of the power of the ZS laser beam.
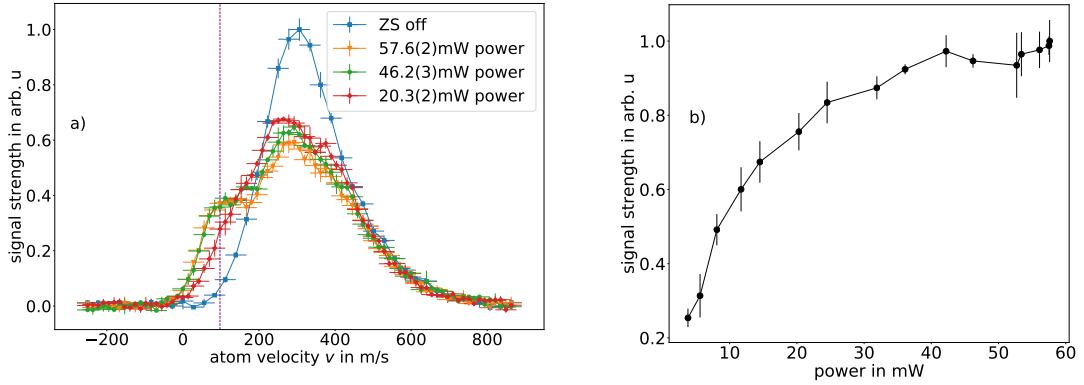
Figure 7.7.: Figure a) shows the spectroscopy signal for different powers of the Zeeman slower light. The purple dashed line marks the chosen spectroscopy frequency of -3.5 MHz at which the scan in power will be recorded. Figure b) shows the Zeeman slower light power curve. The normalised signal strength is measured as a function of the power of the ZS laser beam. This is indicated as black data points. The black line connects the individual data points and serves as a guide to the eye. The measurement has been repeated three times. The indicated data points correspond to the mean value of the normalised signal strength and the presented error bar corresponds to the standard deviation.

7.3. Zeeman Slower Performance Optimisation: Magnetic field

This section contains an analysis of the impact of the individual coils on the deceleration performance of the slower and the optimisation of the currents. Furthermore, the effect of scaling the peak-to-peak magnetic field on the slowing performance, as well as the effect of the transversal cooling on the ZS performance is studied.

Impact of the coils on the cooling performance

For the characterisation of the magnetic field of the Zeeman slower, as a first step the impact of the individual coils is examined by switching sections of the magnetic

field on and off. For this measurement, the current in coil 9 is again set to 10 A and the ZS detuning is set to -564 MHz. The spectroscopic results of the signal strength of the fluorescence for different settings of the magnetic field are shown in Figure 7.8.
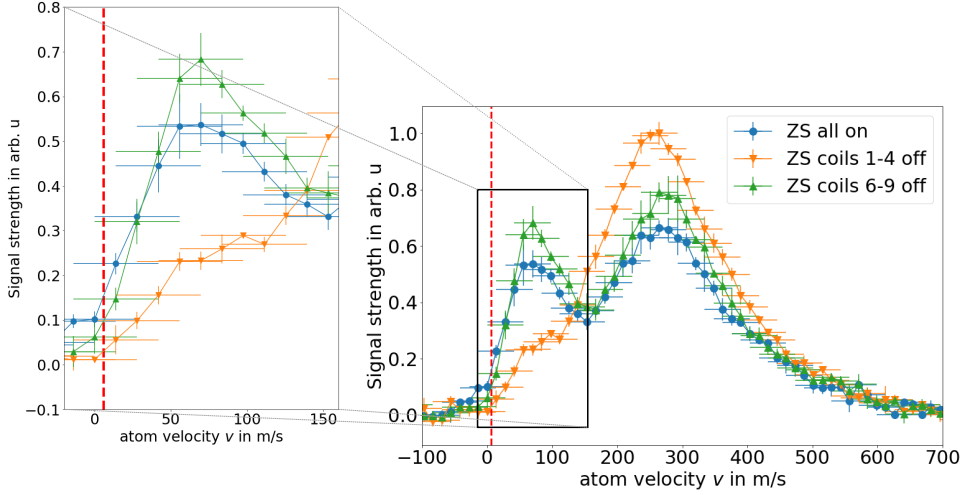

Figure 7.8.: Spectroscopic results of the signal strength of the fluorescence presented in the velocity frame for different settings of the magnetic field. The blue dots represent the strength of the fluorescence signal in case all coils are switched on, the orange down-pointing triangles correspond to the case where the first four coils are switched off and the green up-pointing triangles correspond to the case where the last four coils are switched off. The red dashed line marks the capture velocity of the MOT for spectroscopy performed under an angle $\alpha = -1.2(1)°$. For better visualisation of the peak corresponding to the Zeeman slowed atoms, this figure contains a zoomed version of the region confined by the black rectangle.

Let us start the discussion with the case where the first four coils are switched off. The strength of the fluorescence in the case where the first four coils are switched off is strongly reduced with respect to the other two cases (all coils on and coils 6-9 off). This means that the Zeeman slower is not working properly in this case. This is also expected from theory. As explained in Section 3.5, the magnetic field of the Zeeman slower has been designed to decelerate a certain fraction of the atoms being part of the velocity distribution. If the magnetic field is switched off in the first region of the ZS, the laser beam is not interacting with the atoms at the starting point of the ZS and thus the atoms are not decelerated. Only atoms of the thermal beam having such small velocities that they interact with the light for a magnetic field given by the last coils, are appearing as slowed atoms, probably explaining the weak bump still present. Now, let us have a look at the other two cases and let us have a look to the zoomed region. The maximum in signal strength of the

peak corresponding to the Zeeman slowed atoms in case all coils are on is slightly reduced in comparison to the case where the last four coils are switched off. But as only atoms with a capture velocity smaller than the capture velocity of the MOT are relevant for the experiment, the result obtained in case all coils are switched on is better.

Impact of coil 9

This section focusses on the impact of the current in coil 9 on the cooling performance of the Zeeman slower. To examine this, the signal strength of the fluorescence is recorded as a function of the detuning of the spectroscopy laser from resonance and transformed as explained above to the velocity frame for different values of the current in coil 9. The results are shown in Figure 7.9. These measurements have again been taken a ZS detuning of $-564\,\mathrm{MHz}$ and under an angle $\alpha = -1.7(1)°$. Furthermore, the currents running through the coils 1-8 of the Zeeman slower are set to their designated values.
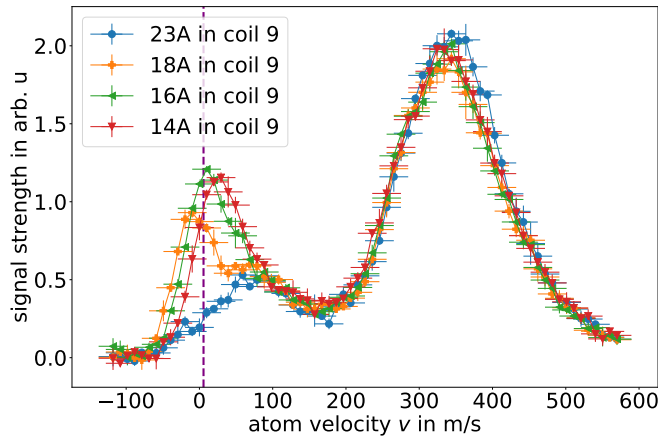

Figure 7.9.: Signal strength of the fluorescence as a function of the detuning of the spectroscopy laser from resonance represented in the velocity frame for different values of the current in coil 9. The capture velocity of the MOT is indicated as purple dashed line.

As shown in Figure 7.9, for a current of 14 A, the apparent peak of slowed atoms is almost equal in signal strength as the one obtained for a current of 16 A. However, the maximum of the apparent peak is further away from resonance in case of a current of 14 A than for a current of 16 A. As a consequence, the signal strength at the threshold (capture velocity of the MOT) is smaller for a current of 14 A. For a current of 18 A, the signal strength of the the peak is lower than for a current of 16 A. Under a current of 23 A, the performance of the Zeeman slower is strongly reduced

in comparison to the lower chosen currents in coil 9, visible as a strong loss in signal strength. This means that changing the current in coil 9 determines the position of the velocity distribution corresponding to the slowed atoms on this velocity axis. For too large currents in coil 9, the atoms are stopped or even accelerated into the opposite direction leading to a loss of atoms in the main chamber. This is also in agreement with what has been found in the simulation presented in Section 7.1. This means, the best result is obtained for a current of 16 A, as the signal strength of the fluorescence shows a maximum for this value and the maximum of the peak is close to the capture velocity of the MOT.

Streching of the magnetic field

One of the final measurements carried out in order to characterise and optimise the Zeeman slower examines the relationship between the strength of the fluorescence signal and the peak-to-peak magnetic field strength of the Zeeman slower. For this, a scaling procedure is employed, wherein each electric current is multiplied by a factor ranging from 0.4 to 1.2. This particular measurement was performed with the spectroscopy laser intersecting the erbium atomic beam at an angle $\alpha =1.7(1)°$. The signal strength of the recorded fluorescence signal as a function of the frequency detuning of the spectroscopy laser from resonance is shown for scaling factors ranging from 0.9 to 1.2 in Figure 7.10.
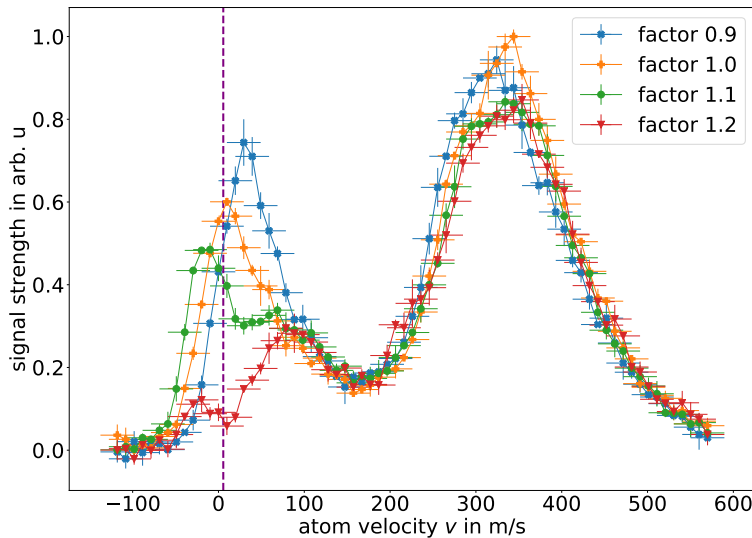

Figure 7.10.: Signal strength of the recorded fluorescence signal as a function of the frequency detuning of the spectroscopy laser from resonance represented in the velocity frame for scaling factors ranging from 0.9 to 1.2. For a factor of 1, the currents in coils number 1-8 are set to the designated currents, the current in coil number 9 is set to 10 A. For other factors the entire shape of the magnetic field is scaled up or down. The capture velocity of the MOT is indicated as purple dashed line.

As shown in Figure 7.10, focussing on the apparent peak of Zeeman slowed atoms near resonance, for higher factors the peak gets smaller in amplitude. Furthermore, the peak gets displaced more towards resonance. This means that for an up-scaling of the magnetic field, the atoms get slowed down towards smaller longitudinal velocities. At the same moment less cooled atoms reach the main chamber.

To further analyse these measurements, the spectroscopic results of the strength of the fluorescence signal are presented in the velocity frame in form of a heat map for all scaling factors. This is shown in Figure 7.11.
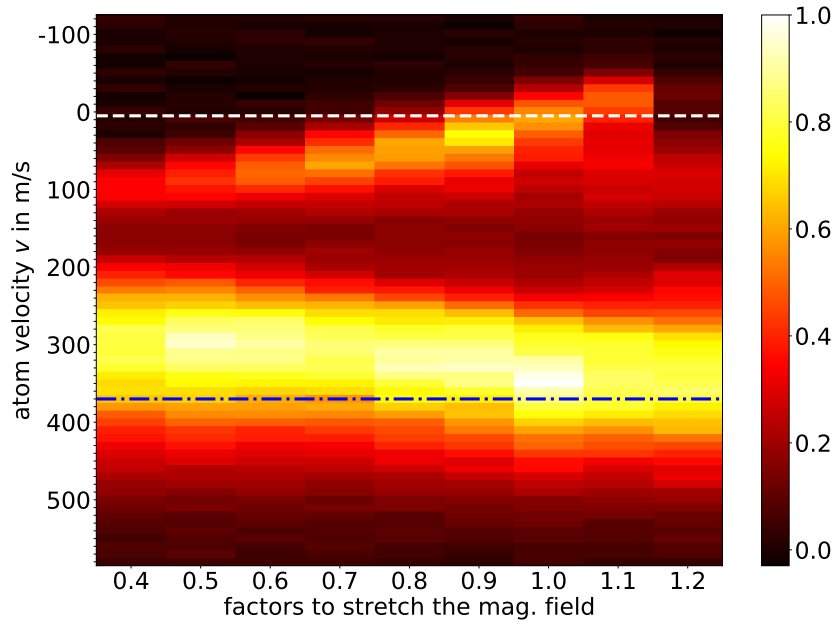

Figure 7.11.: Signal strength of the fluorescence signal as a function of the detuning of the spectroscopy laser from resonance for all scaling factors in range from 0.4 to 1.2. The Doppler shift corresponding to the capture velocity of the Zeeman slower as well as the Doppler shift corresponding to the capture velocity of the MOT are indicated as blue dash-dotted line and as white dashed line, respectively. The colour bar indicates the normalised signal strength of the fluorescence signal recorded in the main chamber.

Here, the maximum in signal strength of the peak corresponding to the Zeeman slowed atoms is pushed from a velocity of around $100\,\mathrm{m/s}$ to around $0\,\mathrm{m/s}$. Furthermore, the peak corresponding to the Zeeman slowed atoms has a maximum in signal strength for a scaling factor of 0.9. However, the atoms have to be slowed down below the capture velocity of the MOT to be able to get trapped. This would be beyond the white dashed line. By looking at the intersection of the dashed white line and the maximum in signal strength corresponding to the Zeeman slowed atoms, a factor of 1 leads to better results. For factor 1.2 almost no Zeeman slowed atoms can be observed, as the atoms are slowed to zero-velocity before they reach the

main chamber or are even accelerated into the opposite direction, moving away from the main chamber. Looking at the peak in signal strength corresponding to the non-Zeeman slowed atoms, the maximum in signal strength is shifted further from resonance for larger scaling factors. This is also expected from theory as the frequency of the ZS laser beam stays constant, but the strength of the magnetic field in enhanced. This leads to a different Zeeman shift induced by the magnetic field and thus to a different capture velocity of the Zeeman slower.

Furthermore, as known from the previous section, enhancing the current in coil 9 can be used to reduce the final velocity of the atoms. Therefore, we performed a measurement directly comparing the situation where the current in coil 9 is enhanced to 16 A while maintaining the current values corresponding to factor 0.9 for coils number 1-8 with the settings from the previous result with factor 1. As shown in Figure 7.12, the maximum of the peak corresponding to the slowed atoms has been shifted more towards resonance for a factor of 0.9 and 16 A in coil 9, in comparison to the result of factor 1 shown in Figure 7.11. The position of the maximum for a scaling factor of 1 and for a scaling factor of 0.9 with enhanced current of 16 A in coil 9 are almost at the same distance from the threshold indicated as purple dashed line, but the signal strength of the data corresponding to factor 0.9 and 16 A in coil 9 is higher. Thus, the setting of magnetic fields corresponding to factor 0.9 and 16 A is considered to give better results.
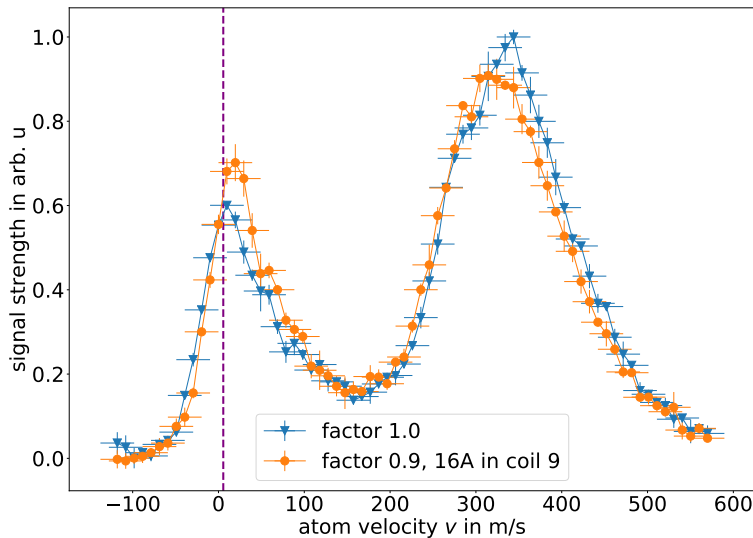

Figure 7.12.: Signal strength of the recorded fluorescence signal as a function of the frequency detuning of the spectroscopy laser from resonance presented in the velocity frame for scaling factor 1 indicated as blue triangles and for a scaling factor 0.9 with enhanced current of 16 A in coil 9.

Effect of transversal cooling on the Zeeman slower performance

To complete the characterisation of the Zeeman slower, spectroscopy data is taken for the optimised settings of the ZS (factor 0-9 and 16 A in coil 9), first with the TC being on and then with the TC being off. This is shown in Figure 7.13. We observe, that the transversal cooling enhances the signal strength in the main chamber significantly. The signal strength of the peak corresponding to the slowed atoms is enhanced by about a factor four. The signal strength of the atoms not slowed by the Zeeman slower is enhanced by about a factor five, as also found in the measurements presented in Section 6.2.

With this measurement, the characterisation of the experimental tools needed to prepare an ensemble of erbium atoms being slow enough to be trapped in the MOT is concluded. This is an important step towards the planned quantum simulation experiments performed with atoms trapped in optical tweezers which are directly loaded from the MOT and excited to Rydberg states.
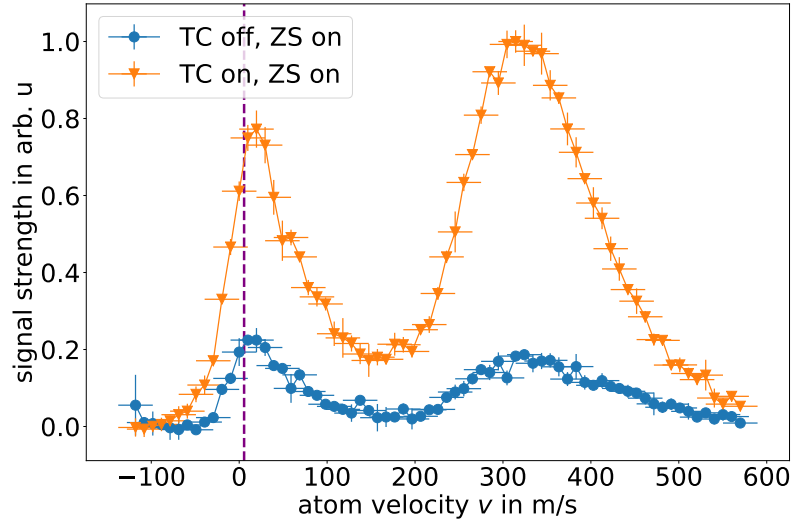

Figure 7.13.: Signal strength of the fluorescence as a function of the detuning of the spectroscopy laser from resonance presented in the velocity frame for the optimised settings of the ZS, once in case of TC on (orange triangles) and once in case of TC off (blue dots). The capture velocity of the MOT is indicated as dashed purple line.

8. Rydberg atoms

In principle, the aim of the TREQS experiment is to trap ultracold erbium atoms in optical tweezers, enabling controlled engineering of scalable many-body systems for quantum information processing, quantum simulations, and precision measurements. As demonstrated in [5] for ^{87}Rb atoms it is possible to produce defect-free one-dimensional cold atom arrays, as well as two-dimensional atomic arrays of the same atom species in [6]. These tweezers are loaded directly from a MOT. For the envisioned applications it is needed that the atoms interact with each other in a very controlled way. To enable those interactions between the atoms trapped in the tweezers, it is common to excite that the atoms into so-called Rydberg states.

Highly excited atoms, so-called Rydberg atoms, have already been studied in the 19th century. Atoms in a so-called Rydberg state possess a highly excited electron that is loosely bound and far away from the core, approximately experiencing a $1/r$-potential rendering Rydberg atoms similarly to hydrogen atoms. In 1885, Johann Jakob Balmer established an empirical formula to describe the spectral lines of hydrogen by relating the wavelengths of the hydrogen spectrum. This formula is given by

$$\lambda = \frac{bn^2}{n^2 - 4}, \tag{8.1}$$

with $b = 3645.6$ Å [57]. The first theoretical description relating the spectra of the hydrogen atom to the binding energy of the electron has been provided by Bohr reading

$$E_n = -hc\frac{R_\infty}{n^2} \tag{8.2}$$

with h being the Planck constant, c the speed of light and n the principal quantum number. The Rydberg constant R_∞ can be expressed in terms of fundamental constants as

$$R_\infty = -\frac{m_e e^4}{8c\epsilon_0^2 h^3}.$$

Here e denotes the elementary charge, m_e the mass of the electron and ϵ_0 the vacuum permittivity [58]. The formula that has been established by Balmer worked only for hydrogen and only for transitions from or to $n = 2$. To overcome this limitation the formula has later been extended and generalised to other chemical elements by

Rydberg [59].

8.1. Properties of Alkali Rydberg atoms

Alkali atoms are atoms that possess only one valence electron. The other electrons fill up the inner shells of the atom and are tightly bound to the atomic core. For highly excited states, the core and the valence electron form a hydrogen-like system. However, there are several effects that need to be taken into account such as the penetration of the substructure of the core in case of electronic states with low angular momentum quantum number l. Furthermore, the valence electron experiences an increased charge inside the core because of the reduced shielding of the nucleus. These effects are considered in the so-called quantum defect theory [60]. According to this theory, the Equation (8.2) stated by Bohr transforms to

$$E_{n,l} = -hc\frac{R_\infty}{(n^*)^2} = -hc\frac{R_\infty}{(n-\delta_l)^2},\tag{8.3}$$

by introducing the so called effective principal quantum number $n^* = n - \delta_l$. Here δ_l denotes the so-called quantum defect which depends on the orbital angular momentum quantum number l.

Table 8.1.: Scaling of the most important properties of Rydberg atoms with the principal quantum number n. Table taken from [61].

property	quantity	scaling
energy levels	E_n	n^{-2}
level spacing	ΔE_n	n^{-3}
radius	$\langle r \rangle$	n^2
transition dipole moment ground to Rydberg state	$\lvert \langle nl \rvert - er \lvert g \rangle \rvert$	$n^{-3/2}$
radiative lifetime	τ	n^3
transition dipole moment for adjacent Rydberg states	$\lvert \langle nl \rvert - er \lvert nl' \rangle \rvert$	n^2
resonant dipole-dipole interaction coefficient	C_3	n^4
polarisability	α	n^7
van der Waals interaction potential	C_6	n^{11}

However, in comparison to an atom in its ground state Rydberg atoms exhibit exaggerated properties such as large electric dipole moments leading to strong interactions with external fields. As stated in [62], already more then two decades ago, it was proposed that these properties of Rydberg atoms scaling with the principle quantum number n as summarised in Table 8.1, can be advantageous to implement quantum gates between neutral atom qubits. The strong long range-interaction,

that can be coherently controlled, enables the implementation of platforms capable to realise long-range two-qubit gates, collective encoding of multiqubit registers, robust light-atom quantum interfaces and also quantum many-body simulators. The following sections will delve into these interactions.

8.2. Rydberg interactions

Due to virtual photon exchange between atoms in Rydberg states, strong interactions can be observed. There are two different possibilities of initial state occupations, that lead to different types of interactions, as explained in the following. This section is, if not stated otherwise, based on [63].

Dipole-dipole interaction

For an atom in a state with some principal quantum number n and zero angular momentum S the notation $|nS\rangle$ is introduced. The second atom is in a state with principal quantum number $n-1$ and an angular momentum of $\hbar$ coded as P with notation $|(n-1)P\rangle$. In case the first atom emits a photon that excites the second atom, the process $|nS, (n-1)P\rangle \rightarrow |(n-1)P, nS\rangle$ can be observed. For the two coupled states $|nS\rangle$ and $|(n-1)P\rangle$ the spatial integral $\langle nS|e\hat{\vec{r}}|(n-1)P\rangle \propto n^2$ gives the dipole matrix element that characterises the coupling strength between the two states.

For the process of re-absorption of the emitted photon, the coupling strength is again proportional to n^2. This leads to a scaling of the entire interaction with the principal quantum number n and the interatomic distance R as n^4/R^3. This kind of interaction strength from different Rydberg states is called dipole-dipole interaction.
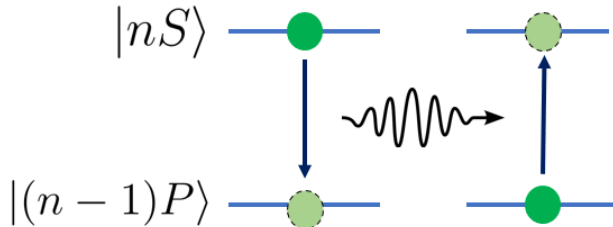

Figure 8.1.: Resonant dipole-dipole interaction. Initially, there is an atom in a state $|nS\rangle$ and a second atom in a state $|(n-1)P\rangle$. In case the first atom emits a photon that excites the second atom, the process $|nS, (n-1)P\rangle \rightarrow |(n-1)P, nS\rangle$ can be observed. This graphic has been inspired by [63].

Van der Waals interaction

In the second case we start with two atoms occupying the same Rydberg state, e.g. $|nS\rangle$. If one of the two atoms decays to a lower lying state $|n'P\rangle$ by spontaneous emission of a photon, the second atom can again absorb this photon and can be excited to a higher lying state $|n''P\rangle$. In the most cases, regarding the second atom, there is no higher lying state the atom can be excited to with an energy that is equal to the energy gap between the $|nS\rangle$ and the $|n'P\rangle$ states. This leads to the so-called energy defect that is defined as $\Delta_E = E(n'P, n''P) - E(nS, nS)$. However, due to the imprecise definition of energy on short time scales, the process can occur in case of sufficiently strong coupling. After this process, the photon can again be exchanged and the atomic population returns to the initial state occupation. The strength of the entire second-order process known as van der Waals interaction needs to be calculated by involving second-order perturbation theory. This kind of interaction scales with the principal quantum number n and the interatomic distance R as n^{11}/R^6.
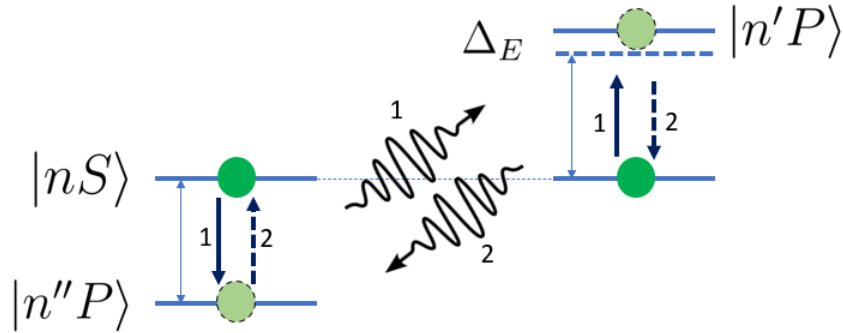

Figure 8.2.: Off-resonant Van der Waals interaction. Initially, there are two atoms occupying the same Rydberg state, e.g. $|nS\rangle$. If one of the two atoms decays to a lower lying state $|n'P\rangle$, the second atom can again absorb this photon and can be excited to a higher lying state $|n''P\rangle$. The energy gap between the $|nS\rangle$ and the $|n'P\rangle$ states leads to the so-called energy defect that is defined as $\Delta_E = E(n'P, n''P) - E(nS, nS)$. This graphic has been inspired by [63].

The Rydberg interactions are switchable as well as tunable, bringing new opportunities depending on the chosen Rydberg state in combination with the applied external fields. Furthermore, the interaction strength can be tuned additionally by controlling the distance between the atoms.

The strong interactions of Rydberg atoms can for example be used to prevent simultaneous excitation of two atoms into a Rydberg state. This effect, known

as Rydberg blockade, provides a mechanism enabling entanglement of atoms used as a resource for quantum information processing, for quantum metrology or for quantum correlated systems [64].

Rydberg blockade

Starting with a pair of atoms, one in the Rydberg state and one in the ground state, the Rydberg level of the atom in the ground state is shifted in energy by an amount corresponding to the interaction strength V of the two-atom system. At a large distance between the two atoms, this energy shift is small compared to the natural transition rate γ, as the interaction strength scales as $V \propto n^4/R^3$ in case of resonant dipole-dipole interaction and as $V \propto n^{11}/R^6$ for off-resonant van der Waals with the interatomic distance R. This means, the atom in the ground state can be excited with approximately the same dynamics as in the absence of the Rydberg atom.

However, at a certain interatomic distance known as Rydberg blockade radius R_{B}, the shift of the Rydberg level of the atom in the ground state becomes larger than the natural linewidth. For interatomic distances being smaller than this blockade radius, the atom in the ground state in completely decoupled from the driving field and the Rydberg excitation is suppressed.

8.3. Multi-valence-electron Rydberg atoms of erbium: Rydberg excitation using electromagnetically induced transparency

Since more than one century Rydberg atoms are an important subject of research, being highly successful in realising strongly interacting many-body quantum simulators. The TREQS experiment aims to simulate such many-particle quantum systems by driving Rydberg excitations in tweezer-trapped neutral erbium atoms, satisfying the conditions of strong interactions, long internal state coherence and microscopic control [2]. As it has been shown in [65], Rydberg atoms in optical or magnetic lattices can provide an efficient implementation of a universal quantum simulator for spin models, reproducing the dynamics of any other many-particle quantum system with short range interactions. In early Rydberg experiments it has been common to use alkali metals such as rubidium and cesium due to their favourable laser excitation schemes. However, in the last years there has been growing interest in extending the investigations to more complex atomic species, such as lanthanide erbium, remaining optically active upon a single Rydberg excitation and thus facilitating more possibilities for the manipulation of the Rydberg atoms [50]. Furthermore, the rich electronic energy level structure of lanthanoids provides many possibilities for different Rydberg excitation paths.

To excite the atom to a Rydberg state it is common to use a technique called two-photon excitation, as the large energy difference between the ground state and the excited state would require a laser with a wavelength in the ultraviolet (UV) region. These UV lasers are technically challenging and in that case additional processes like spurious ionisation are happening. In case of erbium the valence electrons are distributed to the *f*- and *s*-shells, leading to many possible excitation schemes. For the valence electrons in the *s*-shell transitions to the *p*-shell for the intermediate state are allowed according to the selection rules related to the angular orbital momentum quantum number *l*. The intermediate state can than be coupled to the *s*- or *d*-shell for the Rydberg state. In case of the valence electrons of the *f*-shell transitions to the *d*- or *g*-shells for the intermediate state are allowed. The intermediate state can then be coupled to *p*-, *g*- or *h*-shells for the Rydberg state. Such open-shell Rydberg lanthanides are rather unexplored in their special characteristics for ultracold gas experiments.

Within the frame of this thesis, the paper "Spectroscopy of Rydberg states in erbium using electromagnetically induced transparency" [66] has been published. In this paper a study of the first high-resolution spectroscopy on the Rydberg spectrum in ^{166}Er for the Rydberg series connected to the $4f^{12}(^3H_6)6s$, $J_c = 13/2$ and $J_c = 11/2$ ionic core states is presented. The spectroscopy has been performed in the beam shutter section being part of the ultrahigh vacuum setup of the TREQS experiment. For this measurements, the vacuum-setup consisted of the high temperature oven, the transversal cooling chamber, the differential pumping section and the beam shutter section (the so-called probe chamber). The detection of the Rydberg states is implemented using a two-photon excitation scheme based on electromagnetically induced transparency (EIT). With this all-optical detection scheme, ns and nd Rydberg series with principal quantum numbers n ranging from 15 up to 140 can be observed. For this two-photon excitation scheme the ground state $[4f^{12}(^3H_6)6s^2(^1S_0)]_6$ is coupled to the intermediate state $[4f^{12}(^3H_6)6s6p(^1P_1)]_7$ according to the notation introduced in Section 2.2 and Section 2.3 using the so-called probe beam. A second laser beam, the so-called coupling beam couples the intermediate state to the Rydberg state, e.g. the $4f^{12}(^3H_6)6s(^{S_{1/2}})$ with a laser operating at a wavelength of approximately 411 nm. The probe laser is intersected perpendicularly with the erbium atomic beam and experiences absorption in case the laser is on resonance with the atomic transition to the intermediate state. Furthermore, the coupling laser is overlapped with the probe laser and propagating in opposite direction. In case the coupling laser is on resonance with the atomic transition from the intermediate state to the Rydberg state, this leads to a transparency window at resonance. Using this technique, about 550 EIT resonances have been recorded. To these resonances, the total energy is assigned, as well as the effective quantum number after the determination of the lowest ionisation threshold.

To fully assign the large number of nd states, their total angular momentum J is determined by performing a Zeeman spectroscopy on each state. For this purpose, a homogeneous magnetic field is applied. This magnetic field is generated by two temporarily added coils in Helmholtz configuration, leading to a strength of the magnetic field in the center region of 10.7(5) G. The coils in Helmholtz configuration mounted around the beam shutter section are shown in Figure 8.3.
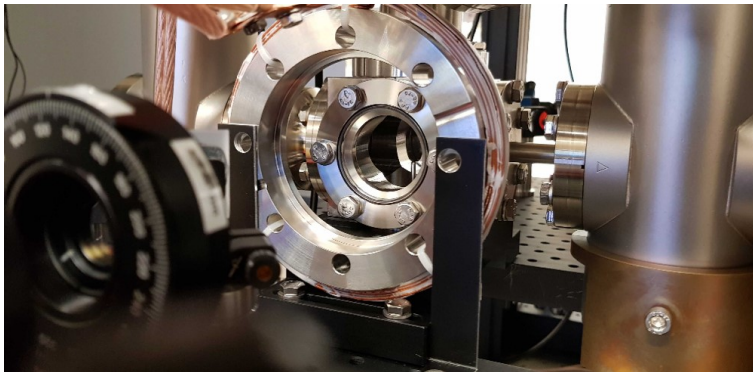

Figure 8.3.: Coils in Helmholtz configuration mounted around the beam shutter section in order to generate a homogeneous magnetic field of 10.7(5) G needed for the Zeeman spectroscopy.

To be able to determine the total angular momentum J, we use the appearing patterns of the Zeeman states recorded performing Zeeman spectroscopy. For this, the selection rules, as well as the polarisation of the probe beam and the coupling beam need to be considered. Furthermore, the initial state occupation due to partial optical pumping towards the stretched states of the ground state resulting from different Clebsch-Gordan coefficients of the first transition are taken into consideration. The spectral pattern is dominated by the relative two-photon transition strength that can be calculated from the transition matrix elements for each single-photon transition. Using the Wigner $3j$-Symbol, the transition matrix element for the transition from the ground state (gs) to the intermediate state (ex) is given by

$$C_{m_{\text{gs}},m_{\text{ex}}} = (-1)^{J_{\text{gs}}-1+m_{\text{ex}}}\sqrt{2J_{\text{gs}}+1}\begin{pmatrix} J_{\text{gs}} & 1 & J_{\text{ex}} \\ m_{\text{gs}} & \Delta m & -m_{\text{gs}} \end{pmatrix}. \tag{8.4}$$

Here J_{gs} and J_{ex} denote the total angular momentum of the ground state and the excited state, respectively. Furthermore, m_{gs} and m_{ex} represent the corresponding magnetic quantum numbers. For the transition from the intermediate state to the Rydberg state (J) the single-photon transition matrix element is given by

$$C_{m_{\text{ex}},m_J} = (-1)^{J_{\text{ex}}-1+m_J}\sqrt{2J_{\text{ex}}+1}\begin{pmatrix} J_{\text{ex}} & 1 & J \\ m_{\text{ex}} & \Delta m & -m_J \end{pmatrix}. \tag{8.5}$$

Here J denotes the total angular momentum of the Rydberg state with correspond-

ing magnetic quantum numbers m_J. The results for the transition matrix element for both single-photon transitions is shown in Figure 8.4. The relative two-photon transition strength is given by $|C_{m_{\mathrm{gs}}, m_{\mathrm{ex}}} \times C_{m_{\mathrm{ex}}, m_J}|$.
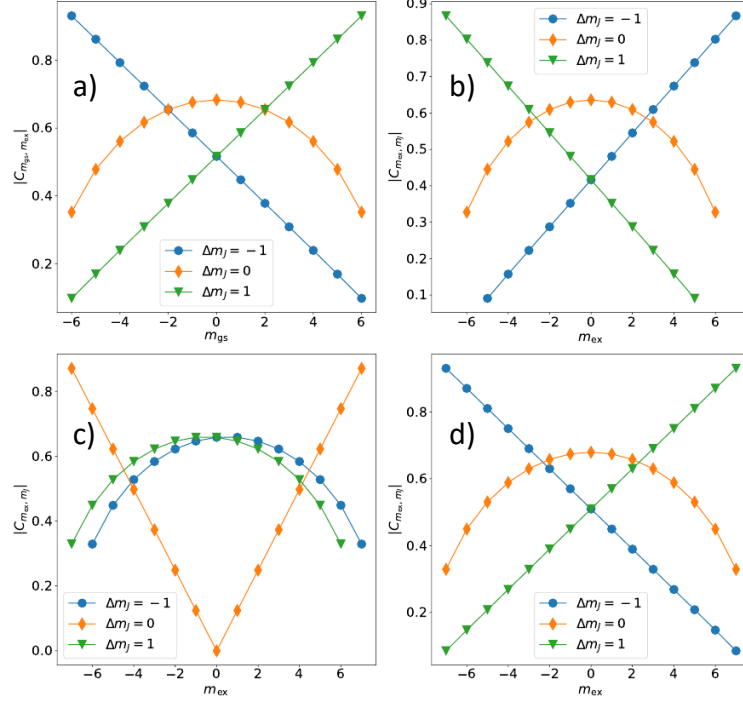

Figure 8.4.: Absolute values of the transition matrix elements of the single-photon transitions from the ground to the intermediate state and for the three possible transitions from the intermediate state to the Rydberg state. The blue (orange) circles (squares) correspond to σ^- (π) transitions. The green triangles represent σ^+ transitions. In a) transition matrix element for the transition $|J_{\mathrm{gs}} = 6, m_{\mathrm{gs}}\rangle \rightarrow |J_{\mathrm{ex}} = 7, m_{\mathrm{ex}}\rangle$, in b) for $|J_{\mathrm{ex}} = 7, m_{\mathrm{ex}}\rangle \rightarrow |J = 6, m_J\rangle$, in c) for $|J_{\mathrm{ex}} = 7, m_{\mathrm{ex}}\rangle \rightarrow |J = 7, m_J\rangle$ and in d) for $|J_{\mathrm{ex}} = 7, m_{\mathrm{ex}}\rangle \rightarrow |J = 8, m_J\rangle$.

9. Conclusion and Outlook

The aim of this thesis has been to characterise and optimise the laser cooling and deceleration tools needed to produce a ensemble of erbium atoms that can be trapped in a MOT to be subsequently loaded into optical tweezers and excited to Rydberg states for quantum simulation purposes. Usually, such characterisation and optimisation processes are performed with the atoms that are trapped in the MOT. However, this pre-work performed within the frame of this thesis led to a better understanding of the given experimental setup and of the individual parameters such as laser frequencies and magnetic field strengths that can be varied. The influence of the parameters on the control of the final velocity of the atoms reaching the main chamber has been studied and the manipulation of the given velocity distribution of the atoms has been optimised. Thanks to this characterisation, the implementation of the MOT will be much easier and the number of atoms loaded into the MOT will be optimal. To obtain an intuitive understanding on the manipulation of the velocity distribution of a thermal beam of erbium atoms, a detailed but also intuitive explanation on the action of the radiation pressure on atoms has been given. In addition, the optical molasses forming the transversal cooling mechanism needed to collimate the atomic beam has been introduced. Furthermore, also the Zeeman slower, which can be understood as magneto-optical deceleration mechanism, has been introduced.

The main body of this thesis presents the results obtained from the optimisation and characterisation measurements. From the differential absorption spectroscopy measurement, first results on the action of the TC on the transversal velocity distribution have been obtained. Furthermore, to understand which broadening mechanism dominates the recorded signal, the differential spectroscopy signals have been analysed using different fitting models. From the analysis it can be concluded, that the shape of the signal is dominated by the natural broadening.

From the spectroscopic measurement with fluorescence imaging performed in the main chamber resulted that the transversal cooling (heating) works the most efficient for a detuning of $-12\,\text{MHz}$ ($26\,\text{MHz}$). In addition, the polarisation insensitivity of the TC has been observed and the power characteristics of the TC have been recorded. From the optimisation of the light of the Zeeman slower, an ideal ZS detuning of $-564\,\text{MHz}$ has been found. Additionally, the effect of focussing of the Zeeman slower light has been tested leading to the conclusion that focussing is leading to a loss in signal strength. Testing the performance of the slower in

91

dependence of the polarisation of the light led to the conclusion that perfectly circular polarisation leads to the best result. To complete the characterisation of the Zeeman slower light, the power characteristics have been recorded. As next step, the dependence of the slower performance on the magnetic field has been examined. In case of a zero magnetic field in the first section of the slower a strong signal loss could have been observed. In case of a zero magnetic field in the last part of the slower, the obtained peak of slowed atoms has been shifted to higher velocities. In addition, the impact of the last coil on the final velocity has been tested. It has been shown, that the last coil can be used to control the final velocity. Also changing the peak-to-peak magnetic field strength led to the results expected from theory. To complete the characterisation of the Zeeman slower, a spectroscopic measurement with optimised settings of the slower has been taken in case of TC on comparing it to the case of TC off. It has been shown, that the transversal cooling enhances the obtained signal strength by about factor 4. In the last part of this thesis, a short introduction to Rydberg atoms has been given delving into the special properties that this atomic state provides. This is followed by the summary of the paper published within the frame of this thesis presenting the first high-resolution spectroscopy on the Rydberg spectrum in ^{166}Er.

Summarising, this thesis presents a pre-optimisation and characterisation work on the cooling and deceleration mechanisms needed to obtain a signal for the MOT. The influence of the individual parameters has been tested and characterised leading to a good understanding on the processes within the apparatus in the individual sections of the experiment. The next step will be the implementation of the MOT with similar optimisation and characterisation work. In addition, the setup needs to be extended to implement a linear tweezer array using a laser operating at 488 nm. The loading of the tweezer arrays then needs to be optimised to provide single atoms with high efficiency and fidelity. When this is done, the linear tweezer arrays will be extended to two-dimensional arrays, similarly as performed in [6]. Furthermore, in-trap cooling techniques such as sisyphus cooling and sideband cooling will be studied. Then, the spectroscopy of Rydberg states needs to be extended to the trapped atoms and an imaging scheme needs to be developed. When these preparations have been made, quantum simulation models will be tested.

List of Figures

List of Tables

96

A. Appendix

A.1. Control via the bus system and magnetic fields

As a first step after the software part of the control system on the computer, the computer and the bus system are linked via a National Instruments digital output card NI6533. This card is connected to the first bus driver card as shown in Figure A.1. All bus driver cards are isolating as the ground of the computer is connected to earth. To the first bus driver crad, the 2 MHz clock for timing the NI6533 card, as well as the trigger generator are connected. Both are synchronised with the 50 Hz line. At the first bus driver the bus direction signal is disconnected from the NI6533 card and connected permanently to the +5 V. The broad 50 pin cable coming out of the first bus driver card contains data, address and clock. Every bus driver card can be connected to a subbus. The thin 16 pin cable contains the address of the subbus. The subbus address as well as the address of the analog output cards can be set at the DIP switches on each box. For switching the Zeeman slower coils in the T-REQS experiment subbus 5 is used. Before reaching the subbus decoder and the strobe generator, both flat ribbon cables pass the buffer box. The subbus is than connected to the analog boxes. The BNC outputs of the analog boxes are connected via BNC to D-Sub adapters to the powersupplies that are connected to the magnetic field coils of the Zeeman slower. In the software that controls the experiment, the values that are set for the individual magnetic field coils of the Zeeman slower correspond to the voltage at the output of the power supplies. But as the relevant quantity with known value for each coil is given by the current, a calibration needs to be implemented. The currents running through each coil are measured for different values of the voltage set on the computer with a current probe. The measured data is fitted with a function of the form $f(x) = A + B * x + C * x^2$. In the matlab code used for controlling the experiment, the quadratic part is neglected.

A. Appendix

Table A.1.: Values of the fit parameters A, B and C for the voltage-current characteristics of the Zeeman slower coils.

coil number	A in V	B in V/A	C in V^2/A
coil 1	0.002(3)	0.480(1)	0.0001(1)
coil 2	0.003(2)	0.4912(9)	-0.00012(9)
coil 3	0.007(8)	0.4894(4)	-0.00011(4)
coil 4	0.003(2)	0.4931(8)	0.00005(6)
coil 5	0.002(2)	0.251(1)	-0.00035(9)
coil 6	-0.001(1)	0.4927(5)	0.00005(5)
coil 7	0.001(1)	0.4893(5)	0.00003(5)
coil 8	0.0020(9)	0.4931(4)	0.00008(4)
coil 9	0.004(3)	0.2497(9)	0.00020(6)
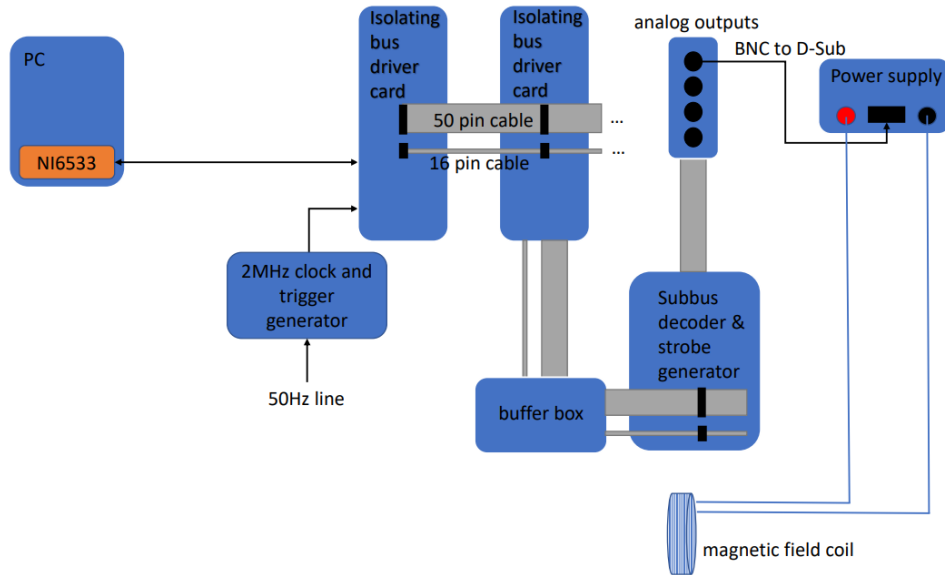
Figure A.1.: Schematic of the hardware used to control the magnetic fields of the Zeeman slower with signals transmitted through a card from National Instruments NI6533. Graphic inspired by [67].

Bibliography

[1] R. P. FEYNMAN, *Simulating physics with computers*, International journal of theoretical physics, **21**(6/7), 467 (1982).

[2] A. BROWAEYS UND T. LAHAYE, *Many-body physics with individually controlled Rydberg atoms*, Nature Physics, **16**(2), 132–142 (2020). URL `http://dx.doi.org/10.1038/s41567-019-0733-z`.

[3] T. SECKER, R. GERRITSMA, A. W. GLAETZLE UND A. NEGRETTI, *Controlled long-range interactions between Rydberg atoms and ions*, Phys. Rev. A, **94**, 013420 (2016). URL `http://dx.doi.org/10.1103/PhysRevA.94.013420`.

[4] X. WU, X. LIANG, Y. TIAN, F. YANG, C. CHEN, Y.-C. LIU, M. K. TEY UND L. YOU, *A concise review of Rydberg atom based quantum computation and quantum simulation**, Chinese Physics B, **30**(2), 020305 (2021). URL `http://dx.doi.org/10.1088/1674-1056/abd76f`.

[5] M. ENDRES, H. BERNIEN, A. KEESLING, H. LEVINE, E. R. ANSCHUETZ, A. KRAJENBRINK, C. SENKO, V. VULETIC, M. GREINER UND M. D. LUKIN, *Atom-by-atom assembly of defect-free one-dimensional cold atom arrays*, Science, **354**(6315), 1024 (2016). `https://www.science.org/doi/pdf/10.1126/science.aah3752`, URL `http://dx.doi.org/10.1126/science.aah3752`.

[6] D. BARREDO, S. DE LÉSÉLEUC, V. LIENHARD, T. LAHAYE UND A. BROWAEYS, *An atom-by-atom assembler of defect-free arbitrary two-dimensional atomic arrays*, Science, **354**(6315), 1021–1023 (2016). URL `http://dx.doi.org/10.1126/science.aah3778`.

[7] C. G. MOSANDER, *On the new metals, Lanthanium and Didymium, which are associated with Cerium; and on Erbium and Terbium, new metals associated with Yttria*, Philosophical magazin and journal of science, **552**, 241 (1843).

[8] J. R. RUMBLE, *ed. CRC handbook of chemistry and physics: a ready-reference book of chemical and physical data. 100th ed. CRC Press*, Taylor & Francis Group (2019), ISBN 9781138367296.

Bibliography

[9] K. Aikawa, A. Frisch, M. Mark, S. Baier, R. Grimm und F. Ferlaino, *Reaching Fermi Degeneracy via Universal Dipolar Scattering*, Phys. Rev. Lett., **112**, 010404 (2014). URL http://dx.doi.org/10.1103/PhysRevLett.112.010404.

[10] C. Patrignani, *Review of Particle Physics*, Chinese Physics C, **40**(10), 100001 (2016). URL http://dx.doi.org/10.1088/1674-1137/40/10/100001.

[11] A. Frisch, *Dipolar Quantum Gases of Erbium*, University of Innsbruck (2014).

[12] D. F. Babik, *Bose-Einstein condensation of erbium atoms for fractional quantum Hall physics*, Dissertation, Rheinische Friedrich-Wilhelms-Universität Bonn (2020).

[13] G. Gsaller, *Visualising Atomic Orbitals*. 2007.

[14] H. Y. Ban, M. Jacka, J. L. Hanssen, J. Reader und J. J. McClelland, *Laser cooling transitions in atomic erbium*, Opt. Express, **13**(8), 3185 (2005). URL http://dx.doi.org/10.1364/OPEX.13.003185.

[15] E. A. D. Hartog, J. P. Chisholm und J. E. Lawler, *Radiative lifetimes of neutral erbium*, **43**(15), 155004 (2010). URL http://dx.doi.org/10.1088/0953-4075/43/15/155004.

[16] W. Gerlach und O. Stern, *Der experimentelle Nachweis der Richtungsquantelung im Magnetfeld*, Zeitschrift fur Physik, **9**(1), 349 (1922). URL http://dx.doi.org/10.1007/BF01326983.

[17] B. R. Judd und I. Lindgren, *Theory of Zeeman Effect in the Ground Multiplets of Rare-Earth Atoms*, Phys. Rev., **122**, 1802 (1961). URL http://dx.doi.org/10.1103/PhysRev.122.1802.

[18] J. G. Conway und B. G. Wybourne, *Low-Lying Energy Levels of Lanthanide Atoms and Intermediate Coupling*, Phys. Rev., **130**, 2325 (1963). URL http://dx.doi.org/10.1103/PhysRev.130.2325.

[19] W. Martin, R. Zalubas und L. Hagan, *Atomic Energy Levels-The Rare-Earth Elements* (1978).

[20] N. F. Ramsey und J. Trischka, *Molecular Beams*, American Journal of Physics, **25**(1), 48 (1957). https://pubs.aip.org/aapt/ajp/article-pdf/25/1/48/12145508/48_2_online.pdf, URL http://dx.doi.org/10.1119/1.1996085.

[21] J. Schindler, *Characterization of an Erbium Atomic Beam* (2011).

[22] P. T. Greenland, M. A. Lauder und D. J. H. Wort, *Atomic beam velocity distributions*, Journal of Physics D: Applied Physics, **18**(7), 1223 (1985). URL http://dx.doi.org/10.1088/0022-3727/18/7/009.

[23] E. Staub, *Developing a High-Flux Atomic Beam Source for Experiments with Ultracold Strontium Quantum Gases* (2019).

[24] A. Einstein, *Zur Quantentheorie der Strahlung*, Phys. Z., **18**, 121 (1917).

[25] R. Frisch, *Experimenteller Nachweis des Einsteinschen Strahlungsrückstoßes*, Zeitschrift für Physik, **86**, 42 (1933).

[26] T. W. Hänsch, *Repetitively Pulsed Tunable Dye Laser for High Resolution Spectroscopy*, Appl. Opt., **11**(4), 895 (1972). URL http://dx.doi.org/10.1364/AO.11.000895.

[27] Y. Wang, S. Shevate, T. M. Wintermantel, M. Morgado, G. Lochead und S. Whitlock, *Preparation of hundreds of microscopic atomic ensembles in optical tweezer arrays*, npj Quantum Information, **6**(1) (2020). URL http://dx.doi.org/10.1038/s41534-020-0285-1.

[28] L. Henriet, L. Beguin, A. Signoles, T. Lahaye, A. Browaeys, G.-O. Reymond und C. Jurczak, *Quantum computing with neutral atoms*, Quantum, **4**, 327 (2020). URL http://dx.doi.org/10.22331/q-2020-09-21-327.

[29] X. Zhang, K. Beloy, Y. S. Hassan, W. F. McGrew, C.-C. Chen, J. L. Siegel, T. Grogan und A. D. Ludlow, *Subrecoil Clock-Transition Laser Cooling Enabling Shallow Optical Lattice Clocks*, Phys. Rev. Lett., **129**, 113202 (2022). URL http://dx.doi.org/10.1103/PhysRevLett.129.113202.

[30] L. A. Orozco, *Laser cooling and trapping of neutral atoms*, AIP Conference Proceedings, **464**(1), 67 (1999). https://aip.scitation.org/doi/pdf/10.1063/1.58237, URL http://dx.doi.org/10.1063/1.58237.

[31] H. Metcalf und P. van der Straten, *Laser Cooling and Trapping*, Journal of the Optical Society of America B, **20** (2003). URL http://dx.doi.org/10.1364/JOSAB.20.000887.

[32] M. L. Citron, H. R. Gray, C. W. Gabel und C. R. Stroud, *Experimental study of power broadening in a two-level atom*, Phys. Rev. A, **16**, 1507 (1977). URL http://dx.doi.org/10.1103/PhysRevA.16.1507.

[33] V. Letokhov und V. Minogin, *Laser radiation pressure on free atoms*, Physics Reports, **73**(1), 1 (1981). URL http://dx.doi.org/https://doi.org/10.1016/0370-1573(81)90116-2.

[34] *Chapter 6: Interaction of Light and Matter* , https://ocw.mit.edu/courses/electrical-engineering-and-computer-science/6-974-fundamentals-of-photonics-quantum-electronics-spring-2006/lecture-notes/. Called up on 17/12/2019.

[35] A. P. Thorne, U. Litzen und S. Johansson, *Spectrophysics : principles and applications* (1999).

[36] S. Chu, L. Hollberg, J. E. Bjorkholm, A. Cable und A. Ashkin, *Three-dimensional viscous confinement and cooling of atoms by resonance radiation pressure*, Phys. Rev. Lett., **55**, 48 (1985). URL `http://dx.doi.org/10.1103/PhysRevLett.55.48`.

[37] P. D. Lett, W. D. Phillips, S. L. Rolston, C. E. Tanner, R. N. Watts und C. I. Westbrook, *Optical molasses*, J. Opt. Soc. Am. B, **6**(11), 2084 (1989). URL `http://dx.doi.org/10.1364/JOSAB.6.002084`.

[38] V. I. Balykin, V. G. Minogin und V. S. Letokhov, *Electromagnetic trapping of cold atoms*, Reports on Progress in Physics, **63**(9), 1429 (2000). URL `http://dx.doi.org/10.1088/0034-4885/63/9/202`.

[39] E. L. Raab, M. Prentiss, A. Cable, S. Chu und D. E. Pritchard, *Trapping of Neutral Sodium Atoms with Radiation Pressure*, Phys. Rev. Lett., **59**, 2631 (1987). URL `http://dx.doi.org/10.1103/PhysRevLett.59.2631`.

[40] B. Jagatap, A. Marathe, K. Manohar, R. Sethi und s. Ahmad, *Neutral Atom Traps for Bose-Einstein Condensation*, S. 299–316 (2000), ISBN 978-1-4613-6912-7. URL `http://dx.doi.org/10.1007/978-1-4615-4259-9_18`.

[41] T. H. Loftus, T. Ido, M. M. Boyd, A. D. Ludlow und J. Ye, *Narrow line cooling and momentum-space crystals*, Physical Review A, **70**(6) (2004). URL `http://dx.doi.org/10.1103/physreva.70.063413`.

[42] A. Frisch, K. Aikawa, M. Mark, A. Rietzler, J. Schindler, E. Zupanič , R. Grimm und F. Ferlaino, *Narrow-line magneto-optical trap for erbium*, Physical Review A, **85**(5) (2012). URL `http://dx.doi.org/10.1103/physreva.85.051401`.

[43] W. Lunden, L. Du, M. Cantara, P. Barral, A. O. Jamison und W. Ketterle, *Enhancing the capture velocity of a Dy magneto-optical trap with two-stage slowing*, Physical Review A, **101**(6) (2020). URL `http://dx.doi.org/10.1103/physreva.101.063403`.

[44] W. D. Phillips und H. Metcalf, *Laser Deceleration of an Atomic Beam*, Phys. Rev. Lett., **48**, 596 (1982). URL `http://dx.doi.org/10.1103/PhysRevLett.48.596`.

[45] T. E. BARRETT, S. W. DAPORE-SCHWARTZ, M. D. RAY UND G. P. LAFY-ATIS, *Slowing atoms with σ^- polarized light*, Phys. Rev. Lett., **67**, 3483 (1991). URL `http://dx.doi.org/10.1103/PhysRevLett.67.3483`.

[46] D. B. ALI, T. BADR, T. BRÉZILLON, R. DUBESSY, H. PERRIN UND A. PERRIN, *Detailed study of a transverse field Zeeman slower*, Journal of Physics B: Atomic, Molecular and Optical Physics, **50**(5), 055008 (2017). URL `http://dx.doi.org/10.1088/1361-6455/aa5a6a`.

[47] X. YU, J. MO, T. LU, T. Y. TAN UND T. L. NICHOLSON, *Zeeman slowing of a group-III atom*, Physical Review Research, **4**(1) (2022). URL `http://dx.doi.org/10.1103/physrevresearch.4.013238`.

[48] C. J. DEDMAN, J. NES, T. M. HANNA, R. G. DALL, K. G. H. BALD-WIN UND A. G. TRUSCOTT, *Optimum design and construction of a Zeeman slower for use with a magneto-optic trap*, Review of Scientific Instruments, **75**(12), 5136 (2004). `https://pubs.aip.org/aip/rsi/article-pdf/75/12/5136/11153162/5136_1_online.pdf`, URL `http://dx.doi.org/10.1063/1.1820524`.

[49] B. F. HOCHREITER, *Optimisation of a spin-flip Zeeman slower and laser locking to a broad spectral line* (2020).

[50] P. ILZHÖFER, *Creation of Dipolar Mixtures of Erbium and Dysprosium*, Dissertation (2020).

[51] E. D. BLACK, *An introduction to Pound–Drever–Hall laser frequency stabilization*, American Journal of Physics, **69**(1), 79 (2001). `https://pubs.aip.org/aapt/ajp/article-pdf/69/1/79/10115998/79_1_online.pdf`, URL `http://dx.doi.org/10.1119/1.1286663`.

[52] J. OLIVERO UND R. LONGBOTHUM, *Empirical fits to the Voigt line width: A brief review*, Journal of Quantitative Spectroscopy and Radiative Transfer, **17**(2), 233 (1977). URL `http://dx.doi.org/https://doi.org/10.1016/0022-4073(77)90161-3`.

[53] N. B. VILAS, *Laser Cooling Towards a Dipolar Quantum Gas of Erbium Atoms* (2018).

[54] M. J. MARK, *Calculation of the magnetic field resulting from the currents running through the magnetic field coils of the ZS*. Code kindly provided by Manfred.

[55] M. J. MARK, *Calculation of the eta paramter*. Code kindly provided by Manfred.

[56] M. J. MARK, *Simulation of the deceleration of an atom in the Zeeman slower in dependence on the initial velocity.* Code kindly provided by Manfred.

[57] J. J. BALMER, *Notiz über die Spectrallinien des Wasserstoffs*, Annalen der Physik, **261**(5), 80 (1885). https://onlinelibrary.wiley.com/doi/pdf/10.1002/andp.18852610506, URL http://dx.doi.org/https://doi.org/10.1002/andp.18852610506.

[58] N. BOHR, *I. On the constitution of atoms and molecules*, The London, Edinburgh, and Dublin Philosophical Magazine and Journal of Science, **26**(151), 1 (1913). https://doi.org/10.1080/14786441308634955, URL http://dx.doi.org/10.1080/14786441308634955.

[59] J. RYDBERG, *Recherches sur la constitution des spectres d'émission des éléments chimiques*, Bd. Band 23 No 11 von *Kungliga vetenskapsakademiens handlingar*, Kungliga Vetenskapsakademien (1890).

[60] M. J. SEATON, *Quantum defect theory*, Reports on Progress in Physics, **46**(2), 167 (1983). URL http://dx.doi.org/10.1088/0034-4885/46/2/002.

[61] C. S. ADAMS, J. D. PRITCHARD UND J. P. SHAFFER, *Rydberg atom quantum technologies*, Journal of Physics B: Atomic, Molecular and Optical Physics, **53**(1), 012002 (2019). URL http://dx.doi.org/10.1088/1361-6455/ab52ef.

[62] M. SAFFMAN, T. G. WALKER UND K. MØLMER, *Quantum information with Rydberg atoms*, Rev. Mod. Phys., **82**, 2313 (2010). URL http://dx.doi.org/10.1103/RevModPhys.82.2313.

[63] N. ŠIBALIĆ UND C. S. ADAMS, *Rydberg Physics*, in *Rydberg Physics*, 2399-2891, S. 1–1 to 1–27, IOP Publishing (2018), ISBN 978-0-7503-1635-4. URL http://dx.doi.org/10.1088/978-0-7503-1635-4ch1.

[64] A. BROWAEYS, A. GAËTAN, T. WILK ET AL., *ENTANGLEMENT OF TWO INDIVIDUAL ATOMS USING THE RYDBERG BLOCKADE*, S. 63–73. https://www.worldscientific.com/doi/pdf/10.1142/9789814282345_0006, URL http://dx.doi.org/10.1142/9789814282345_0006.

[65] H. WEIMER, M. MÜLLER, I. LESANOVSKY, P. ZOLLER UND H. P. BÜCHLER, *A Rydberg quantum simulator*, Nature Physics, **6**(5), 382 (2010). URL http://dx.doi.org/10.1038/nphys1614.

[66] A. TRAUTMANN, M. MARK, P. ILZHÖFER, H. EDRI, A. EL ARRACH, J. MALOBERTI, C. GREENE, F. ROBICHEAUX UND F. FERLAINO, *Spectroscopy of Rydberg states in erbium using electromagnetically induced trans-*

parency, Physical Review Research, **3** (2021). URL `http://dx.doi.org/10.1103/PhysRevResearch.3.033165`.

[67] S. QUANTUM GASSES GROUP, *A Laboratory Control System for Cold Atom Experiments*, http://strontiumbec.com/. Called up on 10/11/2021.

Spectroscopy of Rydberg states in erbium using electromagnetically induced transparency

A. Trautmann ®,[1] M. J. Mark ®,[1,2] P. Ilzhöfer,[1,*] H. Edri,[1] A. El Arrach ®,[1] J. G. Maloberti,[1]
C. H. Greene ®,[3,4] F. Robicheaux ®,[3,4] and F. Ferlaino ®[1,2]

[1]*Institut für Quantenoptik und Quanteninformation, Österreichische Akademie der Wissenschaften,*
Technikerstraße 21a, 6020 Innsbruck, Austria
[2]*Institut für Experimentalphysik, Universität Innsbruck, Technikerstraße 25, 6020 Innsbruck, Austria*
[3]*Department of Physics and Astronomy, Purdue University, West Lafayette, Indiana 47907, USA*
[4]*Purdue Quantum Science and Engineering Institute, Purdue University, West Lafayette, Indiana 47907, USA*

We present a study of the Rydberg spectrum in ^{166}Er for series connected to the $4f^{12}(^3H_6)6s$, $J_c = 13/2$, and $J_c = 11/2$ ionic core states using an all-optical detection based on electromagnetically induced transparency in an effusive atomic beam. Identifying approximately 550 individual states, we find good agreement with a multichannel quantum defect theory (MQDT) which allows assignment of most states to ns or nd Rydberg series. We provide an improved accuracy for the lowest two ionization thresholds to $E_{\mathrm{IP},J_c=13/2} = 49260.750(1)$ cm^{-1} and $E_{\mathrm{IP},J_c=11/2} = 49701.184(1)$ cm^{-1} as well as the corresponding quantum defects for all observed series. We identify Rydberg states in five different isotopes, and states between the two lowest ionization thresholds. Our results open the way for future applications of Rydberg states for quantum simulation using erbium and exploiting its special open-shell structure.

I. INTRODUCTION

Rydberg states in neutral atoms have been highly successful in realizing strongly interacting many-body quantum platforms. The large dipole-dipole (van der Waals) interaction, typically exceeding the MHz scale, enables unique paths for quantum information processing and many-body quantum simulations [1–3]. The conditions of strong interaction, long internal-state coherence, and microscopic control can now be satisfied simultaneously when driving Rydberg (Ry) excitations in tweezer-trapped neutral atoms [4]. This important advance was initially developed with alkaline atoms [5–8]. Due to their relatively sparse atomic structure, alkali are well suited for the implementation of robust, yet simple, cooling and trapping methods. However, this simplicity comes at the cost of somehow restricted opportunities for state preparation and manipulation of the available internal degrees of freedom.

Recently, there has been growing interest in extending the Rydberg toolbox to more complex multi-valence-electron atomic species, opening possibilities for, e.g., laser cooling and trapping, high-fidelity optical read-out, and quantum-information storage [9–12]. In multi-valence-electron atoms,

the key paradigm shift is that, after Ry excitation of one of the available valence electrons, the core remains optically active, effectively resembling a single-charged positive ion. This active core leads, for instance, to a comparatively large polarizability [11], allowing for optical trapping despite the repulsive ponderomotive potential for the Ry electron [13]. Remarkable progress has been made with two-electron atoms, i.e., the alkaline-earth Sr [14–17] and the alkaline-earth-like Yb atoms [18], for ground-state tweezer trapping [19–21], and, more recently, the combination of tweezer trapping and Ry excitation [13,22].

Pushing the boundaries even further, the next step is to consider atomic species with more than two valence electrons, like open-shell lanthanides for which laser cooling and quantum degeneracy have been demonstrated [23–27]. Compared to alkaline earth, these species might exhibit an ionic-core polarizability resembling even more the ground-state polarizability, and might allow access to a large hyperfine manifold [9,12]. Besides the plethora of laser cooling transitions, they could also allow direct access to high orbital-momentum Ry states with negligible quantum defects, which are expected to have strong pair interactions because of the multitude of nearby degenerate quantum states. However, being a comparatively new quantum resource, open-shell Ry lanthanides remain rather unexplored in the ultracold regime.

So far, the only reported high-resolution Ry spectroscopy in ultracold open-shell lanthanides has been performed with holmium in a magneto-optical trap (MOT) [28]. For Dy and Pm, resonance ionization spectroscopy (RIS) has been performed on a hot atomic vapor [29–31]. Using RIS, preliminary data for erbium are also available [32].

The present paper reports on the first high-resolution Ry spectroscopy of erbium atoms. Using a two-photon scheme
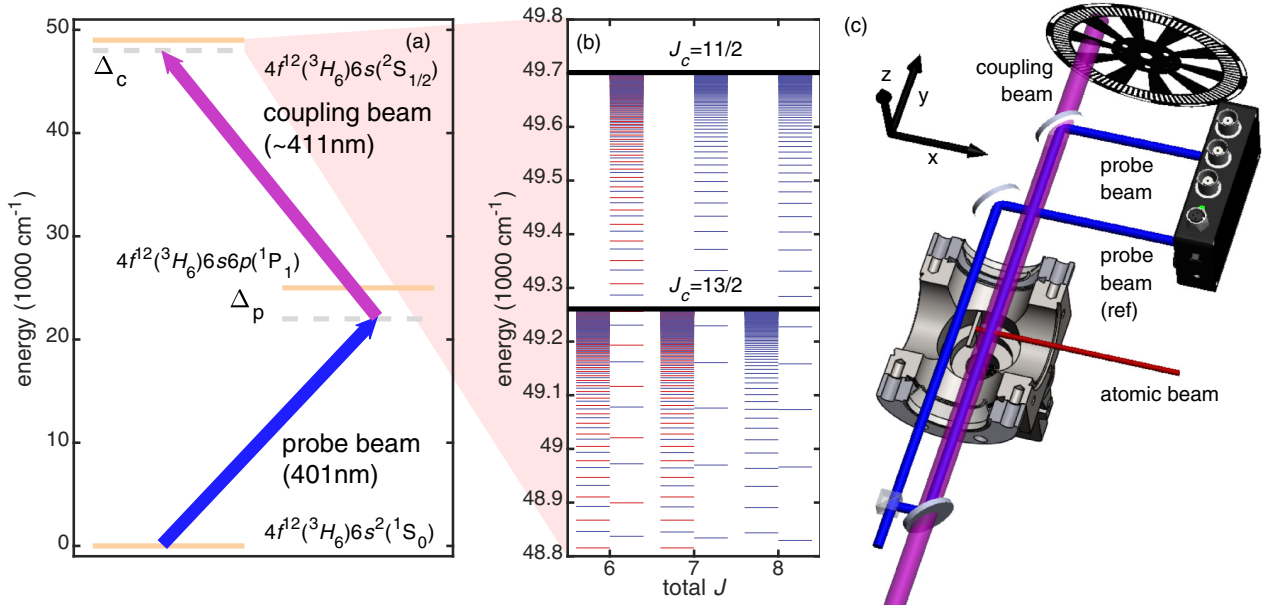
FIG. 1. Electronic levels and experimental setup. (a) Excitation scheme involving the probe transition at about 401 nm with single photon detuning Δ_p and the coupling transition around 411 nm. Also shown, the two-photon detuning Δ_c. (b) Schematic Rydberg level scheme of the two lowest ionization thresholds for different total J. Red (blue) lines indicate the ns (nd) series. (c) Schematic drawing of the experimental setup with the vacuum apparatus, atomic beam, and probe, reference, and couple laser beams.

based on electromagnetically induced transparency (EIT) [33–36], we observe the ns and nd Rydberg series with principal quantum number n ranging from 15 up to 140. Using slope minimizing fits in Lu-Fano style plots [37], we provide an improved value of the first ionization potential. Our method does not require the magnetic quadrupole field present in a MOT, and thus allows an effortless high-resolution study of Zeeman shifts of the Rydberg states. We use these shifts to assign the total angular momentum, J, of a subset of Ry ns and nd states, which serves as an important input parameter for the modeling of the Rydberg series.

Moreover, we identify characteristics of the Rydberg states using procedures based on multichannel quantum defect theory (MQDT), similar to recent work on Sr [38] but accounting for Rydberg perturbers from a spin-orbit split threshold. Using the approximation that the ns and nd states do not mix at all, we successfully perform a MQDT fit to the ns series. For the nd series, we introduce two different approximate methods which are fairly successful in representing most of the states but are less precise in representing the nd perturbers or the measured g factors.

Finally, we surprisingly observe that using just a two-photon transition we could presumably couple ground-state atoms to an ng Ry state ($\Delta\ell = 4$) thanks to the interaction between the submerged shells in Lanthanides. This result provides a first example of the uniqueness of Ry lanthanide with respect to alkali and alkaline-earth atoms.

The paper is structured in the following way: Section II discusses the energy levels and coupling schemes of erbium with all relevant states for this paper. The experimental setup and measurement techniques are reviewed in Sec. III. In Sec. IV, we will discuss the experimental data by demonstrating the EIT signal and present the determination of J and g_J for a

set of nd states as well as an accurate value for the ionization threshold. Section V presents our MQDT results for both ns and nd series and will compare the results with our experimental results.

II. CONSIDERATIONS ON THE ERBIUM LEVEL STRUCTURE

Figure 1(a) shows the excitation scheme used in this paper and Fig. 1(b) a zoom-in on the most relevant Rydberg series attached to the lowest two ionization thresholds. The electronic ground-state configuration of erbium reads $[4f^{12}(^3H_6)6s^2(^1S_0)]_6$. This type of configuration is often called submerged because the partially filled inner f shell is surrounded by the outer s shell. Erbium has a total of 14 valence electrons and each of those can be excited to a higher-lying state. The interactions inside the submerged shell determines the type of angular momentum coupling of the state. Generally speaking, the spin-orbit coupling scheme depends on the specific configuration and on the energy of the state—i.e., overlap between the submerged wave functions.

For our two-photon Rydberg spectroscopy, we couple the ground state to the intermediate state $[4f^{12}(^3H_6)6s6p(^1P_1)]_7$. Here, the angular momentum coupling results from the small size of the $4f$ orbital compared to that of the sp electrons. This leads to the $4f^{12}$ electrons coupling together to give a particular angular momentum term, $(^3H_6)$, and the sp electrons coupling to give $(^1P_1)$. These two partial J's are then coupled to give the total $J = 7$ for the intermediate state. A similar argument holds for the ground and first excited state of the ion $[4f^{12}(^3H_6)6s(^2S_{1/2})]_{J_c}$ with $J_c = 13/2$ for the ground ionic state and $J_c = 11/2$ for the first excited state. For the Rydberg states, the energy scale of the Rydberg electron is

TABLE I. Quantum numbers of all relevant states for the EIT scheme, with the total ground state, intermediate state, and ion core states with Rydberg series attached. The table lists the configuration, state energy, as well as total angular momentum J. For Rydberg states, the core total angular momentum J_c is also given. Only states with $|\Delta J| \leqslant 1$ with respect to the intermediate state ($J_{ex} = 7$) are shown as our two-photon scheme only couples to such states.

Configuration	Term, J	Energy (cm^{-1}) (threshold)
$4f^{12}(^3H_6)6s^2(^1S_0)$	(6,0) 6	0
$4f^{12}(^3H_6)6s6p(^1P_1)$	(6,1) 7	24943.298
$4f^{12}(^3H_6)6s_{1/2}$	(6,1/2) 13/2	49260.750
$4f^{12}(^3H_6)6s_{1/2}$	(6,1/2) 11/2	49701.184
$4f^{12}(^3H_6)6s_{1/2}ns_{1/2}$	(13/2,1/2)6,7	($J_c = 13/2$)
$4f^{12}(^3H_6)6s_{1/2}ns_{1/2}$	(11/2,1/2)6	($J_c = 11/2$)
$4f^{12}(^3H_6)6s_{1/2}nd_{3/2}$	(13/2,3/2)6,7,8	($J_c = 13/2$)
$4f^{12}(^3H_6)6s_{1/2}nd_{5/2}$	(13/2,5/2)6,7,8	($J_c = 13/2$)
$4f^{12}(^3H_6)6s_{1/2}nd_{3/2}$	(11/2,3/2)6,7	($J_c = 11/2$)
$4f^{12}(^3H_6)6s_{1/2}nd_{5/2}$	(11/2,5/2)6,7,8	($J_c = 11/2$)

the smallest, suggesting the angular momentum of the positive ion should be coupled to that of the Rydberg electron. There are three ways to order the addition of angular momenta but the interaction between the Rydberg states will typically preclude the states from being nearly pure in one ordering or the other. The order used in the MQDT simulations is to add the spin and orbital angular momenta of the Rydberg electron together to get the total angular momentum, j, of the Rydberg electron; this is then added to the total angular momentum of the core electrons to get the total angular momentum of the final state. Our two-photon excitation scheme leads to even parity Rydberg states with most of the states having ns or nd character. Also, Lanthanides offer the unique possibility to directly couple to ng states with $\ell = 4$ due to the angular momentum of the submerged shell. Table I lists the relevant quantum numbers for the states discussed in this paper.

III. EXPERIMENTAL SETUP

Figure 1(c) shows a schematic drawing of the experimental spectroscopy setup, consisting of an ultrahigh vacuum setup with a high-temperature effusion cell, a transversal cooling chamber, a differential pumping section (not shown here), and the probe chamber. The design is similar to the one in Ref. [39]. Erbium atoms are evaporated in the effusion cell at 1300 °C. From the effusion cell, the atoms pass through three apertures to form a collimated beam, propagating along the horizontal x direction. In the subsequent probe chamber, the atomic beam crosses the interaction region with the coupling and probe laser beam. The coupling and probe beam counterpropagate and intersect the atomic beam perpendicular (y direction) to reduce Doppler shifts. They are overlapped and separated by dichroic mirrors. An additional reference beam, split from the probe beam, propagates parallel to the probe beam and acts as a reference to cancel out power fluctuations. We can block the atomic beam between the probe and reference beam to provide a reference with and without the atomic absorption. We use about 10 to 500 μW, with a waist ($1/e^2$

radius) of about 0.5 mm for both the probe and reference beam, while the coupling beam approximately has 130 mW at the interaction region and a waist of 1 mm. We modulate the coupling beam with an optical chopper at 7 kHz, monitor both the probe and reference beam on balanced photodiodes (PD1 and PD2), and feed the ac-coupled difference of these signals as input for a lock-in amplifier. Both lasers are commercial resonantly frequency-doubled devices; the probe and reference beam are derived from an amplified diode laser locked onto the 401 nm transition line using a Doppler-free modulation transfer spectroscopy in a hollow cathode lamp [25]. The coupling laser is derived from a continuous-wave free-running Ti:Sa laser. Both lasers are monitored on a wavelength meter with 60 MHz absolute accuracy, see Appendix C.

We add quarter- and half-wave plates to the probe and coupling beam path to control the light polarization, and apply a magnetic field on the order of 10 G in the z ($B = (0, 0, B_z)$) direction. This enables us to drive $\sigma^{\pm}$ and/or π transitions in a controlled setting, which facilitates the assignment of the total angular momentum J and estimation of the g factor of Rydberg states, see Sec. IV B.

IV. DATA ANALYSIS

To detect the Rydberg levels, we make use of EIT [33]. In short, we detect the probe laser transmission through the atomic beam, which experiences absorption when in resonance with the atomic transition to the intermediate state. In case the coupling laser hits a resonance condition, i.e., couples the intermediate state to a Rydberg state, this absorption gets reduced. This can be understood in a dressed state picture where the coupling leads to a doublet of dressed states (Autler–Townes doublet) [40] and, together with destructive interference of the absorption of these states, to a transparency window at resonance. This tell-tale sign of EIT is shown in Fig. 2(a), where we directly record the probe laser power after passing the atomic beam. The probe laser frequency is scanned over the absorption resonance, while the coupling laser frequency is fixed, in this case on resonance to the Rydberg state at 49147.967 cm^{-1}, identified as the lowest-lying fine-structure state of the 31d Rydberg manifold, see later discussion. The narrow transmission peak due to EIT appears in the center of the absorption line.

For a survey of Rydberg states, we lock the probe laser onto the hollow-cathode lamp spectroscopy on resonance with the 401 nm transition to the intermediate state, scan the coupling laser frequency, and again record the transmitted probe laser power. We additionally improve our signal-to-noise ratio by using a reference beam, which we subtract to reduce noise from power fluctuations, and using a lock-in technique where we modulate the coupling beam with a chopper, see Sec. II for details. In case we hit the resonance condition to a Rydberg state, we observe directly the increased transmission. Figure 2(b) shows an excerpt of the total spectroscopy data in the region from about 49112 cm^{-1} to 49211 cm^{-1}.

Using this technique, we record about 550 EIT resonances and assign their total energy, see Appendix D for a full list. After the determination of the ionization thresholds (see details in Sec. IV A) we can assign effective quantum numbers to each level. Figure 2(c) shows the energy of all
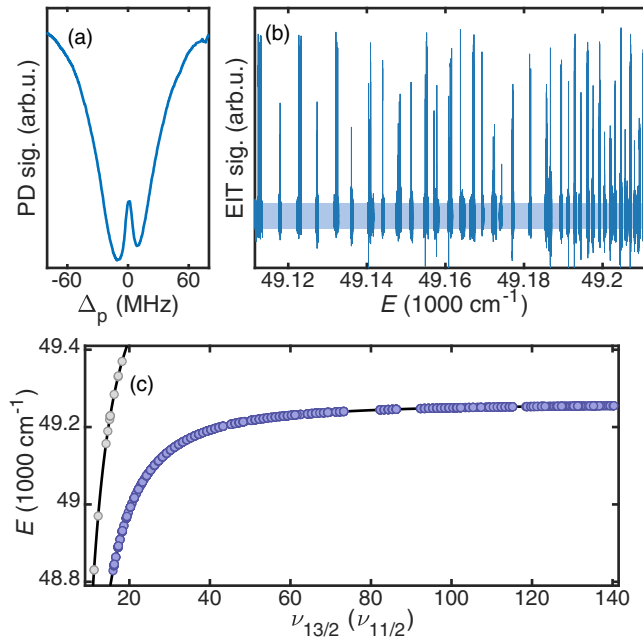
FIG. 2. EIT spectroscopy and survey of Rydberg states. (a) Exemplary EIT resonance around 49147.967 cm^{-1}. Here, the coupling beam is kept fixed while Δ_p is scanned, showing the typical EIT signal of reduced absorption when on two-photon resonances. (b) EIT spectroscopy over a broad range of energies covering about 100 individual Rydberg states. Δ_p is fixed to zero while the coupling laser frequency is scanned. The shaded area indicates the noise floor as a guide to the eye. (c) Energy of all observed Rydberg states extracted from the data as a function of the assigned effective principle quantum number. Ry states that are either above the first ionization threshold or comparatively broad are assigned to the second-lowest $J_c = 11/2$ ionization threshold and are plotted against their corresponding principle quantum number (grey). Solid lines show the expected Rydberg energies using the simple Rydberg formula with the derived $E_{\mathrm{ion},j}$.

A. Determination of lowest ionization threshold and assignment of series

As an important parameter for the assignment of quantum numbers and the understanding of the Rydberg series, we first determine the lowest ionization threshold by plotting the effective quantum numbers $\nu_j = \sqrt{R_\mu/(E_{\mathrm{ion},j} - E_i)}$ and effective quantum defects $\mu_j = -\nu_j (\mathrm{mod}\ 1)$. Here, ν_j is the effective quantum number with respect to the ion core state with angular momentum j, $E_{\mathrm{ion},j}$ the corresponding ionization threshold, and E_i the energy of the Rydberg states. We also
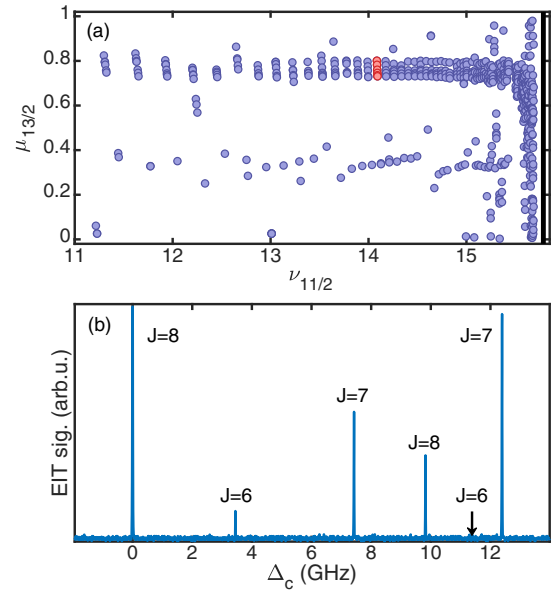
FIG. 3. Rydberg series: (a) Lu-Fano-style plot, showing the calculated $\mu_{13/2}$ of all observed states below the lowest ionization threshold as a function of the effective quantum number $\nu_{11/2}$ of the second-lowest ionization threshold. (b) Zoom into the EIT spectrum around 49148 cm^{-1}, showing the states marked as red data points in (a). This bundle of resonances is identified as the 31d Ry state where the fine structure splitting leads to six features with $J = 6, 7$, or 8, see Sec. IV B for the assignment.

use $n_{\mathrm{eff}} = \mathrm{floor}(\nu_j)$ as the integer part for the assignment. We use a Lu-Fano analysis of our data to extract a new value for the ionization threshold: For an unperturbed Rydberg series, the quantum defect is nearly constant for intermediate principle quantum numbers. For Rydberg states with very high principle quantum numbers close to the ionization threshold, external influences like electric fields can disturb the states, and uncertainties in absolute frequencies have a larger influence on the effective quantum defect, while at lower energies the quantum defect shows a stronger state dependence. By plotting the calculated effective quantum defect $\mu_{13/2}$ versus $\nu_{11/2}$, we obtain a manifold of flat series around $\mu_{13/2} = 0.8$. We vary the value for the ionization threshold and fit a straight line to all states with $0.7 < \mu_{13/2} < 0.9$ above 49250 cm^{-1} and find $E_{\mathrm{ion},13/2} = 49260.7442(23)$ cm^{-1} as a value for the lowest ionization threshold to minimize the overall slope. This value is within the error margin of the literature value of 49262(8) cm^{-1} [41] and of the preliminary value 49260.73(9) cm^{-1} derived in Ref. [32], but improves in precision by almost four, or two, respectively, orders of magnitude. For the first excited ionization threshold, the same analysis suffers from the low number of states and missing states at high $\nu_{11/2}$. Therefore, we use the value reported in Refs. [42,43] for the splitting of the two states with 440.433(10) cm^{-1} and calculate the $E_{\mathrm{ion},11/2} = 49701.177(10)$ cm^{-1}.

Figure 3(a) shows the resulting effective quantum number and quantum defect for all states below the first ionization threshold. Two main series are visible, the first one around $\mu_{13/2} = 0.35$ which consists of single separated states,

observed Rydberg states as a function of their effective quantum numbers. We observe the typical $1/n^2$ scaling of Rydberg states. We also found several very strong EIT features, at least ten times stronger than any surrounding resonances. Together with a few states located above the first ionization threshold, we assign them to be part of the Rydberg series attached to the second-lowest $J_c = 11/2$ ionization threshold. Also, here we observe a similar $1/n^2$ scaling which, together with their positions agreeing with the expected locations of states from this threshold, further strengthens our assignment.

FIG. 4. Zeeman mapping of the $27d$ fine structure multiplet. Blue thick lines show the photo diode signal of multiple averaged experimental data traces scanning the couple laser frequency. Red thin lines show the estimated spectral pattern using the fitted g factors.

expected for the ns series. At the second series around $\mu_{13/2} = 0.75$, we observe a bundle of five to six lines in relatively close proximity to each other. This is consistent with the expected nd series. Figure 3(b) shows an exemplary scan over one of those bundles and already gives the assignment of the individual J values, as we will detail below.

B. Determination of total angular momentum J and g factors

While the ns states are clearly separated and are expected to be nearly exclusively $J = 6$ (see Sec. V for a more detailed discussion), there is a large number of possible nd states. A full assignment of the nd states requires a determination of their total angular momentum, J, which we extract by performing a Zeeman spectroscopy for each state of the fine structure manifold for principal quantum numbers $n_{\mathrm{eff}} = 23, 27, 31, 37$: We apply a magnetic field along z, and use horizontal polarization for all laser beams (propagating along y, polarization parallel to x), which provides σ^+ and σ^- light in the reference frame of the atoms. We first calibrate our magnetic field with a Zeeman spectroscopy of the transition to the intermediate state without probe light by scanning the 401 nm laser and fitting Gaussian curves to the absorption signal. With the known g factors for both ground and intermediate states, we determine our magnetic field strength to be 10.7(5) G.

Now we lock the probe beam frequency again on the zero-field resonance, scan the couple laser frequency over a range of about 100 MHz, and observe a splitting of the EIT lines, which results in distinctly different signal patterns, see exemplary the patterns of the $27d$ fine-structure manifold shown in Fig. 4. We can sort the patterns into three groups: (A) One weak central peak and two strong peaks shifted sym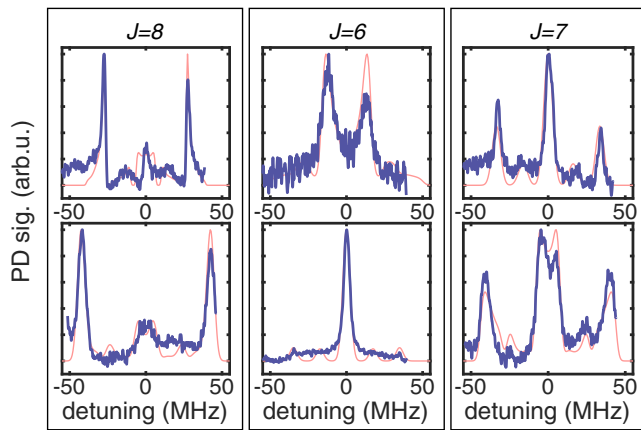metrically by about 40 MHz, (B) one central peak which may split into two peaks separated by less than 30 MHz, and (C) a strong central peak with two or four weaker side peaks. Note that the asymmetry in the spectra is an artifact from the measurement procedure which we were not able to remove completely.

These three distinct behaviors can be explained as the result of the combination of the specific J in the ground (J_{gs}), excited (J_{ex}), and Rydberg states and the polarization of the probe

and coupling beam. In general, the resonance frequency of a specific two-photon transition $|J_{\mathrm{gs}}, m_{\mathrm{gs}}\rangle \rightarrow |J, m_J\rangle$ shifts from its zero-field energy as $\Delta E = (g_J m_J - g_{\mathrm{gs}} m_{\mathrm{gs}})\mu_B B$. Here, m_{gs} (m_J) denotes the projection of J_{gs} (J) of the ground-state (Rydberg) atom along the quantization axis and $\Delta m = m_J - m_{\mathrm{gs}}$ the total difference between them. As transitions are limited to $|\Delta m| \leqslant 2$ due to selection rules and assuming that g_J is close to g_{gs}, we can identify five main features with energies:

$$\Delta E_{\pm 2} = \pm 2 g_{\mathrm{gs}} \mu_B B, \quad (\Delta m = \pm 2),$$
$$\Delta E_{\pm 1} = \pm 1 g_{\mathrm{gs}} \mu_B B, \quad (\Delta m = \pm 1),$$
$$\Delta E_0 = 0, \quad (\Delta m_J = 0).$$

Taking into account the additional difference in g factors, each of these main resonances splits again into a series of closely spaced resonances with additional energy shifts $\Delta E = \Delta g_J m_J \mu_B B$, with $\Delta g_J = g_J - g_{\mathrm{gs}}$.

Given our applied polarization of probe and coupling beam ($\sigma^\pm$) and partial optical pumping toward the stretched states $J_{\mathrm{gs}} = \pm 6$ during the spectroscopy due to the different Clebsch-Gordan coefficients of the first transition, we expect mainly resonances at $\Delta E_{\pm 2}$ and ΔE_0, see Appendix B for further details and corresponding calculations. Based on these modeled spectral patterns, for $J = 8$ we expect the strongest signals at $\Delta E_{\pm 2}$ and a weaker central peak at ΔE_0. Instead, for $J = 6$, the strongest resonance will be ΔE_0, which might split for large Δg_J, while $\Delta E_{\pm 2}$ transitions will be very weak. Finally, $J = 7$ will have its strongest component at ΔE_0 together with slightly weaker $\Delta E_{\pm 2}$ transitions and some very weak $\Delta E_{\pm 1}$ components. With these considerations, we assign group (A) to $J = 8$, group (B) to $J = 6$, and group (C) to $J = 7$.

Using this assignment technique for all investigated principal quantum numbers $n_{\mathrm{eff}} = 23, 27, 31, 37$ [44], we observe the same fine-structure pattern with increasing energy, which goes as $J = 8, 6, 7, 8, 6, 7$, see Fig. 3(b). Additionally, we find that the $J = 6$ EIT resonances within one scan are significantly weaker compared to $J = 7, 8$. The same pattern in relative signal strength can be found for five other $n_{\mathrm{eff}} = 32 - 36$, allowing us to assign the total J of each state via comparison of the order and relative height of the resonances of the EIT spectra without the need of a full Zeeman mapping for every n_{eff}.

We are also able to experimentally determine the g_J value for most of the investigated states. For this, we fit our modeled spectral pattern (see Appendix B) to the experimental data, with g_J as the main fitting parameter. We also allow some variation of the polarization and the optical pumping effect to be able to account for differences in the experimental conditions like probe and coupling laser intensities and beam alignment. Our results are summarized in Table IV.

V. MQDT, ASSIGNMENT OF LINES, ASSIGNMENT OF QUANTUM DEFECTS

Most of the experimentally measured energies for $20 < \nu_{13/2} < 60$ seem to be grouped into two sets that are weakly interacting. The group with quantum defects $0.3 \lesssim \mu_{13/2} \lesssim 0.4$ appear to come from a two channel series with one channel attached to the 13/2 threshold and the other attached to

TABLE II. The MQDT parameters for the *ns* $J = 6$ series.

τ	τ_0	τ_2
μ_1	0.30136	-15.78
μ_2	0.42673	-1.718
α	0.72378	-0.594

the 11/2 threshold. From the discussion in Appendix A, this suggests that these are $J = 6$ states with *ns* Rydberg character. The other main group are states with quantum defects between $\sim$0.75 and $\sim$0.8 which, due to their number, must be states with *nd* Rydberg character. There are several states with small quantum defects which might have *ng* character. Finally, there are several states that are not part of either group but might be identified by fitting the MQDT parameters.

A. *ns* series

In the limit that coupling between *ns* and *nd* states can be ignored, the *ns* series with $J = 6$ results from a two-channel system with one channel attached to the $J_c = 13/2$ threshold and one attached to $J_c = 11/2$. Since the K matrix is symmetric there are only three independent parameters in the K matrix. We chose the parameters to be the two eigenquantum defects and the mixing angle of the eigenvector. Taking channel 1 to be $J_c = 13/2$ and 2 to be $J_c = 11/2$, the K matrix is written as

$$K_{ij} = \sum_a U_{ia} U_{ja} \tan(\pi \mu_a), \tag{1}$$

where $U_{11} = U_{22} = \cos(\alpha)$ and $U_{21} = -U_{12} = \sin(\alpha)$. The frame transformation approximation in Appendix A 3 implies $\alpha = \cos^{-1}(\sqrt{7/13}) = 0.7469$.

We fit the identified states using these three parameters. The fit minimized the χ^2 calculated from the sum of differences between the calculated and measured energies. When we take these parameters to be independent of energy, we find $\mu_1 = 0.27458$, $\mu_2 = 0.42223$, and $\alpha = 0.72885$. Note the closeness of α to the value expected from the frame transformation approximation which further supports this approximation for the *ns* series. The residuals of the $\mu_{13/2}$ are shown in Fig. 5(b) and for most of the states they are smaller than $\sim$0.01. This level of agreement is roughly what should be expected for states over such a large range of energy. For a more realistic fit, we included a linear energy dependence in all of the parameters. Historical precedence gives a subscript 2 to the linear energy dependence [because the linear energy dependence was originally written as $1/(n - \mu)^2$]. For a parameter τ, the energy dependence is written as

$$\tau(E) = \tau_0 + \eta(E) \, \tau_2, \tag{2}$$

where $\eta(E) = (E_{13/2} - E)/R_{166}$ and R_{166} is the Rydberg constant defined in Appendix A. The fit values are given in Table II. Note that the value for α is only $\sim$3% different from the frame transformation value. The comparison between the MQDT fit and measured bound state energies is shown in Fig. 5. Note that the residuals for all states are now much less than 0.01. The fit was useful in identifying states not obviously part of the series with quantum defects between $\sim$0.3
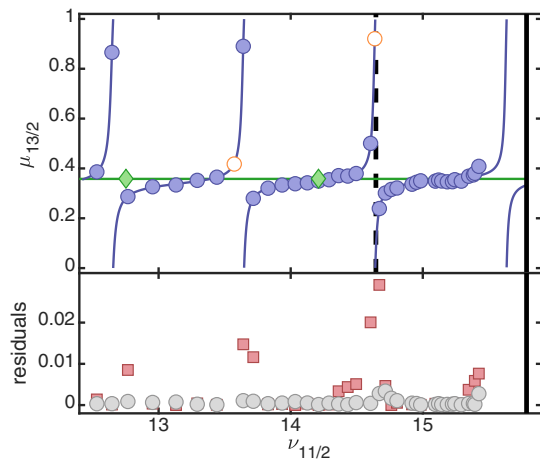
FIG. 5. Lu-Fano plot of the *s* series states. (a) All experimentally observed states assigned to the $J = 6$ (blue circles) and $J = 7$ (green diamonds) *s* series attached to the lowest 13/2 ionization threshold. The lines show the result of the MQDT calculations with energy dependence for the *ns* series; the black bar indicates the ionization threshold. The dashed line indicates a broad and strong EIT feature, assigned to the *ns* series of the 11/2 threshold. The open orange circles indicate theoretically predicted $J = 6$ states found experimentally in an additional survey. (b) Absolute values of the difference between the measured data and the MQDT model, with (grey circles) and without (red squares) energy dependence (see Sec. V A for details on the model).

to $\sim$0.4; these are the three states with quantum defects $\sim$0.9. The fit also predicted two states not in the original data set that were subsequently identified: 26*s* at 49105.45(7) cm^{-1} ($\mu_{13/2} \simeq 0.42$) and 39*s* at 49188.91(7) cm^{-1} ($\mu_{13/2} \sim 0.92$).

We observed only two states with quantum defects of $\mu = 0.358$ that do not appear to be members of the $J = 6$ series. We have assigned these to the $J = 7$ series. This small number of observed states compared to $J = 6$ might be explained by the different coupling of the two series. At short range, the *ns* $J = 7$ must have the coupling (6*sns*) $^3S_1$. Since the intermediate state has (6*snp*) $^1P_1$ character, transitions to the $J = 7$ would be dipole suppressed. But since both the intermediate state and the Rydberg state have finite admixtures of triplet and singlet character, respectively, excitations are allowed, where the excitation strength strongly depends on the singlet admixture of the specific Rydberg state. The large difference of this quantum defect from the μ_2 for $J = 6$ suggests limitations to the frame transformation because these values should both be the $^3S_1$ quantum defect, Appendix A 3.

B. *nd* series

The *nd* series is more difficult to model because of the larger number of channels and the limited number of experimentally identified states being perturbed, see Sec. IV B above. In total, the experimental data allowed to identify 12 states with $J = 6$, 18 states with $J = 7$, and 19 states with $J = 8$ character. These states were used in the fit of the parameters. Because the $J = 6$ and 7 have four channels and the $J = 8$ has three channels, there are ten free parameters for $J = 6$ and 7 and six free parameters for $J = 8$.

TABLE III. The MQDT parameters for the *nd* series for different *J*.

J	$\mu(^1D_2)$	$\mu(^3D_1)$	$\mu(^3D_2)$	$\mu(^3D_3)$
6	0.782	0.729	0.744	0.791
7	0.752	0.724	0.747	0.794
8	0.750		0.763	0.808

Symmetries in the bound-state conditions mean that the energies only determine eight parameters for $J = 6$ and 7 and five parameters for $J = 8$ (whenever two channels are attached to a threshold, the energies only determine the eigenquantum defects and cannot determine their mixing angle). The main difficulty in directly determining the full K matrix is that the $J_c = 13/2$ *nd* states experimentally identified to a particular J are not strongly perturbed by states attached to the $J_c = 11/2$ threshold. This means that the eigenquantum defects attached to the $J_c = 13/2$ threshold are well defined but most of the K-matrix elements are relatively unconstrained. As a contrast, see Fig. 5 where the perturbations of the *ns* states clearly lead to variations greater than 0.1 for $\mu_{13/2}$. This means the energies are giving information about two parameters for each J.

These considerations suggest using the frame transformation approximation or interaction approximation, discussed in Appendices A 3 and A 4, respectively, to reduce the number of fit parameters. These approximations lead to nearly the same χ^2 fit to the data points even though they have very different physical motivation. This is because they are mainly fitting to the eigenquantum defects of the channels attached to the $J_c = 13/2$ threshold. For these fits, we did not include energy dependence in the MQDT parameters because the resulting fits did not substantially improve the agreement with experimental results.

In addition to the measured energies, we were able to experimentally determine the *g* factor of several of the *nd* states. Appendix A 2 describes an approximate method for calculating *g* factors given the MQDT parameters. If the MQDT parameters were exact, this approximation would lead to errors less than 1%. Unfortunately, we did not find an effective way of using the measured *g* factors in the fitting procedure. The difference between the measured and simulated *g* factors described below results from the limitations of the frame transformation and interaction approximations used in the *nd* fits.

Figure 6 shows the experimental states where J has been identified, together with the calculated *nd* series using the frame transformation approximation. This plot emphasizes that the fit gives a fairly accurate representation of the experimentally detected states. Table III shows the fit parameters for the frame transformation approximation. The fact that the quantum defects mostly do not vary strongly with J (only the $^1D_2$ varies by more than 0.02) suggests that this approximation captures much of the physics of these series. However, this approximation is not accurate enough to predict the states that are perturbed or are attached to the $J_c = 11/2$ threshold, see Fig. 6. Also, the calculated *g* factors substantially differ from the measured values, see Table IV. Both difficulties suggest that the frame transformation does not capture the
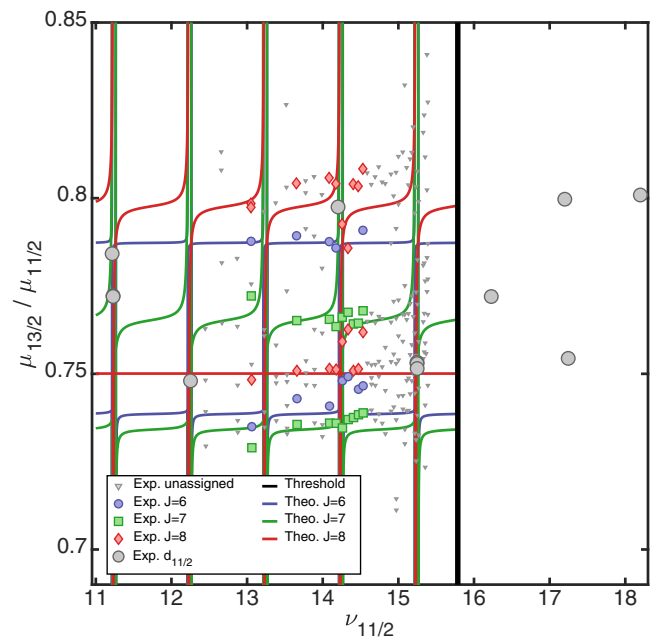
FIG. 6. MQDT assignment of *nd* Rydberg series. The lines show the results of the frame transformation approximation fitting. Small symbols show all experimental data, colored filled symbols show all states where we assigned J experimentally. Large grey circles (plotted with their respective $\mu_{11/2}$) represent states which we assign to the $J_c = 11/2$ threshold. Four of these are above the first threshold, while states for four different *n* are identified as perturbers of the *d* series attached to the $J_c = 13/2$ threshold.

full physics. The channel character is approximately 40:60 (or 60:40) of $nd_{3/2}$ and $nd_{5/2}$ for the frame transformation approximation. Thus, this approximation suggests the channels are strongly mixed. The fit to the interaction parameters, Appendix A 4, gives $C_q = 0.7533$, $\mu_{3/2} = -0.0777$, $\mu_6 = 0.7840$, $\mu_7 = 0.7690$, and $\mu_8 = 0.7979$. Since the experimental states are constraining six K-matrix parameters and there are five parameters in the fit, the fact that this model accurately reproduces the experimental values argues for the physics contained in the method. However, this approximation is also not accurate enough to predict the states that are perturbed or are attached to the $J_c = 11/2$ threshold, see Fig. 6. It does a better job of predicting the *g* factor but still has substantial inaccuracies, see Table IV. The channel character is nearly pure for this approximation. However, the state designation is reversed from that used to experimentally determine the *g* factor in Table IV. This contradicts the frame transformation characterization of the channel mixing which points to the uncertainty in the modeling of the *nd* series.

Note that while the two-threshold MQDT analysis appears to predict much of the general pattern of the Rydberg levels and perturbations at least qualitatively correctly, the energy range just below the $J_c = 13/2$ threshold looks irregular and even rather chaotic. To account for this apparent irregularity, it should be remembered that there are higher energy levels of Er^+ that are guaranteed to support their own infinite Rydberg series of levels as well. It is expected that some of the lower-lying members of those Rydberg series can also occur in the

TABLE IV. List of fine-structure states with Zeeman mapping and measured *g* factor, determined by energy splitting in a vertical magnetic field. For some states, the signal-to-noise ratio was too low to reliably fit the *g* factor (–). The calculated *g* factors are from the (frame transformation approximation, interaction fit). Note that the calculations only show a single state around 49056.9.

n_{eff}	E (cm^{-1})	J	$g_{J, \text{meas}}$	$g_{J, \text{diag}}$	$g_{J, \text{calc}}(FT, QP)$
23	49056.886(5)	8	–	–	(–,–)
23	49056.904(5)	8	1.21(2)	1.1493	(1.2205,1.2256)
23	49057.075(5)	6	1.34(3)	1.2454	(1.1597,1.2259)
23	49057.347(5)	7	1.17(4)	1.1877	(1.1491,1.2262)
23	49057.764(5)	8	–	1.2234	(1.1520,1.1471)
23	49057.997(5)	6	1.23(5)	1.2293	(1.3148,1.2488)
23	49058.102(5)	7	1.33(9)	1.2258	(1.2640,1.1873)
27	49112.369(5)	8	1.10(2)	1.1493	(1.2206,1.2256)
27	49112.531(5)	6	1.32(2)	1.2454	(1.1597,1.2259)
27	49112.794(5)	7	1.13(6)	1.1877	(1.1492,1.2262)
27	49112.949(5)	8	1.23(7)	1.2234	(1.1520,1.1471)
27	49113.035(5)	6	1.17(8)	1.2293	(1.3149,1.2488)
27	49113.115(5)	7	1.24(10)	1.2258	(1.2642,1.1873)
31	49147.967(5)	8	1.18(5)	1.1493	(1.2206,1.2256)
31	49148.098(5)	6	1.33(2)	1.2454	(1.1597,1.2259)
31	49148.258(5)	7	1.22(4)	1.1877	(1.1491,1.2262)
31	49148.359(5)	8	1.30(3)	1.2234	(1.1520,1.1471)
31	49148.435(5)	6	1.17(5)	1.2293	(1.3149,1.2488)
31	49148.470(5)	7	1.25(3)	1.2258	(1.2641,1.1873)
37	49181.406(5)	8	1.13(8)	1.1493	(1.2207,1.2256)
37	49181.480(5)	6	–	1.2454	(1.1597,1.2259)
37	49181.578(5)	7	1.12(10)	1.1877	(1.1492,1.2262)
37	49181.604(5)	8	1.23(2)	1.2234	(1.1520,1.1471)
37	49181.668(5)	6	–	1.2293	(1.3149,1.2488)
37	49181.701(5)	7	1.22(3)	1.2258	(1.2642,1.1873)

spectral region studied here, and those are expected to cause significant distortions of the experimental energy level pattern and associated deviations from the present MQDT models.

One ionic threshold, in particular, appears to lie at an energy poised to produce such a perturbation just below the even-parity ground state of the ion. We refer to the odd-parity level of Er$^+$ with the spectroscopic label $4f^{11}6s^2 \ ^4I^o_{15/2}$, which lies 6824.774 cm^{-1} above the $J_c = 13/2$ ionic ground state. A $5f$ Rydberg electron attached to that core, with an expected quantum defect of $\mu_f \approx 1$, should produce many Rydberg states of erbium lying approximately 34 cm^{-1} below the $J_c = 13/2$ ionization threshold, in the $\nu_{13/2} \approx 50 - 60$ range, and $\nu_{11/2} \approx 15.2$. Specifically, a $5f_{5/2}$ electron produces levels with all values of J from 5 to 10, and a $5f_{7/2}$ electron produces J from 4 to 11, so there are six perturbing levels expected near that region of the spectrum with angular momenta in the range $J = 6 - 8$ that would be observable in the present experiment. Some of those levels might be present in Fig. 6, as that region near $\nu_{11/2} \approx 15.2$ shows numerous levels that deviate from our simplified two-threshold MQDT models.

C. Coupling to low-lying *ng* states

Due to the angular momentum coupling to the ionic core, a two-photon excitation of a Rydberg state with $\ell = 4$ (*ng* state) is possible as both angular momentum selection rules and
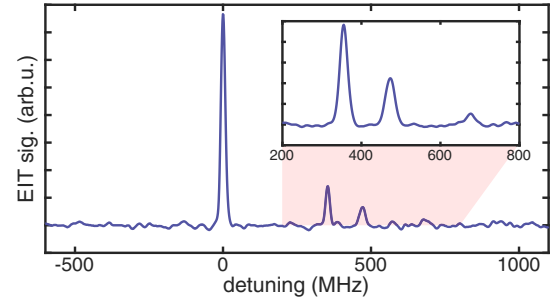
FIG. 7. EIT spectrum of the possible $13g$ state at 49052.771 cm^{-1}. A fine-structure splitting of four resonances is visible, the inset shows a second measurement run confirming the fourth resonance feature.

change of parity are fulfilled. Nonzero matrix elements can arise among others from f-wave admixture in the intermediate state or any d-wave admixture in the *ng* Rydberg state. Below the first ionization threshold, the highest $n_{\text{eff}, 11/2} = 15$. Due to its large angular momentum, the corresponding quantum defect is expected to be close to zero. We identified several candidates with very small $\mu_{11/2}$ and further eliminated lines too close to other *ns* or *nd* resonances, especially when close to already identified perturbers. One candidate meets all requirements and additionally shows a distinct fine structure pattern different from the previous investigated series, see Fig. 7. Its energy of 49052.771 cm^{-1} would be compatible to a $13g$ state connected to the second ionization threshold.

D. States above first ionization threshold

We observed several states above the first ionization threshold, which we assigned to the second ionization threshold. With an effective quantum defect $\mu_{11/2} \approx 0.78$, we would identify them as belonging to the *nd* series of the $J = 11/2$ state. We assign effective principal quantum numbers $n_{\text{eff}, 11/2}$ and measure their width as the FWHM value, as shown in Table V. Interestingly, their widths vary by more then two orders of magnitude, presumably caused by drastically different lifetimes. A more systematic survey of these states could improve the MQDT modeling by constraining the parameters, as discussed in Sec. V.

E. Isotope shift

To demonstrate the flexibility of our method and to exploit the large number of isotopes with high abundance in erbium,

TABLE V. States above the first ionization threshold, with their measured full width at half maximum. Only the first two states have significantly increased widths, while the other states show a linewidth comparable to the states below the threshold.

$n_{\text{eff}, 11/2}$	$\delta_{\text{eff}, 11/2}$	E_{meas} (cm^{-1})	FWHM (MHz)
17d	0.77	49284.43(1)	350
18d	0.80	49330.22(1)	30
18d	0.76	49332.16(1)	2
19d	0.80	49369.82(1)	4

TABLE VI. Total energy of the lowest state of the $27d$ multiplets for different isotopes, with the energy difference between the Rydberg state and the intermediate ($E_{i,\mathrm{Ry}}$) and the ground state (E_{tot}).

isotope	$E_{i,\mathrm{Ry}}$ (cm^{-1})	E_{tot} (cm^{-1})
164	24169.102(5)	49112.429(5)
166	24169.106(5)	49112.404(5)
168	24169.105(5)	49112.375(5)
170	24169.108(5)	49112.350(5)
$167_{(17/2,19/2)}$	24169.031(5)	49112.313(5)
$167_{(9/2,11/2)}$	24169.178(5)	49112.465(5)

we record the isotope shift of the $n = 27d$ multiplets for four bosonic isotopes, ^{164}Er, ^{166}Er, ^{168}Er, ^{170}Er, as well as for two hyperfine states of the fermionic ^{167}Er isotope, see Table VI. This shows the versatility of our approach, and our ability to switch easily between the addressed isotopes and hyperfine states. For the energy of the first photon, we take the value from Ref. [45] to calculate the total energy.

VI. SUMMARY AND OUTLOOK

We observe about 550 Rydberg states in erbium with unprecedented precision and with principal quantum numbers as high as $n = 140$. By controlling the light polarization and applying a magnetic field, we can resolve the splitting between Zeeman sublevels and are able to assign the total angular momentum J to the observed Rydberg series and measure their g_J factors.

The number and precision of states allowed for an accurate determination of the MQDT parameters for the ns-Rydberg series. We were not able to unambiguously determine the MQDT parameters for the more complicated nd-Rydberg series. Two restricted models of the series were able to reproduce many of the features of the nd series. However, the g factors for several of the states and the details of the perturbations were not accurately reproduced. Future technical improvements will allow a higher absolute accuracy of the measured Rydberg energies as well as enabling a more systematic survey of the states between the two ionization thresholds, thus providing an improved basis for understanding and modeling of the nd-Rydberg series.

Our spectroscopic study marks a step in creating a toolbox for Rydberg physics. While our first survey concentrated on an excitation scheme using a $6s$ electron, our vision is to employ schemes using inner-shell $4f$ electrons. Additionally, to the possibilities offered by two-electron atoms like strontium or ytterbium, we expect dramatically new physics to be present and that the active submerged shell will affect fundamental properties of these systems.

APPENDIX A: MULTICHANNEL QUANTUM DEFECT EQUATIONS (MQDT)

The formulas used to calculate the energies and g factors of the states are given below. They follow the notation in Ref. [12] and are given with little discussion. For a fuller derivation and discussion, see Ref. [46] or [12]. The mass of ^{166}Er$^+$ was taken from Ref. [47] to be $M_{166+} = 165.930\,293\,1u - m_e$ with $u = 1.660\,539\,066\,60 \times 10^{-27}$ kg and $m_e = 9.109\,383\,701\,5 \times 10^{-31}$ kg taken from the CODATA values. The Rydberg constant, R_{166}, was taken to be scaled from the CODATA R_∞ value as $R_{166} = 109\,737.315\,681\,60$ cm$^{-1} \times M_{166+}/(M_{166+} + m_e)$.

1. Calculated energies

When the Rydberg electron is outside of the ionic core, the unphysical wave functions can be written as

$$|\psi_i\rangle = \sum_{i'} |\Phi_{i'}\rangle [f_{i'}(r)\delta_{i',i} - g_{i'}(r)K_{i',i}], \qquad (A1)$$

where the $f(g)$ are the energy normalized, radial Coulomb functions which are regular (irregular) at the origin and **K** is the real, symmetric K matrix. See Ref. [46] for the properties of these functions that depend on the radial position of the Rydberg electron. The core states $|\Phi_{i'}\rangle$ contain all other degrees of freedom. For the Rydberg states described above, the core states can be written as

$$|\Phi_i\rangle = |(J_{c,i}(s\ell_i)j_i)J_iM_i\rangle, \qquad (A2)$$

where $J_{c,i}$ is the total angular momentum of the core, s is the spin of the Rydberg electron, ℓ_i is the orbital angular momentum of the Rydberg electron, j_i is the total angular momentum of the Rydberg electron, J_i is the total angular momentum, and M_i is the related azimuthal quantum number. The order of parenthesis is meant to indicate the order that the angular momenta are coupled together.

The $|\psi_i\rangle$ function is unphysical because the $f_{i'}$, $g_{i'}$ functions diverge at large r for closed channels defined by $E < E_{c,i'}$. At bound-state energies, the $|\psi_i\rangle$ can be superposed to give a physical eigenfunction which converges to 0 at large r. For the bound state at energy E_b, the superposition can be written as

$$|\psi_b\rangle = \sum_i |\psi_i\rangle \frac{\cos(\beta_i)}{\nu_i^{3/2}} A_{i,b} \qquad (A3)$$

and the condition that determines the bound states is [46]

$$\sum_i [\tan(\beta_{i'})\delta_{i',i} + K_{i',i}] \frac{\cos(\beta_i)}{\nu_i^{3/2}} A_{i,b} = 0, \qquad (A4)$$

where $\beta_i = \pi(\nu_i - \ell_i)$ and the effective quantum number is defined as $E = E_{c,i} - R_{166}/(2\nu_i^2)$ in terms of the total energy, E, and the energy of the ith core state, $E_{c,i}$ with both energies in cm^{-1}. The Rydberg constant is given in Appendix A above. This condition only holds when the term in [ ] has a determinant equal to 0. The normalization condition when the K matrix is slowly varying with energy is

$$\sum_i A_{i,b}^2 = 1, \tag{A5}$$

which, with Eq. (A4), defines the $A_{i,b}$ within an irrelevant, overall sign.

2. Calculated *g* factor

The g factor for individual states can be approximately calculated from the MQDT parameters by assuming the contribution is negligible when the Rydberg electron is within the ionic core region. This situation is covered by Eq. (4.1.2) of Ref. [46] (or, similarly, Eqs. (15) and (16) of Ref. [12]):

$$g_b = \sum_{i,i'} A_{i,b} \langle \Phi_i | \hat{g} | \Phi_{i'} \rangle O_{ib,i'b} A_{i'b}, \tag{A6}$$

where the overlap matrix is

$$O_{ib,i'b} = \frac{2\sqrt{\nu_{ib}\nu_{i'b}}}{\nu_{ib} + \nu_{i'b}} \frac{\sin(\beta_{ib} - \beta_{i'b})}{(\beta_{ib} - \beta_{i'b})}, \tag{A7}$$

with $O_{ib,ib} = 1$. The g-operator matrix element is complicated but only uses Eqs. (3.7.9), (5.4.1), (5.4.3), (7.1.7), and (7.1.8) of Ref. [48]. The matrix element is

$$\langle \Phi_i | \hat{g} | \Phi_{i'} \rangle = \frac{1}{M_i} \langle \Phi_i | g_{c,i} J_{c,z} + \ell_z + g_s s_z | \Phi_{i'} \rangle$$

$$= \frac{\langle \Phi_i || g_{c,i} J_c^{(1)} + \ell^{(1)} + g_s s^{(1)} || \Phi_{i'} \rangle}{\Lambda(J_i)}, \tag{A8}$$

where $g_c = 1.230$ for the $J_c = 13/2$ state and 1.101 for the $J_c = 11/2$ state [49,50] and $g_s = 2.002319....$. The $\Lambda(x) \equiv \sqrt{(2x+1)(x+1)x}$. The reduced matrix elements when ℓ is the same for i and i' are

$$\langle \Phi_i || \ell^{(1)} || \Phi_{i'} \rangle = \delta_{J_{c,i} J_{c,i'}} \mathcal{G}_1 \mathcal{G}_2 \Lambda(\ell),$$

$$\langle \Phi_i || s^{(1)} || \Phi_{i'} \rangle = \delta_{J_{c,i} J_{c,i'}} \mathcal{G}_1 \mathcal{G}_3 \Lambda(s),$$

$$\langle \Phi_i || J_c^{(1)} || \Phi_{i'} \rangle = \delta_{j_i j_{i'}} \delta_{J_{c,i} J_{c,i'}} \mathcal{G}_4 \Lambda(J_{c,i}), \tag{A9}$$

where we have made the approximation that the core angular momentum operator does not mix core states with different J_c and

$$\mathcal{G}_1 = (-1)^{J_{c,i} + j_{i'} + J + 1} (2J+1) \begin{Bmatrix} j_i & J & J_{c,i} \\ J & j_{i'} & 1 \end{Bmatrix},$$

$$\mathcal{G}_2 = (-1)^{s + \ell + j_i + 1} [j_i, j_{i'}] \begin{Bmatrix} \ell & j_i & s \\ j_{i'} & \ell & 1 \end{Bmatrix},$$

$$\mathcal{G}_3 = (-1)^{s + \ell + j_{i'} + 1} [j_i, j_{i'}] \begin{Bmatrix} s & j_i & \ell \\ j_{i'} & s & 1 \end{Bmatrix},$$

$$\mathcal{G}_4 = (-1)^{J_{c,i} + j_i + J + 1} (2J+1) \begin{Bmatrix} J_{c,i} & J & j_i \\ J & J_{c,i'} & 1 \end{Bmatrix}. \tag{A10}$$

3. Frame transformation approximation

The energy-dependent K matrix exactly determines the bound-state energies and approximately allows evaluation of other state properties (e.g., the g factor). Unfortunately, the electronic structure of Er is too complicated for an accurate, *ab initio* calculation. Nevertheless, there are two possible paths to obtain the K matrix. The first is to use the experimental data, without any guidance from a model, to obtain a fit of the K matrix. This is described in Sec. V A. The other is to utilize an approximation to restrict the possible values of the K matrix before using the experimental energies to fit the elements of the K matrix. This section describes this second method where the approximation is based on a frame transformation. The following section will use a different physical idea to reduce the number of parameters defining the K matrix.

The frame transformation approximation assumes there is a channel coupling that diagonalizes the K matrix when the electron is in the core region. The Rydberg states are attached to fine structure split core states of Er$^+$: $4f^{12}(^3H_6)6s_{1/2}J_c$ with $J_c = 13/2$ and $11/2$ being the ground and first excited states, respectively. The idea is to call the angular momentum of the $4f^{12}$ inner electrons $J_f = 6$ and the angular momentum of the valence $6s$ electron $J_s = 1/2$. In terms of the notation of Appendix A 1, the channel states when the electron is outside of the core, Eq. (A2), is expanded to

$$|\Phi_i\rangle = |((J_f J_s)J_{c,i}(s\ell_i)j_i)J_i M_i\rangle. \tag{A11}$$

We assume that the coupling that leads to a diagonal K matrix is given by

$$|\Phi_{i'}^{in}\rangle = |(J_f((J_s s)S_{o,i'}\ell_{i'})J_{o,i'})J_{i'}M_{i'}\rangle, \tag{A12}$$

where the order of coupling is the spin of the $6s$ and Rydberg electron coupled to give total outer spin, $S_{o,i}$, then the total outer spin is coupled to the orbital angular momentum of the Rydberg electron, ℓ_i, to give the total outer angular momentum, $J_{o,i}$, then the angular momentum of the inner $4f^{12}$, $J_f = 6$ is coupled to the total outer angular momentum to give the total angular momentum. The overlap matrix between these couplings are only nonzero if $J_i = J_{i'}$, $M_i = M_{i'}$, and $\ell_i = \ell_{i'}$. For Er, the $s = 1/2$ and is automatically the same.

With the help of the intermediate coupling $|(J_f(J_s(s\ell)j)J_o)JM\rangle$, the projection of the two coupling schemes is derived from Eq. (6.1.5) of Ref. [48] to give

$$\langle \Phi_i | \Phi_{i'}^{in} \rangle = [j_i, S_{o,i'}, J_{c,i}, J_{o,i'}](-1)^{J_f + 2J_s + j_i + J + s + \ell + J_{o,i'}}$$

$$\times \begin{Bmatrix} J_f & J_s & J_{c,i} \\ j_i & J & J_{o,i'} \end{Bmatrix} \begin{Bmatrix} J_s & s & S_{o,i'} \\ \ell & J_{o,i'} & j_i \end{Bmatrix}, \tag{A13}$$

with $[j_1, j_2...] = \sqrt{(2j_1+1)(2j_2+1)....}$.

For the case where the Rydberg electron has s character, there are two channels for $J = 6$ and one channel for $J = 7$. Thus, the frame transformation is only useful for $J = 6$. The two $|\Phi\rangle$ states can be defined as $|J_c\rangle \equiv ((^3H_6 6s_{1/2})J_c ns_{1/2})J = 6$, with $J_c = 13/2$ and $11/2$ while the two $|\Phi^{in}\rangle$ can be defined as $|J_o\rangle \equiv (^3H_6(6s_{1/2}ns_{1/2})^{2S_o+1}S_{S_o})J = 6$ with $S_o = 0$ and 1. In

this simplified notation, $\langle 13/2|0\rangle = \langle 11/2|1\rangle = \sqrt{7/13}$ and $\langle 13/2|1\rangle = -\langle 11/2|0\rangle = \sqrt{6/13}$.

For the case where the Rydberg electron has d character, there are 4 channels for $J = 6$ and 7 and three channels for $J = 8$. The $|\Phi\rangle$ can be defined as $|J_c, j\rangle \equiv ((^3H_6 6s_{1/2})J_c nd_j)J$. Both $J = 6$ and 7 have the four couplings $|13/2, 3/2\rangle$, $|13/2, 5/2\rangle$, $|11/2, 3/2\rangle$, and $|11/2, 5/2\rangle$ while $J = 8$ only has $|13/2, 3/2\rangle$, $|13/2, 5/2\rangle$, and $|11/2, 5/2\rangle$. The $|\Phi^{\rm in}\rangle$ can be defined as $|S_o, J_o\rangle \equiv (^3H_6(6s_{1/2}nd_{1/2})^{2S_o+1}D_{J_o})J$. Both $J = 6$ and 7 have four couplings, $|0, 2\rangle$, $|1, 1\rangle$, $|1, 2\rangle$, and $|1, 3\rangle$ while $J = 8$ only has $|0, 2\rangle$, $|1, 2\rangle$, and $|1, 3\rangle$. If we let the quantum defects vary with J, then there are 11 free parameters for all K matrices.

4. Interaction-inspired K-matrix approximation

A completely different method for parametrizing the K matrix for the nd channels is to identify interactions that lead to coupling between channels or shifts in channels. This section discusses some of the important interactions.

There are two shifts that are expected. The first is the average K matrix will depend on J. The second is the shift due to the spin-orbit interaction. These lead to terms of the form:

$$K_{ii'}^{(d)} = \delta_{i,i'}[\tan(\pi\mu_J) + \delta_{j,3/2}\tan(\pi\mu_{3/2})], \quad (A14)$$

where we have put all of the spin-orbit shift into the $nd_{3/2}$ channels.

Another important interaction arises from a second rank coupling of the core state interacting with the nd electron. This type of interaction can arise through a quadrupole moment of the ionic core or from an anisotropic polarizability of the core [51]. Other long-range interaction terms between the Rydberg electron and the anisotropic ionic core could be introduced, such as the vector hyperpolarizabity term, but the present level of theory has not yet taken such interactions into account [52,53]. The angular part of the matrix element arises from

$$Q_{ii'} = \langle \Phi_i|P_2(\hat{r}_c \cdot \hat{r})|\Phi_{i'}\rangle, \quad (A15)$$

where $|\Phi_i\rangle$ are from Eq. (A2) and the $P_2(\hat{r}_c \cdot \hat{r})$ is the Legendre polynomial of the Rydberg electron dotted into core electrons. To evaluate this, we use the fact that the $4f^{12}$ electrons are coupled as $S_f = 1$, $L_f = 5$, and $J_f = 6$ before coupling to the $6s$ electron to give J_c. Using Eqs. (5.4.6), (7.1.6), (7.1.7), and (7.1.8) of Ref. [48], we find $Q_{ii'} = C\, q_{ii'}$,

$$q_{ii'} = (-1)^{2J_{c,i'}+2j_i+J}\frac{[j_i, j_{i'}, J_{c,i}, J_{c,i'}]}{[J]}\begin{Bmatrix} \ell & j_i & s \\ j_{i'} & \ell & 2 \end{Bmatrix}$$

$$\times \begin{Bmatrix} J & j_i & J_{c,i} \\ 2 & J_{c,i'} & j_{i'} \end{Bmatrix}\begin{Bmatrix} J_f & J_{c,i} & J_s \\ J_{c,i'} & J_f & 2 \end{Bmatrix}, \quad (A16)$$

when making the approximation $\ell_i = \ell_{i'}$. Since the size of the second rank coupling is unknown, we add this to the K matrix with a fitting parameter to obtain the total:

$$K_{ii'} = K_{ii'}^{(d)} + C_q q_{ii'}. \quad (A17)$$
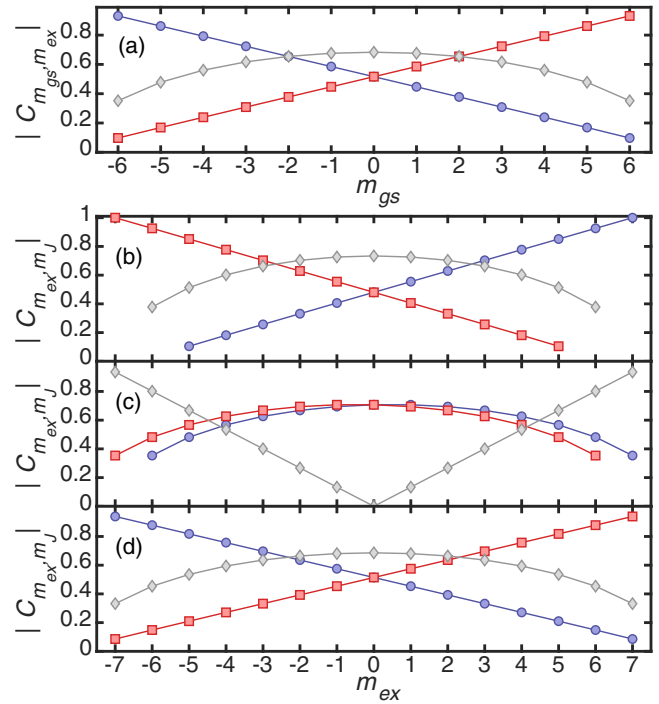
FIG. 8. Absolute values of the transition matrix elements for the first transition (a) $|J_{\rm gs} = 6, m_{\rm gs}\rangle \rightarrow |J_{\rm ex} = 7, m_{\rm ex}\rangle$ as well as for the three possibilities of the second transition, (b) $|J_{\rm ex} = 7, m_{\rm ex}\rangle \rightarrow |J = 6, m_J\rangle$, (c) $|J_{\rm ex} = 7, m_{\rm ex}\rangle \rightarrow |J = 7, m_J\rangle$, and (d) $|J_{\rm ex} = 7, m_{\rm ex}\rangle \rightarrow |J = 8, m_J\rangle$. Circles (squares) encode σ^- (σ^+) transitions, diamonds display π transitions.

If we stop at this level, there are five free parameters in the K matrix.

APPENDIX B: ESTIMATION OF THE SPECTRAL PATTERN OF DIFFERENT J STATES OF THE nd MANIFOLD

For a simple estimation of the relative EIT resonance strength, we create a list of all dipole-allowed transitions from the ground state $|J_{\rm gs} = 6, m_{\rm gs}\rangle$ over the intermediate state $|J_{\rm ex} = 7, m_{\rm ex}\rangle$ to the Rydberg states $|J = 6, 7, 8, m_J\rangle$. We calculate the transition matrix elements for each single photon transition using the Wigner $3j$ symbol, leading to

$$C_{m_{\rm gs}, m_{\rm ex}} = (-1)^{J_{\rm gs}-1+m_{\rm ex}}\sqrt{2J_{\rm gs}+1}\begin{pmatrix} J_{\rm gs} & 1 & J_{\rm ex} \\ m_{\rm gs} & \Delta m & -m_{\rm ex} \end{pmatrix}$$

for the first transition and

$$C_{m_{\rm ex}, m_J} = (-1)^{J_{\rm ex}-1+m_J}\sqrt{2J_{\rm ex}+1}\begin{pmatrix} J_{\rm ex} & 1 & J \\ m_{\rm ex} & \Delta m & -m_J \end{pmatrix}$$

for the transition from the intermediate to the Rydberg state. Figure 8 shows the calculated values as a function of the m_J state for all possible J values.

For each possible combination, we can calculate the relative two-photon strength $|C_{m_{\rm gs}, m_{\rm ex}} \times C_{m_{\rm ex}, m_J}|$ and multiply it with our estimated amplitudes of our light polarizations (here we assume 5% π-light) and the corresponding amplitude of
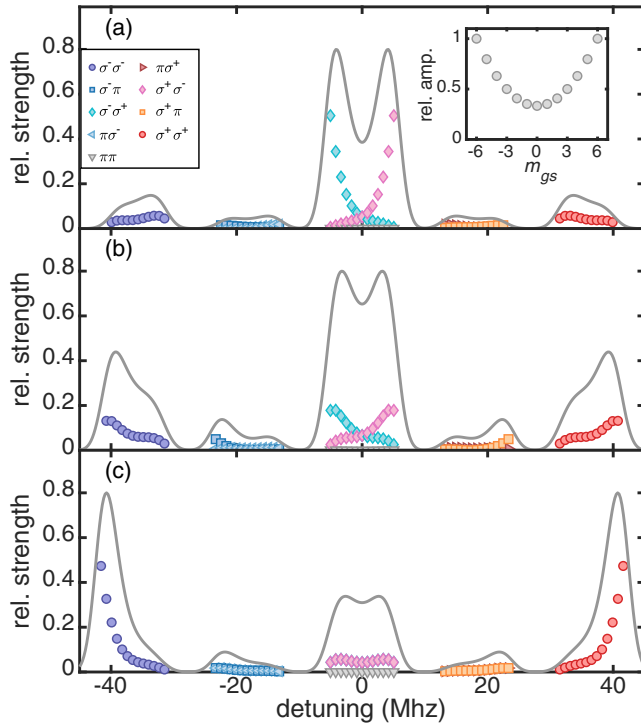
FIG. 9. Estimation of the spectral pattern given the relative two-photon transition strength for (a) $|J = 6, m_J\rangle$, (b) $|J = 7, m_J\rangle$, and (c) $|J = 8, m_J\rangle$. Different colors and symbols encode the transition type (see legend). The inset shows the assumed relative distribution of populations among the ground-state manifold.

the population of the Zeeman level of the ground state. Here, the population amplitudes account for the effects of optical pumping during the spectroscopy. Now we can plot it as a function of the two-photon detuning for a given magnetic field, in our case 10.7 G, see Fig. 9. Here we exemplary assume a g factor $g_J = 1.22$ for the Rydberg state. The solid line gives a total sum of all transitions, taking a Gaussian line shape with a width of 2 MHz and the corresponding two-photon strength as amplitude for each transition.

Each J has its own characteristic spectral pattern: For $J = 6$, a strong central peak originating from $\Delta m_J = 0$ transitions (split for large g_J) with two weaker side peaks ($\Delta m_J = \pm 2$ transitions) is expected, while for $J = 8$ the central peak should be much weaker and the side peaks should be strongest. For $J = 7$, the central peak as well as the side peaks have roughly the same strength, and only here the $\Delta m_J = \pm 1$ transitions also have a significant strength and might be visible.

APPENDIX C: ESTIMATION OF THE EXPERIMENTAL UNCERTAINTIES AND FREQUENCY INACCURACIES

The used wave meter has an absolute frequency accuracy of ± 60 MHz, given as 3σ interval [54]. This error is partially systematic, depending on various environmental conditions. Long-time measurements on a laser locked to an atomic tran-

sition in our laboratory shows frequency deviations of typical 20 MHz within one hour. We therefore assume a fundamental 1σ error of ± 20 MHz for single measurements and an additional 1σ systematic uncertainty of ± 10 MHz when combining multiple measurement sets.

To be able to give the absolute energy of the measured states, we have to add the first transition, whose energy we also measure with the same wave meter. We always measure the fundamental frequency of both probe and coupling beam before frequency doubling. We estimate our wave-meter-limited accuracy for single state energies therefore to about ± 69 MHz, i.e., $\pm 0.0023 \, \text{cm}^{-1}$. The final error in the determination of the ionization threshold includes the error of the fit itself and the combined systematic uncertainty of probe- and coupling frequency ($\pm 0.0013 \, \text{cm}^{-1}$), resulting in an estimated accuracy of $\pm 0.0023 \, \text{cm}^{-1}$.

An additional uncertainty in our resonance position energies results from our wavelength monitoring. While scanning the coupling frequency using an analog voltage ramp, we continuously read out the measured frequencies from the wave meter. Due to the limited and variable read-out speed (depending on the light intensity coupled to the wave meter), which is not synchronized to the analog ramp, we record frequency traces during several scans and take the maximum and minimum measured wavelength to calibrate the frequency axis of the scans.

For most of the wide scans used in our survey, we estimate the absolute uncertainty of the resonance positions with $0.07 \, \text{cm}^{-1}$, mainly limited by nonlinearities within each frequency scan. For the nd states investigated for the g factor, the smaller scan ranges minimize those nonlinearities and allows us to reduce the absolute uncertainty to $0.005 \, \text{cm}^{-1}$, now primarily limited by the absolute accuracy of the wave meter.

The main uncertainty in the fitting of the g factor is the determination of the proper frequency axis scale. For these very narrow scan ranges, the finite read-out speed of the wave meter results in significant variations of the frequency axis scale of up to 20% when comparing different experimental runs where the scan range should have been identical. We account for this by scaling all frequency axes of one set to the maximum range, as the described frequency axis calibration will always lead to an underestimation of the scan range. The given error of the g factor takes into account the fit error itself, the uncertainty of the B-field calibration and the rescaling factor.

APPENDIX D: LIST OF ALL OBSERVED STATES

All Rydberg features observed in this work using the EIT technique are summarized in Table VII. We provide the energies, as determined with the wavemeter, with an upper bound of the error of $0.07 \, \text{cm}^{-1}$. Some features have been measured with higher precision, see main text. The states are sorted by effective quantum number, as assigned to the lower ($J = 13/2$) and upper ($J = 11/2$) ionization threshold.

TABLE VII. Table listing all observed features, listed by effective quantum number n_{eff}, and term energy. Errors in energy are 0.07 cm^{-1}. Some features have been measured with higher precision, see main text.

$n_{\text{eff},13/2}$	$E\,(\text{cm}^{-1})$								
15	48828.76								
16	48841.30	48842.77	48842.83	48843.43	48844.77	48845.23	48863.11	48863.98	
17	48888.33	48889.26	48889.80	48889.93	48891.47	48892.07	48892.73	48909.31	48909.33
18	48929.32	48929.99	48930.00	48930.01	48930.03	48930.87	48931.46	48931.71	48931.94	48945.19
19	48963.98	48964.28	48964.32	48964.92	48964.98	48965.52	48968.26	48969.00	48979.36
20	48992.82	48993.07	48993.20	48993.44	48993.70	49002.52			
21	49015.08	49016.30	49016.42	49017.03	49017.42	49026.46	49028.00		
22	49038.45	49038.83	49039.17	49039.37	49039.43	49047.31	49052.80	49052.81	49052.81	49052.82
23	49056.91	49056.93	49057.10	49057.37	49057.79	49058.02	49058.13	49064.84	
24	49073.44	49073.97	49073.99	49074.33	49074.39	49074.79	49080.13	49081.41	
25	49087.98	49088.54	49088.66	49088.68	49088.83	49093.78			
26	49100.58	49100.86	49101.22	49101.51	49101.54	49101.62	49101.70	49101.72	49105.45
27	49111.45	49112.39	49112.56	49112.82	49112.98	49113.06	49113.14	49117.95	
28	49122.73	49122.76	49122.86	49123.23	49123.26	49123.29	49127.35		
29	49132.01	49132.16	49132.39	49132.49	49132.53	49132.63	49136.08		
30	49140.44	49140.60	49140.75	49140.96	49140.98	49144.04			
31	49147.99	49148.12	49148.28	49148.38	49148.46	49148.50	49151.25	49151.27	
32	49154.90	49155.02	49155.17	49155.25	49155.35	49157.12	49157.74	49157.82	
33	49160.85	49161.25	49161.41	49161.45	49161.52	49161.60	49163.83		
34	49167.02	49167.12	49167.15	49167.22	49167.29	49169.25			
35	49172.18	49172.38	49172.45	49172.51	49174.33				
36	49177.01	49177.19	49177.25	49177.28	49177.31	49178.94			
37	49181.43	49181.51	49181.60	49181.63	49181.69	49181.73			
38	49185.54	49185.70	49185.75	49185.80	49186.73				
39	49188.90	49188.91	49189.34	49189.52	49189.54	49189.55	49189.57	49191.35	
40	49192.84	49192.98	49193.02	49193.04	49193.07	49194.52			
41	49196.09	49196.22	49196.26	49196.28	49196.31	49197.61			
42	49199.13	49199.25	49199.29	49199.33	49200.52				
43	49201.95	49202.08	49202.11	49202.15					
45	49207.04	49207.08	49207.14	49207.16	49207.20	49208.14			
46	49209.35	49209.42	49209.45	49209.49	49210.35				
47	49211.49	49211.53	49211.58	49211.61	49211.64	49211.69	49211.69	49212.43	49213.08
48	49213.51	49213.53	49213.59	49213.61	49213.62	49213.64	49214.30		
50	49217.20	49217.28	49217.29	49217.32	49217.32	49218.53			
51	49218.85	49218.95	49218.96	49219.01	49219.02	49219.63			
52	49220.48	49220.55	49220.57	49220.59	49221.17				
53	49221.99	49222.04	49222.07	49222.08	49222.64				
54	49223.40	49223.45	49223.47	49223.49					
55	49224.73	49224.79	49224.81	49224.82	49225.34				
56	49226.00	49226.00	49226.06	49226.08	49226.73				
57	49227.23	49227.27	49227.29	49227.30	49227.75				
58	49228.37	49228.40	49228.42	49228.45	49228.45	49228.83	49228.86	49229.11	49229.20
59	49229.45	49229.47	49229.49	49229.51	49229.52	49229.83	49229.87		
60	49230.49	49230.53	49230.54	49230.55					
61	49231.29	49231.35	49231.38	49231.40	49231.89				
62	49232.59	49232.64	49232.67	49232.67	49232.69				
64	49234.13	49234.16	49234.17	49234.18	49234.60	49234.62	49234.62	49234.64	49234.76
65	49234.93	49234.97	49234.98	49234.99	49235.29				
66	49235.72	49235.74	49235.76	49235.77	49235.78	49236.04	49236.10	49236.14	49236.17
67	49236.50								
68	49237.05	49237.14	49237.17	49237.18	49237.19	49237.46			
69	49237.83	49237.86	49237.87	49237.87	49237.89	49238.13			
71	49239.10	49239.14	49239.15						
72	49239.69	49239.70	49239.71	49239.71	49239.71	49239.72	49239.94		
73	49240.26	49240.27	49240.28	49240.29					
82	49244.51	49244.53	49244.54	49244.55					
83	49244.90	49244.91	49244.92						

TABLE VII. *(Continued.)*

$n_{\mathrm{eff},13/2}$	$E(\mathrm{cm}^{-1})$						
84	49245.28	49245.28	49245.29	49245.31	49245.32		
85	49245.64	49245.65	49245.66	49245.67	49245.68		
86	49245.98	49245.98	49245.99	49246.00	49246.00		
92	49247.86	49247.87					
93	49248.11	49248.13	49248.14	49248.16			
94	49248.39	49248.39	49248.41				
95	49248.66	49248.67	49248.67	49248.68			
96	49248.90	49248.91	49248.92	49248.93			
97	49249.15	49249.15	49249.17	49249.17	49249.17	49249.19	
98	49249.38	49249.39	49249.45	49249.47			
99	49249.61	49249.62	49249.63	49249.65			
100	49249.85	49249.85	49249.86	49249.86	49249.93	49249.95	
101	49250.02	49250.03	49250.05	49250.06	49250.16	49250.18	
102	49250.24	49250.25	49250.25	49250.26			
103	49250.48	49250.49					
104	49250.65	49250.67					
105	49250.85	49250.86					
106	49251.05	49251.08					
107	49251.20	49251.21					
108	49251.43	49251.44					
109	49251.55	49251.57	49251.59				
110	49251.73	49251.74	49251.76				
111	49251.89	49251.90	49251.91	49251.91	49251.93	49251.93	
112	49252.04	49252.05	49252.07	49252.08			
113	49252.19	49252.19	49252.22	49252.23			
114	49252.34	49252.35	49252.36				
115	49252.45	49252.46	49252.46	49252.47			
118	49252.92	49252.95	49252.96				
119	49253.04	49253.08	49253.08				
120	49253.16	49253.19	49253.20				
121	49253.27	49253.30	49253.31				
122	49253.37	49253.41	49253.42	49253.45	49253.46	49253.48	
123	49253.51	49253.60					
124	49253.65	49253.66					
125	49253.72	49253.76	49253.77	49253.83			
126	49253.87	49253.87	49253.93				
127	49253.97	49253.97	49254.02	49254.04			
128	49254.09	49254.09	49254.15				
129	49254.19	49254.19	49254.24				
130	49254.28	49254.28	49254.29	49254.31	49254.33	49254.35	
131	49254.38	49254.38	49254.39	49254.40	49254.43		
132	49254.44	49254.49	49254.49	49254.52	49254.54		
133	49254.58	49254.62					
134	49254.66	49254.70	49254.71				
135	49254.73	49254.74	49254.77	49254.77	49254.78	49254.78	49254.78	49254.79
136	49254.85	49254.86	49254.89				
137	49254.93	49254.97					
138	49255.01	49255.05					
139	49255.09	49255.13					
140	49255.15	49255.17					

$n_{\mathrm{eff},11/2}$	$E(\mathrm{cm}^{-1})$			
11	48830.62	48830.66		
12	48970.09			
14	49157.12	49189.47		
15	49219.46	49228.23	49229.09	49229.11
16	49284.46			
17	49330.24	49332.19		
18	49369.84			

[1] D. Jaksch, J. I. Cirac, P. Zoller, S. L. Rolston, R. Côté, and M. D. Lukin, Fast Quantum Gates for Neutral Atoms, Phys. Rev. Lett. **85**, 2208 (2000).

[2] G. K. Brennen, I. H. Deutsch, and P. S. Jessen, Entangling dipole-dipole interactions for quantum logic with neutral atoms, Phys. Rev. A **61**, 062309 (2000).

[3] M. Saffman, T. G. Walker, and K. Mølmer, Quantum information with Rydberg atoms, Rev. Mod. Phys. **82**, 2313 (2010).

[4] A. Browaeys and T. Lahaye, Many-body physics with individually controlled Rydberg atoms, Nat. Phys. **16**, 132 (2020).

[5] D. Barredo, S. de Léséleuc, V. Lienhard, T. Lahaye, and A. Browaeys, An atom-by-atom assembler of defect-free arbitrary 2D atomic arrays, Science **354**, 1021 (2016).

[6] H. Bernien, S. Schwartz, A. Keesling, H. Levine, A. Omran, H. Pichler, S. Choi, A. S. Zibrov, M. Endres, M. Greiner, V. Vuletić, and M. D. Lukin, Probing many-body dynamics on a 51-atom quantum simulator, Nature (London) **551**, 579 (2017).

[7] D. Barredo, V. Lienhard, S. de Léséleuc, T. Lahaye, and A. Browaeys, Synthetic three-dimensional atomic structures assembled atom by atom, Nature (London) **561**, 79 (2018).

[8] K.-N. Schymik, V. Lienhard, D. Barredo, P. Scholl, H. Williams, A. Browaeys, and T. Lahaye, Enhanced atom-by-atom assembly of arbitrary tweezer arrays, Phys. Rev. A **102**, 063107 (2020).

[9] M. Saffman and K. Mølmer, Scaling the neutral-atom Rydberg gate quantum computer by collective encoding in holmium atoms, Phys. Rev. A **78**, 012336 (2008).

[10] R. Mukherjee, J. Millen, R. Nath, M. P. A. Jones, and T. Pohl, Many-body physics with alkaline-earth Rydberg lattices, J. Phys. B: At. Mol. Opt. Phys. **44**, 184010 (2011).

[11] T. Topcu and A. Derevianko, Divalent rydberg atoms in optical lattices: Intensity landscape and magic trapping, Phys. Rev. A **89**, 023411 (2014).

[12] F. Robicheaux, D. W. Booth, and M. Saffman, Theory of long-range interactions for Rydberg states attached to hyperfine-split cores, Phys. Rev. A **97**, 022508 (2018).

[13] J. Wilson, S. Saskin, Y. Meng, S. Ma, R. Dilip, A. Burgers, and J. Thompson, Trapped arrays of alkaline earth rydberg atoms in optical tweezers, arXiv:1912.08754 [quant-ph].

[14] J. Millen, G. Lochead, and M. P. A. Jones, Two-Electron Excitation of an Interacting Cold Rydberg Gas, Phys. Rev. Lett. **105**, 213004 (2010).

[15] A. D. Bounds, N. C. Jackson, R. K. Hanley, R. Faoro, E. M. Bridge, P. Huillery, and M. P. A. Jones, Rydberg-Dressed Magneto-Optical Trap, Phys. Rev. Lett. **120**, 183401 (2018).

[16] F. Camargo, R. Schmidt, J. D. Whalen, R. Ding, G. Woehl, S. Yoshida, J. Burgdörfer, F. B. Dunning, H. R. Sadeghpour, E. Demler, and T. C. Killian, Creation of Rydberg Polarons in a Bose Gas, Phys. Rev. Lett. **120**, 083401 (2018).

[17] L. Couturier, I. Nosske, F. Hu, C. Tan, C. Qiao, Y. H. Jiang, P. Chen, and M. Weidemüller, Measurement of the strontium triplet rydberg series by depletion spectroscopy of ultracold atoms, Phys. Rev. A **99**, 022503 (2019).

[18] H. Lehec, A. Zuliani, W. Maineult, E. Luc-Koenig, P. Pillet, P. Cheinet, F. Niyaz, and T. F. Gallagher, Laser and microwave spectroscopy of even-parity Rydberg states of neutral ytterbium and multichannel-quantum-defect-theory analysis, Phys. Rev. A **98**, 062506 (2018).

[19] M. A. Norcia, A. W. Young, and A. M. Kaufman, Microscopic Control and Detection of Ultracold Strontium in Optical-Tweezer Arrays, Phys. Rev. X **8**, 041054 (2018).

[20] A. Cooper, J. P. Covey, I. S. Madjarov, S. G. Porsev, M. S. Safronova, and M. Endres, Alkaline-Earth Atoms in Optical Tweezers, Phys. Rev. X **8**, 041055 (2018).

[21] S. Saskin, J. T. Wilson, B. Grinkemeyer, and J. D. Thompson, Narrow-Line Cooling and Imaging of Ytterbium Atoms in an Optical Tweezer Array, Phys. Rev. Lett. **122**, 143002 (2019).

[22] I. S. Madjarov, J. P. Covey, A. L. Shaw, J. Choi, A. Kale, A. Cooper, H. Pichler, V. Schkolnik, J. R. Williams, and M. Endres, High-fidelity entanglement and detection of alkaline-earth Rydberg atoms, Nat. Phys. **16**, 857 (2020).

[23] J. J. McClelland and J. L. Hanssen, Laser Cooling Without Repumping: A Magneto-Optical Trap for Erbium Atoms, Phys. Rev. Lett. **96**, 143005 (2006).

[24] B. Lev, M. Lu, and S. H. Youn, Laser cooling and trapping the most magnetic atom, dysprosium, in *Frontiers in Optics 2010/Laser Science XXVI* (Optical Society of America, Washington, DC, 2010), p. STuD4.

[25] A. Frisch, K. Aikawa, M. Mark, A. Rietzler, J. Schindler, E. Zupanič, R. Grimm, and F. Ferlaino, Narrow-line magneto-optical trap for erbium, Phys. Rev. A **85**, 051401(R) (2012).

[26] J. Miao, J. Hostetter, G. Stratis, and M. Saffman, Magneto-optical trapping of holmium atoms, Phys. Rev. A **89**, 041401(R) (2014).

[27] I. S. Cojocaru, S. V. Pyatchenkov, S. A. Snigirev, I. A. Luchnikov, E. S. Kalganova, G. A. Vishnyakova, D. N. Kublikova, V. S. Bushmakin, E. T. Davletov, V. V. Tsyganok, O. V. Belyaeva, A. Khoroshilov, V. N. Sorokin, D. D. Sukachev, and A. V. Akimov, Light-assisted collisions in ultracold Tm atoms, Phys. Rev. A **95**, 012706 (2017).

[28] J. Hostetter, J. D. Pritchard, J. E. Lawler, and M. Saffman, Measurement of holmium Rydberg series through magneto-optical trap depletion spectroscopy, Phys. Rev. A **91**, 012507 (2015).

[29] Z. Hai-jun, X. Xiang-yuan, H. Wen, L. Liang-quan, and C. Die-yan, Study of high-lying excited states of rare-earth element dy by laser resonance ionization spectroscopy, Acta Phys. Sin. (Overseas Edn) **1**, 19 (1992).

[30] D. Studer, P. Dyrauf, P. Naubereit, R. Heinke, and K. Wendt, Resonance ionization spectroscopy in dysprosium, Hyperfine Interact. **238**, 8 (2016).

[31] D. Studer, S. Heinitz, R. Heinke, P. Naubereit, R. Dressler, C. Guerrero, U. Köster, D. Schumann, and K. Wendt, Atomic transitions and the first ionization potential of promethium determined by laser spectroscopy, Phys. Rev. A **99**, 062513 (2019).

[32] D. Studer, Resonanzionisationsspektroskopie hochliegender Zustnde in Dysprosium und Erbium zur Entwicklung effizienter Anregungsschemata und Bestimmung des ersten Ionisationspotentials, Master's thesis, Johannes Gutenberg Universität Mainz, 2015 (private communication).

[33] K.-J. Boller, A. Imamoğlu, and S. E. Harris, Observation of Electromagnetically Induced Transparency, Phys. Rev. Lett. **66**, 2593 (1991).

[34] A. K. Mohapatra, T. R. Jackson, and C. S. Adams, Coherent Optical Detection of Highly Excited Rydberg States Using Electromagnetically Induced Transparency, Phys. Rev. Lett. **98**, 113003 (2007).

[35] S. Mauger, J. Millen, and M. P. A. Jones, Spectroscopy of

strontium rydberg states using electromagnetically induced transparency, J. Phys. B: At., Mol. Opt. Phys. **40**, F319 (2007).

[36] J. B. Naber, A. Tauschinsky, H. B. van Linden van den Heuvell, and R. J. C. Spreeuw, Electromagnetically induced transparency with Rydberg atoms across the Breit-Rabi regime, SciPost Phys. **2**, 015 (2017).

[37] K. T. Lu and U. Fano, Graphic analysis of perturbed Rydberg series, Phys. Rev. A **2**, 81 (1970).

[38] C. L. Vaillant, M. P. A. Jones, and R. M. Potvliege, Multichannel quantum defect theory of strontium bound Rydberg states, J. Phys. B: At., Mol. Opt. Phys. **47**, 155001 (2014).

[39] P. Ilzhöfer, G. Durastante, A. Patscheider, A. Trautmann, M. J. Mark, and F. Ferlaino, Two-species five-beam magneto-optical trap for erbium and dysprosium, Phys. Rev. A **97**, 023633 (2018).

[40] S. H. Autler and C. H. Townes, Stark effect in rapidly varying fields, Phys. Rev. **100**, 703 (1955).

[41] E. F. Worden, R. W. Solarz, J. A. Paisner, and J. G. Conway, First ionization potentials of lanthanides by laser spectroscopy, J. Opt. Soc. Am. **68**, 52 (1978).

[42] W. C. Martin, R. Zalubas, and L. Hagan, Atomic energy levels—the rare-earth elements, Nat. Stand. Ref. Data Ser. NSRDS-NBS 60 (1978).

[43] J.-F. Wyart and J. E. Lawler, Theoretical interpretation and new energy levels in Er II, Phys. Scr. **79**, 045301 (2009).

[44] For $n_{eff} = 23$ we observe two $J = 8$ features very close together, which is not yet understood.

[45] A. Frisch, K. Aikawa, M. Mark, F. Ferlaino, E. Berseneva, and S. Kotochigova, Hyperfine structure of laser-cooling transitions in fermionic erbium-167, Phys. Rev. A **88**, 032508 (2013).

[46] M. Aymar, C. H. Greene, and E. Luc-Koenig, Multichannel Rydberg spectroscopy of complex atoms, Rev. Mod. Phys. **68**, 1015 (1996).

[47] J. R. de Laeter, J. K. Böhlke, P. D. Bièvre, H. Hidaka, H. S. Peiser, K. J. R. Rosman, and P. D. P. Taylor, Atomic weights of the elements. Review 2000 (IUPAC Technical Report), Pure Appl. Chem. **75**, 683 (2003).

[48] A. Edmonds, *Angular Momentum in Quantum Mechanics*, 2nd Edition (Princeton University Press, Princeton, NJ, 1974).

[49] A. Kramida, Yu. Ralchenko, J. Reader, and NIST ASD Team, NIST Atomic Spectra Database (Ver. 5.8) (online). https://physics.nist.gov/asd [February 17, 2021] (National Institute of Standards and Technology, Gaithersburg, MD, 2020).

[50] J. R. McNally and K. L. V. Sluis, Preliminary classification of the spectrum of singly ionized erbium (Er II), J. Opt. Soc. Am. **49**, 200 (1959).

[51] J. H. Becher, S. Baier, K. Aikawa, M. Lepers, J.-F. Wyart, O. Dulieu, and F. Ferlaino, Anisotropic polarizability of erbium atoms, Phys. Rev. A **97**, 012509 (2018).

[52] W. Clark and C. H. Greene, Adventures of a Rydberg electron in an anisotropic world, Rev. Mod. Phys. **71**, 821 (1999).

[53] S. Watanabe and C. H. Greene, Atomic polarizability in negative-ion photodetachment, Phys. Rev. A **22**, 158 (1980).

[54] J. Schäfer, Toptica Photonics AG (private communication).